Nonlinear Thermo-mechanical Behavior of Polymers under Multiaxial Loading

Thesis by

Hongbing Lu

In Partial Fulfillment of the Requirements

for the Degree of

Doctor of Philosophy

California Institute of Technology

Pasadena, California

1997

(Submitted April 29, 1997)

To my wife, Hui

The empty space or free volume described by the poet Lucretius who lived in the first century:

"Therefore there is intangible space, voids, emptiness. But if there were none, things could not in any way move; for that which is the province of body, to prevent and to obstruct, would at all times be present to all things; therefore nothing would be able to move forward, since nothing could begin to give place."

Acknowledgements

It is difficult to provide a complete list of the people who helped me during my years at Caltech. First of all, I would like to express my sincere appreciation to Professor W.G. Knauss for his guidance, support and encouragement during the entire course of this study. I am very grateful to Professor Knauss for giving me the opportunity to pursue the research presented in this thesis. Through his scientific intuition, he resolved a lot of my confusions and lead me to the fantasy of this area. I would like to express my appreciation to Professor G. Ravichandran for his advice and encouragement throughout my Ph.D. program. Also I would like to thank Professors K. Bhattacharya, T.K. Caughey, J.A. Kornfield for taking time to review my thesis.

My thanks also go to all my fellow students in the Solid Mechanics Group of the Graduate Aeronautical Laboratories for their comments and suggestions. In particular, I greatly appreciate the help from Drs. W. Chen, T. H. Deng, M. Walter and G. Vendroux for sharing their valuable laboratory experience with me.

This work was initially supported by the program on Advanced Technologies (PAT) at Caltech under the sponsorship of Aerojet General, General Motors and TRW and by ONR grant N00014-91-J-1427 with Dr. Peter Schmidt as the monitor, later work was supported by NASA under grant #NSG 1483, with Dr. Tom Gates as the technical monitor. In addition funds from the National Science Foundation under grant #CMS9504144 allowed completion of this study. The financial support is greatly acknowledged.

Finally I am deeply grateful to my parents for their unwavering belief in education and lovely concern all the time. I am also indebted to my wife, Hui, to whom this thesis is dedicated, for her love, support and appreciation of my research.

Abstract

In order to better understand phenomena related to "yield-like" behavior of polymers, the nonlinear thermo-mechanical behavior of Polymethyl Methacrylate (PMMA) under combined axial (tension, compression) and shear stress states (torsion) is investigated on thin walled cylindrical specimens at temperatures between 22° and 110°C. A non-contact measurement technique based on digital image correlation method is developed to determine the surface deformations on curved cylindrical specimens at various temperatures, including temperatures close to the glass transition when the specimens become soft. The study indicates that in contrast to the mutual independence of shear and dilatational response under conditions appropriate for linearized viscoelasticity, one observes an increasingly strong coupling between all deformation or stress invariants as assessed in creep experiments for strains in excess of 0.4%. While shear stresses alone elicit nonlinear response in creep (rates) as "intrinsically" nonlinear shear response, the superposition of small positive dilatation accelerates shear deformations while negative dilatation retards it in quantitative agreement with free volume arguments. Passing below the glass transition still produces greater creep acceleration from positive dilatation than from a decrease in specific volume, but the dominance of the intrinsic shear nonlinearity vis-a-vis the dilatational influence increases below T_g as the temperature drops. A constitutive model based on free volume consideration is modified from the models proposed by Losi and Knauss (1992). Comparison of experimental results with model prediction indicates a good qualitative agreement and reasonably good quantitative agreement.

Contents

List of Figures

List of Tables

Introductory Remark

In spite of the tremendous increase in polymer applications to various sectors of industry such as automotive, civil, aerospace and electronics, there exists a surprising lack of knowledge regarding polymer nonlinear behavior at elevated load or deformation levels. To date, uniaxial stress or simple shear fields serve almost exclusively to characterize the mechanical properties of these materials. As structural polymers are usually used under multiaxial stress states, the understanding of the multiaxial behavior is essential in the critical application of polymers. As a consequence, the response of polymers under multi-axial loading conditions at different temperatures is investigated in this study.

There are different ways to generate bi-axial stress state. To separate the effects of the infinitesimal volumetric deformation and shear deformation a thin walled cylindrical specimen is used in the experimental investigation because a relatively uniform axial and torsional stress field can be generated under simultaneous axial and torsional loadings.

The difficulties in characterizing the nonlinear behavior of polymers arise from the facts that the polymers become soft around their glass transition temperatures, which makes most standard measurement techniques inappropriate in determining the local surface deformation. Thus a non-contact measurement technique, based on digital image correlation method is developed to determine the local deformation of a cylindrical specimens at various temperatures, including temperatures close to the glass transition when the specimens become very soft.

The nonlinear thermo-mechanical behavior of Polymethyl Methacrylate (PMMA) under combined axial (tension, compression) and shear stress (torsion) states is in-

vestigated between $22°C$ and $110°C$. The interaction between volumetric and shear deformation is investigated so that the effects of volumetric and shear deformations in controlling the general viscoelastic response rate is determined. A constitutive model that includes the contribution to instantaneous local free volume due to shear is proposed to explain the results observed in the experiment.

Chapter 1 Surface Deformation Measurements of a Cylindrical Specimen by Digital Image Correlation

1.1 Abstract

Planar digital image correlation has been extended to measure surface deformations of cylindrical specimens without physical contact for high temperature situations. A single CCD camera acquires the surface image patterns of a section of a specimen in the undeformed and deformed states to determine two dimensional displacements on a projection plane. Axial, circumferential and shear deformations are determined through curvature transformation on the two dimensional projection displacement field. The resolution of this technique was determined for a cylinder of 22.23 mm diameter and was found to be 3.5 μm for the axial displacement, 0.05% for the axial and shear strains and 0.08% for the circumferential strain.

1.2 Introduction

Solid or thin-walled cylindrical specimens subjected to combined axial and torsional loading are often employed to determine multiaxial mechanical behavior. Strain gauges are typically used for measuring surface deformation (axial, circumferential and shear strains) when the stiffness of the test material is comparable to or greater than that of strain gauges and the gauge temperature is not exceeded. However, if the test material is soft, as is the case with polymers near their glass transition temperature, strain gauges are inappropriate since their relatively high stiffness prevents the deformation of the gauge with the specimen material. In this case a non-contact measurement technique must be used. Although the application considered here bears

polymers in mind this method should be equally useful in studying time dependent deformations in metals and ceramics exposed to much higher temperatures.

Some of the currently popular non-contact measurement techniques are successful for measurements of planar deformation, but are not applicable without modification to curved surfaces. For geometric moire and moire interferometry the limitation comes from both the complication of manufacturing gratings on curved surfaces and from the fact that the interference fringes depend on both the surface deformation of the specimen as well as the distance between the flat reference grating and the curved specimen grating. The interferometric strain/displacement gauge (Sharpe, 1982) requires the incident laser beam to be normal to the local surface with sets of indentations and that the interference fringe shift be measured at a fiducial point. These conditions cannot be maintained for a cylindrical specimen undergoing rotation. Since speckle interferometry records two exposures of the surface laser speckle pattern on a holographic plate before and after deformation to deduce the planar deformation, it is difficult to modify this method to measure time dependent, three dimensional deformations.

Because of inherent difficulties in measuring local strain fields on curved surfaces of soft materials, the assumption is often made that the deformation is uniform along the axis of a cylindrical specimen and therefore the local deformation is computed from the relative end rotations and axial displacement. This approach eliminates the possibility to observe potential deformation inhomogeneities which may be prevalent when yield-like behavior is being examined: then a surface deformation computed from the end displacements may not represent the actual local deformation. To track the uniformity of the deformation field on a soft cylindrical specimen with good accuracy requires a new non-contact measurement technique.

Sutton *et al.* (Sutton, *et al.*, 1983; Rason, *et al.*, 1985; Sutton, *et al.*, 1986; Sutton, *et al.*, 1988; Bruck, *et al.*, 1989 and Luo, *et al.*, 1993) proposed a technique to measure

deformations via comparison of digital video images of black- or laser- speckled surfaces in the undeformed and deformed states. A typical resolution of 0.05% of strain could be achieved. Recently this method has been extended to measure sub-micron deformations of in-plane (James, *et al.*, 1990) as well as out-of-plane (Vendroux and Knauss, 1994a and 1994b) displacement field through a digital scanning tunneling microscope and the three-dimensional displacement field through stereo-imaging of a pair of CCD cameras (Luo, *et al.*, 1993).

The technique of measuring the surface deformation of a cylindrical specimen through a single CCD camera imaging is presented here. Digital images of a section of the cylinder specimen in the undeformed and deformed states are acquired and the projection of the displacement field on an observed plane is obtained by using the correlation algorithm proposed by Vendroux and Knauss (1994b). A zero order approximation gray level distribution function is introduced for correlating an experimental image in order to establish the global positioning of the cylinder and account is taken of the curvature to determine the axial, circumferential and shear deformations.

1.3 Experimental

Specimen Preparation: A cylindrical specimen is shown with reference coordinates in figure (1.1). To employ the digital image correlation method a speckle pattern has to be imposed on the specimen surface. This is accomplished by first uniformly spraying (Krylon) flat white spray paint on the specimen surface to generate a white background. After this thin layer of white paint has dried, the black (flat Krylon) paint is sprayed to a Colgate toothbrush and splattered onto the specimen surface to produce black speckles. A high density random black speckle pattern is formed on the specimen with a layer thickness of less than 0.01 mm so that the added load carrying ability of the paint may be neglected in subsequent considerations.

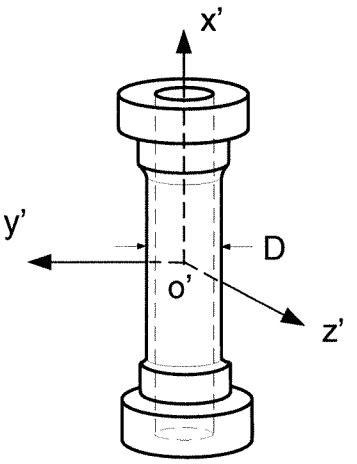

Figure 1.1: Thin walled cylindrical specimen

Recording Equipment: The image acquisition system consisting of a Nikon 200 mm $f/2$ lens with 50 mm exit pupil, a Sanyo CCD camera possessing a spatial resolution of 640×480 $pixels$ and an $8-bit$ gray scale, a Data Translation DT-2855 monochrome frame grabber and a $486-66$ MHz personal computer is used to acquire images automatically during experiment at predetermined times. The CCD camera with the Nikon lens are mounted on a tri-pod and oriented at 90° with respect to the cylinder axis. A black background is placed 30 cm behind the specimen to generate a clear contrast with the specimen diameter. Two Sunnex Halogen illuminators (12V, 20W) illuminate the specimen. By properly adjusting the positions and angles of the two light sources, a relatively uniform light intensities can be generated on the specimen.

1.4 Computation of the Surface Deformation Information from the Acquired Digital Images

Figure 1.2 shows a sample (projection) image of a cylindrical specimen ($D = 22.23$ mm) against the dark observation background. We define in figure 1.3 a fixed frame $\underset{\sim}{F} = \{o, x, y\}$ and a moving frame $\underset{\sim}{F'} = \{o', x', y'\}$, the x' coordinate being coincident with the axis of the specimen, along with the diameter D, orientation angle ξ

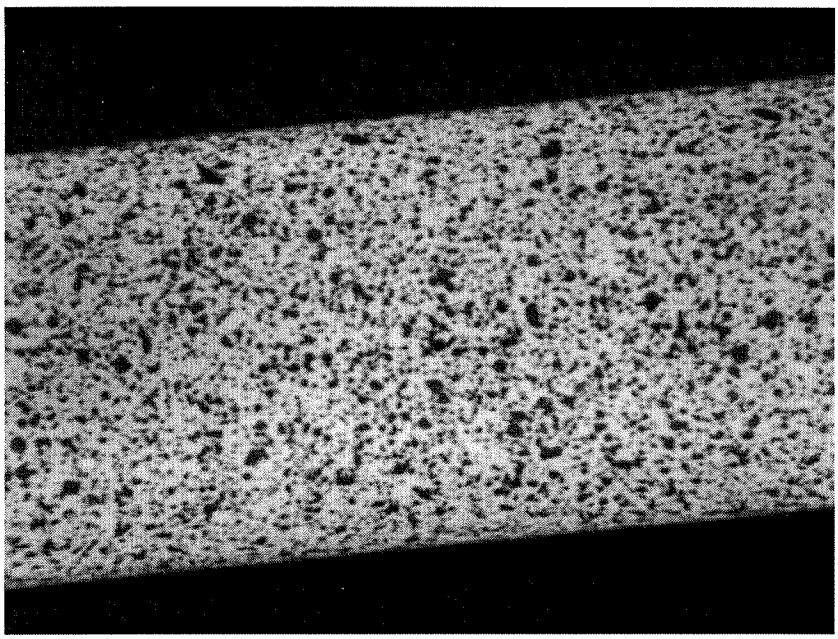

Figure 1.2: A section of a cylindrical specimen

and the position y_0 of the specimen with respect to the image center.

We emphasize that the "local" deformation field anywhere in the image field can be derived from a collection of grid points in a rectangular array ($A_1A_2A_3A_4$ in figure 1.3) that encompasses m grid points in the x direction and n in the y direction.

The two dimensional (projected) displacement field of the surface deformation on an observation plane can then be obtained by the digital image correlation technique (Sutton, *et al.*, 1983; Vendroux and Knauss, 1994b). The comparison of images before and after deformation is accomplished by way of the least square coefficient (Vendroux and Knauss, 1994b) instead of the least cross coefficient (Sutton, *et al.*, 1983). The convergence of the algorithm code is robust. Usually a guess in displacement components which are as far as 7 pixels away from the actual solution in either the x or the y direction still leads to a convergent solution.

The computation field is a grid of m points in the x direction and n points in the y direction. In the examples illustrated in the subsequent sections a grid of 11×11 points with an interval of 10 pixels between neighboring points in either x or y direction is

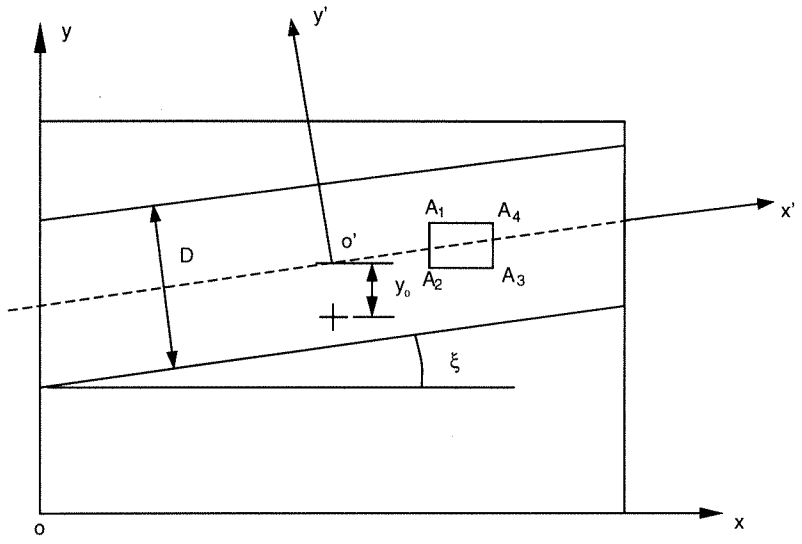

Figure 1.3: Definition of parameters D, ξ and y_0, + represents the point $(x_c,\ y_c)$ which is the center of the image

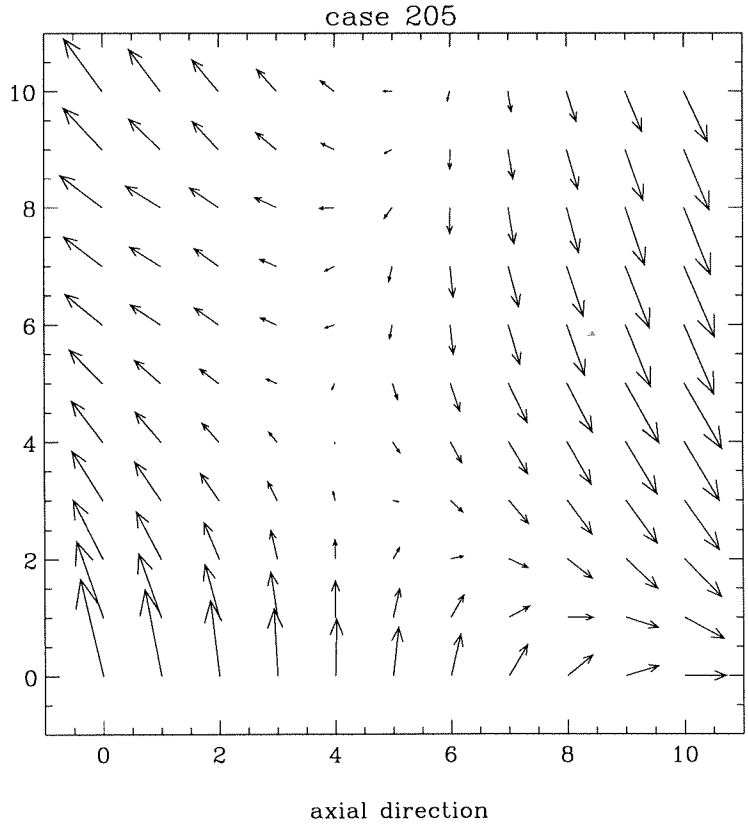

Figure 1.4: Two-dimensional projection displacement field

used. The interpolation subset over the non-grid points are 41×41 *pixels*. This area of investigation may be chosen from anywhere within the viewing field of the CCD camera. The intervals between two neighboring points in either the x or the y direction may be varied. An example of a projection or planar relative displacement field, having its average displacement vector subtracted, is shown in figure 1.4. It represents the displacement field over an area that is 5.52×5.52 mm for a combined tension and torsion resulting in an axial strain of 0.25%, a circumferential strain of -0.2% and a shear strain of 0.19%. The maximum relative displacements are 0.31 *pixels* in the horizontal direction and 0.63 *pixels* in the vertical direction.

1.4.1 The Two-Dimensional Projection Displacement Field of the Surface Deformation and Global Positioning of a Cylindrical Specimen

The results of the planar image correlation are the displacements $[u(x, y)$ and $v(x, y)]$ and the Lagrangian strain components with respect to the (reference) axes of the data acquisition system. However, the determination of the cylinder deformations are needed with respect to the coordinates x' and y'. Since the orientation of the cylinder with respect to $x-y$ coordinates of the recording system is not necessarily accurately pre-determined (cf., figure 1.2), the global positioning and dimensions of the cylinder (diameter for reference purposes) need to be addressed first. The cylinder orientation and its diameter can be determined by comparing a recorded image to a theoretical image which carries the global positioning information. This goal is achieved with the code for the planar configuration and without reference to the circular nature of the specimen. The positioning information can then be extracted by using the Newton-Raphson method to solve a problem of minimizing a least square coefficient.

It is seen in figure 1.2 that the gray levels on the background are (generally) lower (darker) than the gray levels on the specimen. Along the lateral generators or "edges"

of the specimen there exist two abrupt changes in gray levels. Therefore the determination of the radial boundaries of the specimen is equivalent to the determination of the locations of gray level steps in the image reference frame.

In computing the global specimen position, the *variation of gray levels* on the background and on the specimen is not important for purposes of determining the cylinder orientation. As a consequence a "zero order" gray level distribution function is used assuming that the (average) gray levels on the specimen and on the background are represented by two different constants. The transition of gray level from the background to the specimen is then a step function, which is a function with a discontinuous derivative at the boundary of the specimen. However, use of the Newton-Raphson method to determine the global positioning parameters requires the nonlinear function to be differentiable. We, therefore, use a hyperbolic tangent function as a good approximation of a step function and emply the following representation for the average gray level field

$$h(x, y, D, \xi, y_0) = g_b - \frac{(g_f - g_b)}{2}\{\tanh[l(X - \frac{D}{2})] - \tanh[l(X + \frac{D}{2})]\}, \qquad (1.1)$$

where g_b is the average gray level on the background, g_f is the average gray level on the specimen. "l" is an adjustable parameter that determines the slope of the transition zone between the background and the specimen. As l increases the transition of the gray level from the background to the foreground becomes steeper. X is defined as

$$X = -(x - x_c)\sin\xi + (y - y_c - y_0)\cos\xi, \qquad (1.2)$$

with (x_c, y_c) being the center of an image and D, ξ, y_0 are defined in figure 1.3.

The parameters D, ξ and y_0 are determined through the process of correlating this (approximate) gray level distribution function with an experimental image.

Define the least square correlation coefficient C

$$C = \frac{1}{\sum_x \sum_y h_{exp}(x,y)^2} \sum_x \sum_y [h_{exp}(x,y) - h(x,y,D,\xi,y_0)]^2, \tag{1.3}$$

where $h_{exp}(x,y)$ is the gray level of an experimental image. The minimization of C yields the diameter D, orientation ξ and position y_0 of a specimen in an image. The Newton-Raphson method with the use of the approximate Hessian matrix (Vendroux and Knauss, 1994b) is used to solve this minimization problem.

Let D, y_0, ξ_0 define a three dimensional vector space $\mathcal{S}$

$$\mathcal{S} = \{\underset{\sim}{Q} \in \mathcal{R}^3 | \underset{\sim}{Q}(D, y_0, \xi)\} \tag{1.4}$$

$\underset{\sim}{Q}$ is an unknown vector in C, $C = C(\underset{\sim}{Q})$. Let $\underset{\sim}{Q}_0$ be the vector solution of the minimization problem. Expanding $C(\underset{\sim}{Q})$ as a truncated Taylor series around $\underset{\sim}{Q}_0$ gives

$$C(\underset{\sim}{Q}) = C(\underset{\sim}{Q}_0) + \nabla C(\underset{\sim}{Q}_0)^T(\underset{\sim}{Q} - \underset{\sim}{Q}_0) + \frac{1}{2}(\underset{\sim}{Q} - \underset{\sim}{Q}_0)^T \nabla\nabla C(\underset{\sim}{Q}_0(\underset{\sim}{Q} - \underset{\sim}{Q}_0) \tag{1.5}$$

Since $\underset{\sim}{Q}_0$ corresponds to a minimum C, $\nabla C(\underset{\sim}{Q}_0) = 0$. Consequently, taking the gradient of the above equation yields

$$\nabla\nabla C(\underset{\sim}{Q}_0)(\underset{\sim}{Q} - \underset{\sim}{Q}_0) = -\nabla C(\underset{\sim}{Q}_0) \tag{1.6}$$

Solving $\underset{\sim}{Q}_0$ iteratively from the above equation will converge to the vector solution $\underset{\sim}{Q}_0$ of the minimization problem. This algorithm, called the Newton-Raphson optimization method (Bruck *et al.*, 1989, Vendroux and Knauss, 1994b) requires the representation of $\nabla\nabla C(\underset{\sim}{Q})$, the components of which are defined as

$$[\nabla\nabla(C)]_{ij} = \left(\frac{\partial^2 C}{\partial Q_i \partial Q_j}\right)_{i=1,3;j=1,3}. \tag{1.7}$$

However, it may not be necessary to compute the second derivatives of C with respect to $\underset{\sim}{Q}$, i.e.,

$$[\nabla C]_{ij} = \left(\frac{\partial C}{\partial Q_i}\right)_{i=1,3}. \tag{1.8}$$

To show this, we first write down the components of ∇C:

$$\frac{\partial C}{\partial Q_i} = \frac{-2}{\sum_x \sum_y h_{exp}(x,y)^2} \sum_x \sum_y [h_{exp}(x,y) - h(x,y,D,y_0,\xi)] \frac{\partial h(x,y,D,y_0,\xi)}{\partial Q_i}, \tag{1.9}$$

taking another derivative gives the components of Hessian matrix

$$\begin{aligned} \frac{\partial^2 C}{\partial Q_i \partial Q_j} &= \frac{-2}{\sum_x \sum_y h_{exp}(x,y)^2} \sum_x \sum_y [h_{exp}(x,y) - h(x,y,D,y_0,\xi)] \frac{\partial^2 h(x,y,D,y_0,\xi)}{\partial Q_i \partial Q_j} \\ &+ \frac{2}{\sum_x \sum_y h_{exp}(x,y)^2} \sum_x \sum_y \frac{\partial h}{\partial Q_i} \frac{\partial h}{\partial Q_j} \end{aligned} \tag{1.10}$$

If $\underset{\sim}{Q}$ is close to the $\underset{\sim}{Q_0}$, the experimental gray level $h_{exp}(x,y)$ will approach the ideal gray level $h(x,y,D,y_0,\xi)$, and the first term in equation (1.10) will be small compared to the second term. Neglecting the first term, the Hessian matrix can be approximated as

$$\frac{\partial^2 C}{\partial Q_i \partial Q_j} = \frac{2}{\sum_x \sum_y h_{exp}(x,y)^2} \frac{\partial h}{\partial Q_i} \frac{\partial h}{\partial Q_j}. \tag{1.11}$$

$\frac{\partial h}{\partial Q_i}$ are given by

$$\frac{\partial h}{\partial D} = \frac{(g_f - g_b)}{4} l\{sech^2[l(X - \frac{D}{2})] + sech^2[l(X + \frac{D}{2})]\},$$

$$\frac{\partial h}{\partial y_0} = -[\frac{(g_f - g_b)}{2} l\{\cos\xi[sech^2[l(X - \frac{D}{2})] - sech^2[l(X + \frac{D}{2})]]\},$$

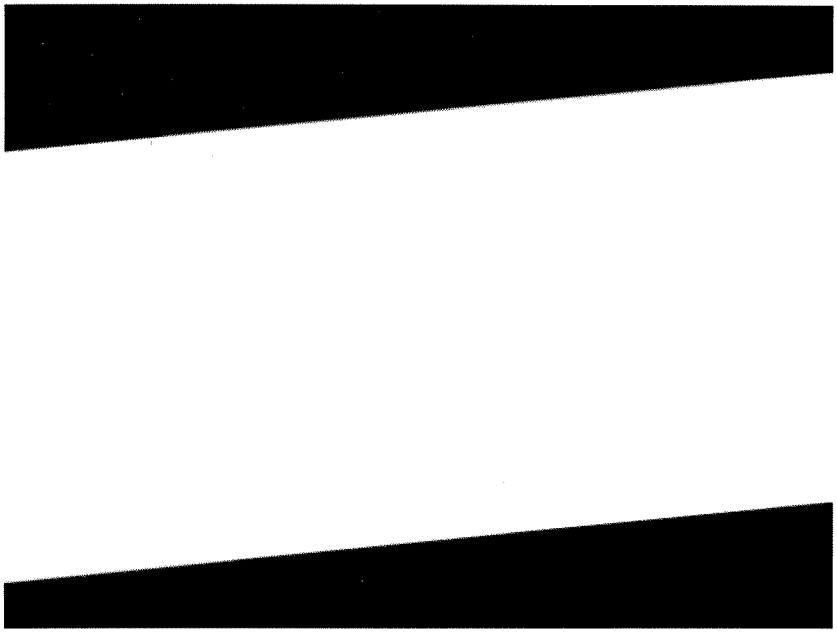

Figure 1.5: An ideal image used to determine the global positioning parameters

$$\frac{\partial h}{\partial \xi} = -\frac{(g_f - g_b)}{2} l\{[(x-x_c)\cos\xi-(y-y_c-y_0)\sin\xi)][sech^2[l(X-\frac{D}{2})]-sech^2[l(X+\frac{D}{2})]]\}.$$

From this algorithm, the global positioning information can be obtained for the reference image and deformed image.

As an example, the global positioning parameters for the image shown in figure 1.2 were determined in this way to be: $D = 331.0 \pm 0.05$ *pixels*, $\xi = 5.5 \pm 0.05°$ and $y_0 = -12.2 \pm 0.05$ *pixels*. The ideal gray level distribution function with these parameters is plotted in figure 1.5.

1.4.2 Accommodation for Curvature and the Determination of the Axial, Circumferential and Shear Strains

The two dimensional displacement components on the projection plane as well as the global positioning parameters are used to deduce the axial, circumferential and shear

deformations of the specimen. Assume that the surface deformation field is *locally* uniform in the computation field on the surface of the cylinder. The displacement components $u(x,y)$ and $v(x,y)$ obtained in section 1.4.1 are along the x and y directions of a planar (projection) image, not necessarily along the x' and y' directions attached to the cylindrical specimen (cf., figure 1.3). Using the global positioning parameters D, ξ and y_0, the displacement components $u'(x,y)$ and $v'(x,y)$ along the x' and y' directions on the projection plane are obtained with the help of the "moving frame" $\underset{\sim}{F}' \in \{o', x', y'\}$. In frame $\underset{\sim}{F}'$, the coordinates of a point (x,y) in the undeformed state in the fixed image frame $\underset{\sim}{F} \in \{o, x, y\}$ are

$$x'_u = (x - x_c)\cos\xi_u - (y - y_c - y_{0u})\sin\xi_u, \tag{1.12}$$

$$y'_u = (x - x_c)\sin\xi_u + (y - y_c - y_{0u})\cos\xi_u, \tag{1.13}$$

where D_u, ξ_u and y_0 are the positioning parameters for the undeformed image. In the deformed state, the point (x,y) moves to $(x+u(x,y), y+v(x,y))$, and the coordinates of this point in the frame $\underset{\sim}{F}'$ are

$$x'_d = (x + u - x_c)\cos\xi_d - (y + v - y_c - y_{0d})\sin\xi_d, \tag{1.14}$$

$$y'_d = (x + u - x_c)\sin\xi_d + (y + v - y_c - y_{0d})\cos\xi_d, \tag{1.15}$$

where D_d, ξ_d and y_{0d} are the positioning parameters in a deformed image. The (projected) displacements of the point (x,y) are then

$$u'(x,y) = x'_d(x,y) - x'_u(x,y), \tag{1.16}$$

$$v'(x,y) = y'_d(x,y) - y'_u(x,y), \tag{1.17}$$

where $u'(x,y)$, $v'(x,y)$ are displacement components along the x' and y' directions respectively. The rigid body translation in either the x' or y' direction and the rigid

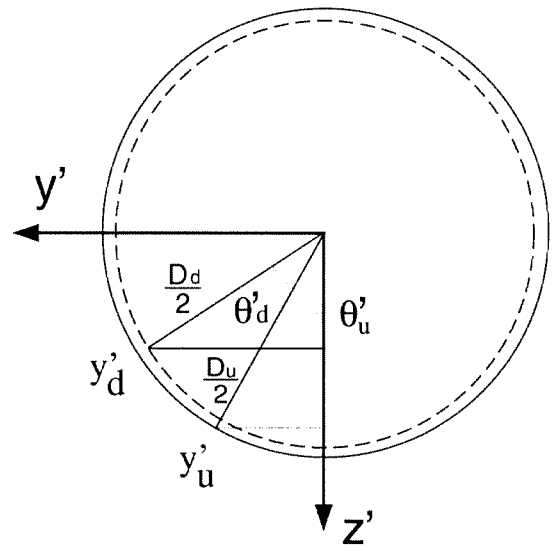

Figure 1.6: Definition of θ'_u and θ'_d

body rotation around the z' axis have been accounted for in u' and v'.

Let θ'_u be the circumferential angle of point $(x'_u,\ y'_u)$ in the undeformed state as defined in figure 1.6.

$$\theta'_u = \sin^{-1}[\frac{2y'_u}{D_u}]. \tag{1.18}$$

Similarly, the circumferential angle of $(x'_d,\ y'_d)$ in the deformed state is

$$\theta'_d = \sin^{-1}[\frac{2y'_d}{D_d}]. \tag{1.19}$$

The relation between angles θ'_u and θ'_d is

$$\theta'_d = \theta'_u(x', y') + \theta'_0(\bar{x}'_u, \bar{y}'_u) + \alpha(x'_u - \bar{x}'_u), \tag{1.20}$$

where $(\bar{x}'_u, \bar{y}'_u)$ is a reference point in the computation field; it can be any grid point at which the displacements are computed. The (circumferential) rotation angle of this point during deformation is θ'_0. α is the rotation angle per unit length of the cylinder.

The two dimensional projections of the displacement field onto the image plane are then

$$u_1(x,y) \equiv \hat{u}'(x',y') = u'(\bar{x}'_u, \bar{y}'_u) + \epsilon_{x'x'}(x'_u - \bar{x}'_u), \tag{1.21}$$

$$v_1(x,y) \equiv \hat{v}'(x',y') = \frac{1}{2}D_d \sin\theta'_d - \frac{1}{2}D_u \sin\theta'_u, \tag{1.22}$$

where $u'(\bar{x}', \bar{y}')$ is the axial displacement of point $(\bar{x}, \bar{y})$, and $\epsilon_{x'x'}$ is the local axial strain. $\epsilon_{x'x'}$ and α need to be determined.

Define the least square correlation coefficient

$$C' = \frac{\sum_x \sum_y [u'(x,y) - u_1(x,y)]^2}{\sum_x \sum_y [u'(x,y)]^2}. \tag{1.23}$$

By definition, $u'(\bar{x}, \bar{y}) = u'(\bar{x}'_d,\ \bar{y}'_d) - u'(\bar{x}'_u,\ \bar{y}'_u)$, if this relation is used in equation (1.21) and then $\epsilon_{x'x'}$ is computed by minimizing C', there will be an accumulated error in $\epsilon_{x'x'}$ due to the error in axial displacement from a single point $(\bar{x}, \bar{y})$. To reduce this possibly accumulated error in $\epsilon_{x'x'}$, we seek here a $u'(\bar{x}, \bar{y})$ that can allow the experimental displacements u_1 (equation 1.21) to best fit u' (equation 1.16) in the whole computation field so as to find the best fit for $u'(\bar{x}, \bar{y})$ and $\epsilon_{x'x'}$.

Minimizing C' yields $u'(\bar{x}, \bar{y})$ and $\epsilon_{x'x'}$

$$u'(\bar{x}, \bar{y}) = \frac{[\sum_x \sum_y u'][\sum_x \sum_y (x'_u - \bar{x}'_u)^2] - [\sum_x \sum_y u'(x'_u - \bar{x}'_u)][\sum_x \sum_y (x'_u - \bar{x}'_u)]}{(m \times n)[\sum_x \sum_y (x'_u - \bar{x}'_u)^2] - [\sum_x \sum_y (x'_u - \bar{x}'_u)]^2}, \tag{1.24}$$

$$\epsilon_{x'x'} = \frac{(m \times n)[\sum_x \sum_y u'(x'_u - \bar{x}'_u)] - [\sum_x \sum_y u'] \sum_x \sum_y [(x'_u - \bar{x}'_u)]}{(m \times n)[\sum_x \sum_y (x'_u - \bar{x}'_u)^2] - [\sum_x \sum_y (x'_u - \bar{x}'_u)]^2}. \tag{1.25}$$

Following the same procedure as in the computation of $\epsilon_{x'x'}$, we have

$$\theta'_0 = \frac{[\sum_x \sum_y \beta][\sum_x \sum_y (x'_u - \bar{x}'_u)^2] - [\sum_x \sum_y \beta(x'_u - \bar{x}'_u)][\sum_x \sum_y (x'_u - \bar{x}'_u)]}{(m \times n)[\sum_x \sum_y (x'_u - \bar{x}'_u)^2] - [\sum_x \sum_y (x'_u - \bar{x}'_u)]^2}, \tag{1.26}$$

$$\alpha = \frac{(m \times n)[\sum_x \sum_y \beta(x'_u - \bar{x}'_u)] - [\sum_x \sum_y \beta] \sum_x \sum_y [(x'_u - \bar{x}'_u)]}{(m \times n)[\sum_x \sum_y (x'_u - \bar{x}'_u)^2] - [\sum_x \sum_y (x'_u - \bar{x}'_u)]^2}, \tag{1.27}$$

where

$$\beta = \sin^{-1} \frac{v' + \frac{1}{2} D_u \sin \theta'_u}{\frac{1}{2} D_d} - \theta'_u. \tag{1.28}$$

For "infinitesimal deformation", the shear strain is

$$\epsilon_{x'\theta'} = \frac{1}{4} D_u \alpha. \tag{1.29}$$

As long as the specimen is and remains perfectly circular and the deformation is uniform in the imaged section of the specimen, the circumferential strain can be computed from the circumference of the specimen as

$$\epsilon_{\theta'\theta'} = \frac{D_d - D_u}{D_u}. \tag{1.30}$$

If the deformations are inhomogeneous, the circumferential strain needs to be computed from the local deformation by image correlation. In the present study involving mostly twist and axial extension it turned out, however, that this local deformation always gave less accurate values than equation (1.30).

1.5 Validation of the Algorithm

Experiments were designed to check the validity of using the approximate gray level distribution function as defined in equation (1.1) to determine the global positioning information and, second, the validity of using the curvature correction algorithm for determining the local cylindrical deformations.

1.5.1 Global Positioning of Ideal Images

For this examination two ideal example images were constructed. The first ideal image exhibits a gray level of 0 on the background and of 255 on the specimen. The diameter of the specimen D is set to 200 $pixels$, the position y_0 is 0 $pixel$ and the orientation angle is 0°. Using this gray level distribution computations lead to the following global, code determined, positioning parameters: $D = 200.0001$ $pixels$, $y_0 = 2.278 \times 10^{-5}$ $pixels$ and $\xi = 2.212 \times 10^{-12°}$. The computations thus indicate excellent agreement between the prescribed parameters and the computation results for the ideal image. In this example, the adjustable parameter l in equation (1.1) is set to unity. It is found that the computational speed for $l = 1$ is 4 times faster than for $l = 1000$ for the same accuracy, i.e., a steeper transition in gray level from the background to the specimen results in a slower convergence. In all the subsequent examples, $l = 1$ was used.

For the second image $D = 98.2878$ $pixels$, $y_0 = 0.5$ $pixels$ and $\xi = 45°$ were chosen. To construct this ideal image with a specimen oriented at 45° of angle ξ, "stairs" of gray level distributions on the two sides of the specimen were used. The diameter of this ideal image is the distance between the two lines passing through the centers of the "stairs". The computations yielded $D = 98.2885$ $pixels$, $y_0 = 0.4996$ $pixels$ and $\xi = 44.9993°$. The algorithm can thus recover the parameters with very high accuracy. This demonstrates that the proposed gray level distribution

function defined in equation (1.1) can be used to determine the global positioning parameters for ideal images.

1.5.2 In-Plane Rotation

Next the validity of this algorithm for the determination of the global positioning parameter, ξ, is examined. When a specimen undergoes rigid rotations around the z' axis (figure 1.1), the rotation angles should be recoverable. A cylinder of diameter 22.23 mm coated with a random speckle pattern was mounted on a Melles Griot manual rotation stage (Model 470-B) with a resolution capability of 0.084° with the cylinder axis perpendicular to the rotation axis of the stage. Table 1.1 shows the prescribed and commutated rotation angles. The maximum error is 3.51%, indicating that the proposed function in equation (1.1) of a zero order gray level distribution provides a good approximation in the determination of the orientation angle of a cylinder relative to an image reference frame.

Table 1.1: In plane rotation angles

Prescribed Rotation (°)	Computed Rotation (°)	Error (°)	Percent Error (%)
1.00	0.9688	0.0312	3.12
2.00	1.9299	0.0701	3.51
3.00	2.9308	0.0692	2.31
4.00	3.8900	0.1100	2.75
5.00	4.8899	0.1101	2.21
6.00	5.8373	0.1627	2.71

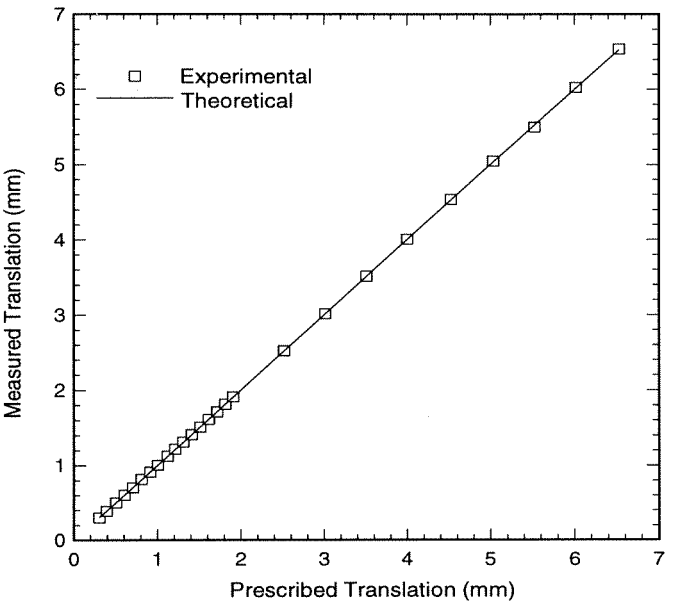

Figure 1.7: Translation in the axial direction of the cylinder

1.5.3 Specimen Translation in the Axial Direction

A cylindrical specimen coated with a random black speckle pattern is mounted on a translation stage driven by a NRC translation actuator (model 360-30) with a resolution of $0.1\mu m$. The axis of the cylinder is parallel to the translation direction of the translation stage. The magnification of this optical setup was determined by a translation of 6.529 mm and by computing the displacement in $pixels$ through digital image correlation. The displacement in $pixels$ is $\sqrt{u^2 + v^2}$ with u and v being the displacement components in the x and y directions (measured along the image coordinates x, y). The magnification for this optical setup is 0.053 $mm/pixel$. Figure 1.7 indicates that the axial displacement can be recovered with very high accuracy. The standard deviation in displacement is 0.0065 $pixel$, which interprets into an accuracy of $3.5\mu m$ in axial translation.

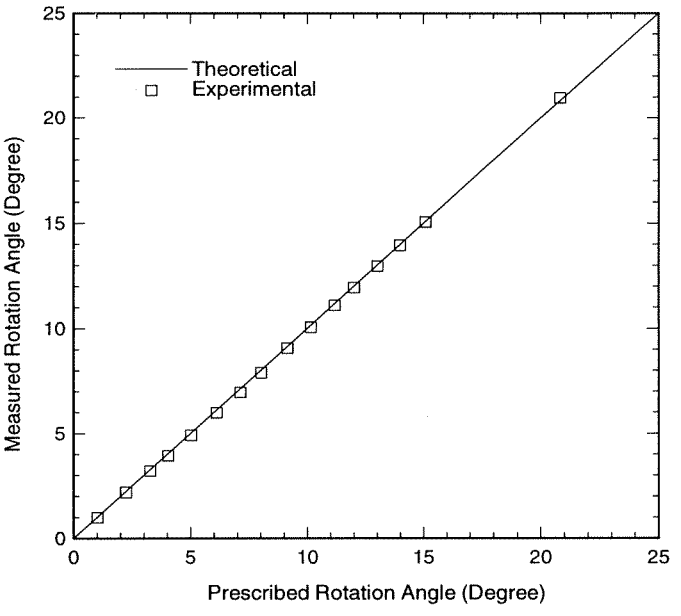

Figure 1.8: Rotation around the axis of the cylinder

1.5.4 Rigid Body Rotation of a Specimen Around its Axis

To explore this mode of motion a cylinder was mounted to the piston of a servo-hydraulic MTS machine possessing a resolution of 0.001 degree in rotation angle. The comparison of the prescribed rotation angles and the results from the computation is shown in figure 1.8. The maximum deviation is 1.3%, indicating that the computed rotation angles match the prescribed angles very well.

1.5.5 Comparison of Strain Gauge Measurements and Image Correlation

To compare the ability of the image correlation method on a cylindrical specimen with standard strain gauge measurements a rosette is attached to an aluminum 2024, thin walled cylindrical specimen of 22.23 *mm* diameter and 1.59 *mm* wall thickness with gauges oriented in the 45°, 90° and 135° directions with respect to the circumferential direction. The random paint speckle pattern is deposited right over the rosette to

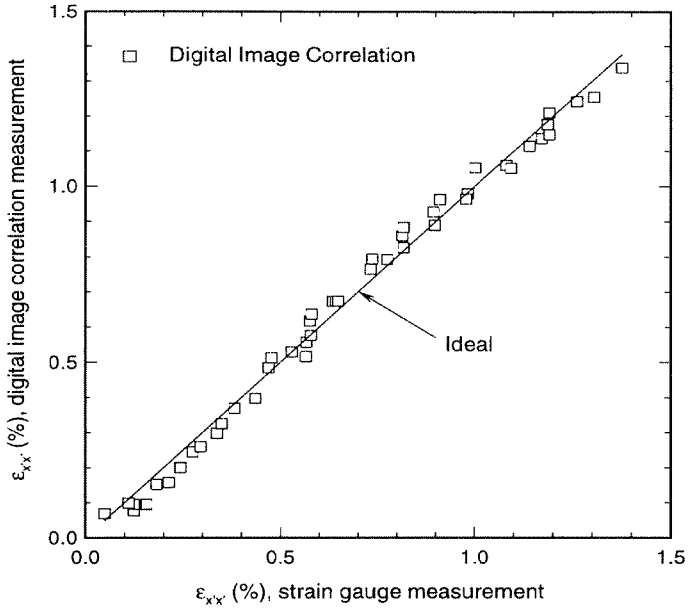

Figure 1.9: Axial strain

assure that the deformation measurements via the strain gauge rosette and digital image correlation are made at the same location. The strain gauge rosette has an area of 5 $mm \times 5$ mm and the computation field for the digital image correlation is carried out over the same area. The specimen is subjected to simultaneous tension and torsion. The loading is applied through a proportional ramp in the axial displacement and the rotation angle. The results from both methods are shown in figures 1.9, 1.10 and 1.11. The maximum deviation between the measurements of the strain gauge and the digital image correlation is $|\Delta\epsilon_{x'x'}| = 0.05\%$, $|\Delta\epsilon_{x'\theta'}| = 0.05\%$. The percent error for the axial strain is high for strain values below 0.5% but improves for larger strains, but at 1.5% of axial strain the percent deviation is still 3.4%. The maximum deviation between the measurements of strain gauge rosette and this technique was used as the accuracy of this measurement method.

In figure 1.11 the circumferential strains are computed from the diameters of the specimen in the undeformed and deformed states as formulated in equation (1.30).

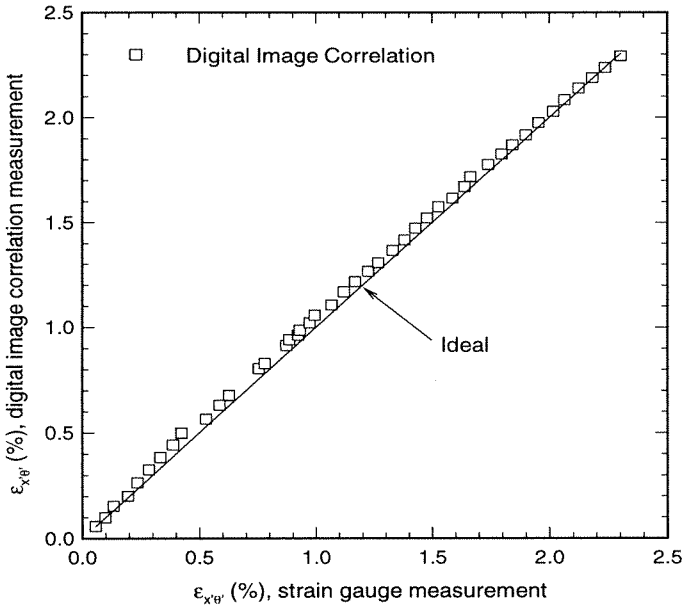

Figure 1.10: Shear strain

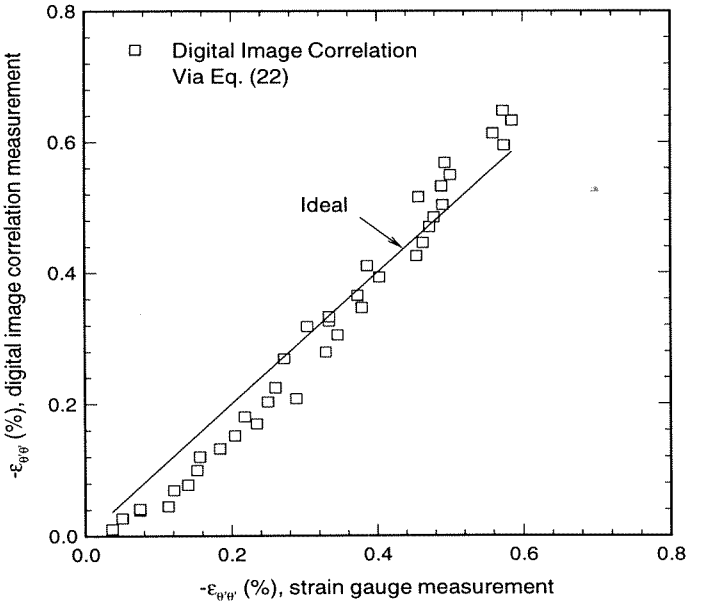

Figure 1.11: Circumferential strain

The circumferential strain computed by digital image correlation fits the prescribed circumferential strains only reasonably well. The maximum deviation is $|\Delta\epsilon_{y'y'}| = 0.08\%$, which is not much higher than for the axial strain case. However since the circumferential strain is usually less than half of the axial strain, in experiments involving $\epsilon_{x'x'}$ strains of only 1% to 2%, this magnitude of error may be too large to allow the satisfactory determination of Poisson's ratio.

1.6 Conclusions

A non-contact technique has been developed to measure surface deformations of cylindrical specimens by digital image correlation technique, which employs an image acquisition system with a single CCD camera system to obtain the digital image of the projection of a specimen coated with a random black speckle pattern. A zero-order gray level distribution function consisting of hyperbolic tangent functions is employed to represent the gray level distribution of an experimental image in order to determine the global positioning information (diameter, orientation and position). The displacement components computed from the two dimensional digital image correlation scheme resolved along the reference axes of an image (camera position dependent) are decomposed into directions along the axial and transverse directions of the cylindrical specimen. The cylinder curvature is accounted for in deriving these decomposed displacement components and the axial, circumferential and shear and strains can be determined. This technique has accuracies of $3.5\mu m$ for axial displacements, 0.05% in axial and shear strains and 0.08% in circumferential strain for a cylinder with a diameter of 22.23 mm. The method should thus be useful for determining strains on the order of a few tenths of a percent or larger.

Chapter 2 Uniaxial, Shear and Poisson Relaxation and their Conversion to Bulk Relaxation

2.1 Abstract

Multiple viscoelastic properties are determined for PMMA in the context of examining experimental limitations on deriving other properties from these measurements, specifically time dependent bulk modulus behavior. By means of master curves for uniaxial extension on plate and cylinder specimens, as well as shear (torsion) and Poisson behavior[1] from measurements in the temperature range from $-40°C$ to $125°C$, it is established that exorbitant precision is needed for reliable interconversion of some properties to others. While normal inverse relations (modulus-compliance) are readily obtained from one set of measurements, bulk (relaxation or creep) properties cannot be derived reliably from other functions and must be determined directly.

2.2 Introduction

Within the context of linearly viscoelastic material behavior it is sufficient for any analysis effort to define any two of the four material functions (in relaxation or creep) describing uniaxial, shear, bulk or Poisson response. In the relaxation mode these properties are identified as the uniaxial modulus $E(t)$, the shear modulus $\mu(t)$, the bulk modulus $K(t)$ and Poisson's ratio $\nu(t)$, with appropriate functions defined for the creep complement. By implication any two can then be computed from the others.

In current engineering practice it is common to deal with either the uniaxial or shear relaxation modulus, assuming that the other function is described sufficiently

[1]The Poisson behavior is determined by Zhang and Knauss (1991).

well in terms of a constant Poisson's ratio or a constant bulk modulus. With the advent of more refined and powerful methods of computation the need arises to know the material behavior with an increasing degree of sophistication. As a consequence it becomes important to be able to determine the material properties with more precision for a full characterization of (even) linearly viscoelastic materials than current engineering practices allow. For example, few reliable records of two of the four time-dependent material functions for the same materials exist. Similarly, there is an unbelievable dearth of information on the time dependent bulk response of linearly viscoelastic materials (in the transition range). These difficulties in understanding viscoelastic materials more fully derive from the often poorly appreciated time dependent characteristics of these materials, their temperature sensitivities, and the fact that both large and small deformations may be involved and need to be addressed separately.

While some experimentally oriented investigators have realized serious limitations in being able to determine any of the material functions from the others (Heydemann, 1959), this recognition is anything but general, and it appears appropriate to demonstrate the experimental limitation underlying this conversion failure. Moreover, even though a purely analytical demonstration using typical, though fictitious properties might suffice, it appears more convincing to many to deal with measured material properties.

We report two groups of material functions for PMMA materials. For the first group of tests, strip specimens are used to measure the uniaxial modulus and Poisson's ratio in relaxation with an image moire method on a Rohm & Haas material. In the second group, tubular specimens are used to measure the uniaxial and the shear relaxation moduli of an ACE material as monitored with the digital image correlation method (Lu, Vendroux and Knauss, 1996). Moreover, preliminary uniaxial tension and Poisson's ratio measurements conducted dynamically at 5 MHz frequencies,

and uniaxial tension experiments at a strain rate of $0.1\%/min$ at a temperature of $22°C$; i.e., $83°C$ below the glass transition, suggested that the uniaxial modulus still decreases rather significantly under both conditions, so that relaxation behavior at lower than room temperature conditions was indicated. Accordingly temperatures as low as $-40°C$ are included in our study.

The earliest comprehensive temperature-dependent data for $E(t)$ on PMMA were reported by McLoughlin and Tobolsky (1952) but similar shear relaxation data does not appear to have been collected over as wide a range of temperatures. Several investigators have contributed to the measurement of $E(t)$ for PMMA, among them, Rusch (1968) provided relaxation data between $-20°$ and $106°C$. The temperature and time dependent Poisson's ratio, $\nu(t)$, has not been measured directly in the transition range, though Poisson's ratio in the "glassy" state has been measured repeatedly as a (limited) function of time: Gilmour, *et al.* (1974) summarized results on E and ν for polystyrene; Wilson, *et al.* (1976a, 1976b) measured $\nu(t)$ on polyethylene sheets using both an optical technique and Michelson interferometry; McCammond, *et al.* (1973) determined $\nu(t)$ from the deflection of a freely-supported circular plate under uniformly distributed pressure for PMMA and PVC materials at room temperature. However, the experimental methods employed in these studies, except possibly the optical ones (Wilson, *et al.* 1976, 1988) lead to serious difficulties when applied over a wide range of temperatures.

2.3 Analytical Prerequisites

The analytical relations connecting the various material functions of linear viscoelasticity are readily derived and need not be recounted here. We document here only the formulae for the numerical computations that are based on the Hopkins and Hamming algorithm (1957) The range of material response is divided into "n" (non-constant) time intervals t_n so that the relaxation bulk modulus can be computed as a function

of time from the uniaxial modulus $E(t)$ and the Poisson function $\nu(t)$ via

$$K(t_n) = \frac{\frac{E(t_n)}{3} + K(t_{n-1})[\nu_g - \nu(t_n - t_{n-1})] + \sum_{i=1}^{n-1}[K(t_{i-1}) + K(t_i)][\nu(t_n - t_i) - \nu(t_n - t_{i-1})]}{1 - 3\nu_g + \nu(t_n - t_{n-1})} \tag{2.1}$$

with

$$K(t_1) = \frac{E(t_1)/3 + K_g[\nu_g - \nu(t_1)]}{1 - 3\nu_g + \nu(t_1)}$$

and $K_g = \dfrac{E_g}{3(1-2\nu_g)}$, $E_g = E(0)$, $\nu_g = \nu(0)$; on the other hand, given $E(t)$ and the shear modulus $\mu(t)$ this quantity is computed from

$$\begin{aligned} K(t_{n-\frac{1}{2}}) &= \frac{1}{3f(t_n - t_{n-1})}\{3\sum_{i=1}^{n-1} K(t_{i-\frac{1}{2}})[f(t_n - t_i) - f(t_n - t_{i-1})] \\ &\quad - \sum_{i=1}^{n} \mu(t_{i-\frac{1}{2}})[g(t_n - t_i) - g(t_n - t_{i-1})]\}, \end{aligned} \tag{2.2}$$

with

$$f(t) \equiv \int_0^t [3\mu(\xi) - E(\xi)]d\xi, \qquad g(t) \equiv \int_0^t E(\xi)d\xi,$$

and

$$K(t_{\frac{1}{2}}) = \frac{\mu(t_{\frac{1}{2}})g(t_1)}{3f(t_1)}.$$

2.4 Experimental Work

As mentioned before, material functions for PMMA were determined for two variants: the first set led to uniaxial relaxation modulus and Poisson's ratio using a flat speci-

men for a Rohm & Haas material. The second set of measurements yielded uniaxial and shear relaxation functions as determined through tension and torsion of a hollow cylinder specimen made of an ACE PMMA.

2.4.1 Measurements of the Uniaxial Modulus and Poisson's Ratio

Image moire was used to monitor the specimen deformation with time under strain, and force recording was accomplished on an MTS servo hydraulic testing system via a Masscomp data acquisition system; the moire fringe data was acquired photographically.

Material and Specimen Preparation

The material for this portion of study (commercial PMMA, Rohm & Haas, nominally 4.8 mm thick and possessing a T_g of $105°C$) was annealed[2] for two Hours in air at $120°C$ and cooled down (slowly) at $5°C/hr$ to room temperature. The specimen is shown in figure 2.1, with moire grid locations and orientations indicated. Its ends were reinforced with aluminum tabs to reduce grip creep in that portion of the specimen. As a result, very stable ϵ_{yy} strains were obtained as determined by continuous monitoring. For each test at the various temperatures new specimens were used to eliminate uncertainties arising from previous strain and thermal histories. All specimens were cut from a single large sheet of PMMA without special orientation preference.

The photoresist method was used to provide moire gratings for monitoring the axial and transverse strains. A master grating with 40 lines per millimeter was found optimal, since a finer grating developed resolution problems due to multiple reflections of the light beam as it passed through the window of the environmental chamber.

[2]This annealing process was necessary because the as-received material contained residual strains. While there exists a mild anisotropy in the material, that material feature disappears within experimental error after annealing.

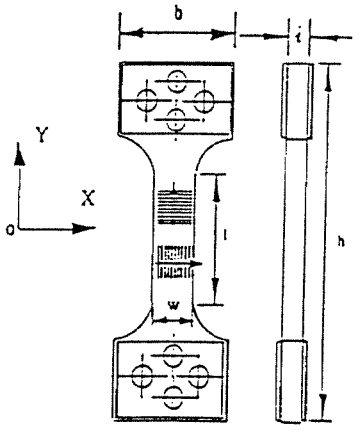

Figure 2.1: Specimen cut from Rohm & Haas plate

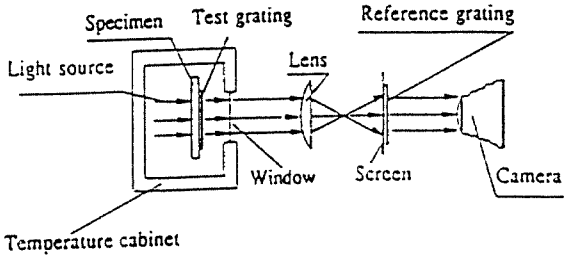

Figure 2.2: Test and recording arrangement

Physical Test Arrangement

A schematic of the test set-up is given in figure 2.2. The lens system is adjusted to provide an initial, small mismatch between the grating on the specimen and its screen image to enhance the sensitivity of the measurements. This lens system is used to measure the ratio of the transverse strain and axial strain via the moire method.

An MTS servo hydraulic system was used to load the specimen to a constant strain and the corresponding axial load was recorded by the Masscomp data acquisition system. In addition to the moire monitoring the strain was tracked by an MTS extensometer with a gage length of 25.4 *mm*. A Russell's environmental unit pro-

vided temperature control between $-40°C$ and $125°C$. Liquid Nitrogen was used to produce temperatures below $0°C$. The temperature was continuously monitored by a thermocouple close to the specimen which was always within $\pm 0.2°C$ of the set temperature. Optically flat window glass in the environmental control housing reduced measurement errors due to light aberrations. Straining by ramp deformation entailed a typical rise time of 1 second. The constant strain was 0.2% at all temperatures except 0.5% at $-40°C$. These small strains were necessary to avoid nonlinear effects. Using rigid wedge grips, the small strain could always be maintained with an accuracy of 1% for the constant strain, ϵ_{y0}. The room humidity remained at about 50% for these tests. The load cell has a full capacity of $15kN$ as calibrated to a precision of $\pm 0.5N$.

Photographs taken of the fringes indicative of the strain in the axial and transverse directions were photographed periodically, and enlarged photographs were passed through a digitizer to obtain an average scan of the gray level distribution. After calibrating this data reduction method with an interferometrically generated fringe pattern of known frequency, the strains were determined (shown in section 2.4.1) to render Poisson behavior with an accuracy of $\pm 10\%$. Dimension and load levels were such as to allow the relaxation modulus to be determined with an accuracy of $\pm 4\%$.

Image Processing and Data Analysis

Fringe images taken at various times (motor driven Nikon F camera with Nikon 85 mm f 45 lens) were scanned with a digitizing scanner possessing a resolution of 118 pixels per cm (The moire pattern covered an area of 4.3×10 cm on the photograph). At least 500 line passes were taken across the fringes and the gray scale distribution was averaged to obtain the mean fringe spacing $f(t)$. Accuracy calibration of this method was accomplished with the help of an interferometrically constructed fringe pattern of 3.96 mm. Processing of this image produced a fringe spacing of 3.98 mm.

This 0.02 mm difference corresponds to a 0.5% error relative to the known spacing. We accept this error bound for all fringe evaluations.

To evaluate the correspondence for the accuracy in measuring Poisson's ratio one needs to evaluate the error incurred in the moire fringe evaluation. To achieve improved sensitivity of the moire process one employs an initial mismatch between image and reference grating such that an initial fringe density f_0 results. If p is the pitch of the master (observation) grating and F is the image magnification then

$$\epsilon_{xx}(t) = [\frac{1}{f_x(t)} - \frac{1}{f_{x0}}]\frac{p}{F} \tag{2.3}$$

with Poisson's ratio given by

$$\nu(t) = -\frac{\epsilon_{xx}(t)}{\epsilon_{y0}} \tag{2.4}$$

for

$$\epsilon_{y0} = [\frac{1}{f_y} - \frac{1}{f_{y0}}]\frac{p}{F} \tag{2.5}$$

so that with $f_{x0} = f_{y0} = f_0$ and a constant f_y

$$\nu(t) = -\frac{1/f_x(t) - 1/f_0}{1/f_y - 1/f_0}. \tag{2.6}$$

One derives from this a relative error due to the errors in $f_x(t)$ and f_y (f_0 remains constant for all measurements) as

$$\frac{d\nu}{\nu} = [\frac{df_x/f_x(t)}{1 - f_x(t)/f_0}] + [\frac{df_y/f_y}{1 - f_y/f_0}] \tag{2.7}$$

which interprets into a $\pm 10\%$ error bound if the denominators are averaged over the range of the experimental data.

2.4.2 Measurements of the Uniaxial and Shear Response on Tubular Specimens

Material and Specimen Preparation

The material for this portion of study was commercially cast PMMA stock of 38 mm diameter (ACE, now a part of Ono, $T_g = 105°C$). Cast instead of extruded rods were chosen so as to avoid possible anisotropy due to molecular alignment incurred during processing. Each rod, delivered in 152 cm lengths was cut into blanks roughly one cm longer than the finished specimen length and the short rods were annealed in a Texaco ISO 46 hydraulic oil bath (boiling point=355°C) at 115°C for four hours and then cooled down to room temperature slowly by cutting the power to the temperature chamber; the cooling rate was about $5°C/hr$. This annealing process was necessary to remove the memory of thermal and loading history stored in the material during the casting process[3]. Tubular specimens with an outer diameter of 25.15 mm and an inner diameter of 19.05 mm were machined from these rods. During the machining process, coolant was constantly circulated in order to avoid damage due to overheating. The finished specimens were annealed again in the hydraulic oil bath at 115°C for 4 hours to remove the residual stress built in on the surface during the machining process.

As demonstrated by Knauss and Kenner (1980) the moisture content in amorphous polymers can have a significant effect on the viscoelastic behavior. The volumetric dilatation due to moisture content has the same effect on the creep behavior as temperature if the induced volumetric deformations are the same. To avoid this, the specimens were stored and used at the same relative humidity at all times. An environment of 6% of relative humidity at room temperature was produced via a saturated sodium hydroxide solution within an enclosed belljar (Lide, 1995). The annealed PMMA specimens were stored for two weeks prior to use. The weight of

[3]It was found that if the rod was not annealed before machining, the finished specimen would deform after annealing subsequent to the machining.

each specimen was measured every few days and found to decrease initially but to remain constant after three days (Mettler electronic balance, model HL 32 with an accuracy of $0.001g$). During the measurements the relative humidity was maintained at 6%. Excepting the time when the specimen was taken out from the belljar and placed into the environment chamber the specimen was always in an environment of 6% of relative humidity.

Digital image correlation (Lu, Vendroux and Knauss, 1996) was used to monitor the surface deformation of the specimen. This method requires a uniformly random speckle pattern on the specimen surface which is attained by first uniformly spraying (Krylon) flat white spray paint on the specimen surface to generate a white background and by subsequently splattering on black paint with the help of a toothbrush.

Physical Test Arrangement

The same MTS test system and Russell's environmental chamber were used in the measurements of the uniaxial and the shear relaxation moduli. An image acquisition system consisting of a Nikon 200 mm $f/2$ with a 52 mm objective, a Sanyo CCD camera with 640×480 $pixels$ spatial resolution and 8 $bits$ of gray scale, a Data Translation monochrome frame grabber (model DT2855) and a personal computer ($486,\ 66MHz$) was used to automatically acquire digital images at pre-determined times during the experiment. The acquired images were processed later using the digital image correlation method (Lu, Vendroux and Knauss, 1996). An air hole drilled in the lower grip allowed the air inside the hollow cylinder to circulate and equilibrate with the surrounding temperature[4].

[4]We mention peripherally that the application of a fixed end rotation of the cylinder produced a steady shear strain in the specimen. This was established with digital image correlation, which yielded very constant strain values with time and in agreement with the value derived from the end rotation.

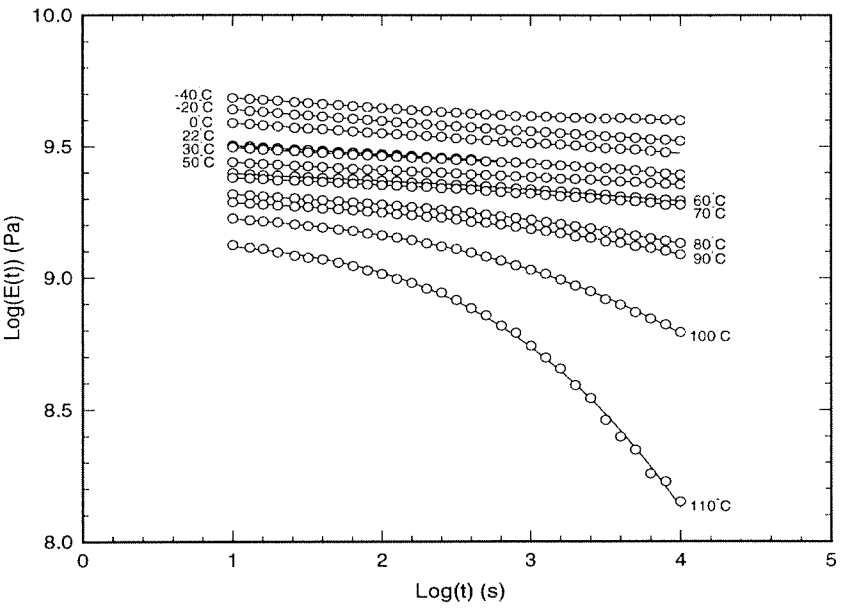

Figure 2.3: Uniaxial relaxation modulus for the Rohm & Haas Material (*Aging time* = 10800 *s*)

2.5 Results and Discussions

2.5.1 Uniaxial Relaxation Modulus and Poisson's Ratio Measured of the Rohm & Haas Material (Plate Specimens)

The relaxation data for this material are shown in figure 2.3 for different temperatures, and the corresponding Poisson data in figure 2.4. Following McLoughlin/Tobolsky (1952) and Williams/Landel/Ferry (1955) the relaxation data is shifted along the log-time axis to obtain the best-fit master curve in figure 2.5 and the Poisson data shifted by identical amounts in figure 2.6 with the shift factor recorded in figure 2.7. Although there is no common understanding or agreement that such shifting in the glassy region is valid, it has been observed to hold for several materials (e.g., see for PVAc, Emri and Knauss 1981 and an epoxy, Matsukawa, *et al.* (1992)), though the existence of a pronounced $\beta-$transition might be cause for concern.

The master relaxation curve is fairly smooth in terms of experimental error, how-

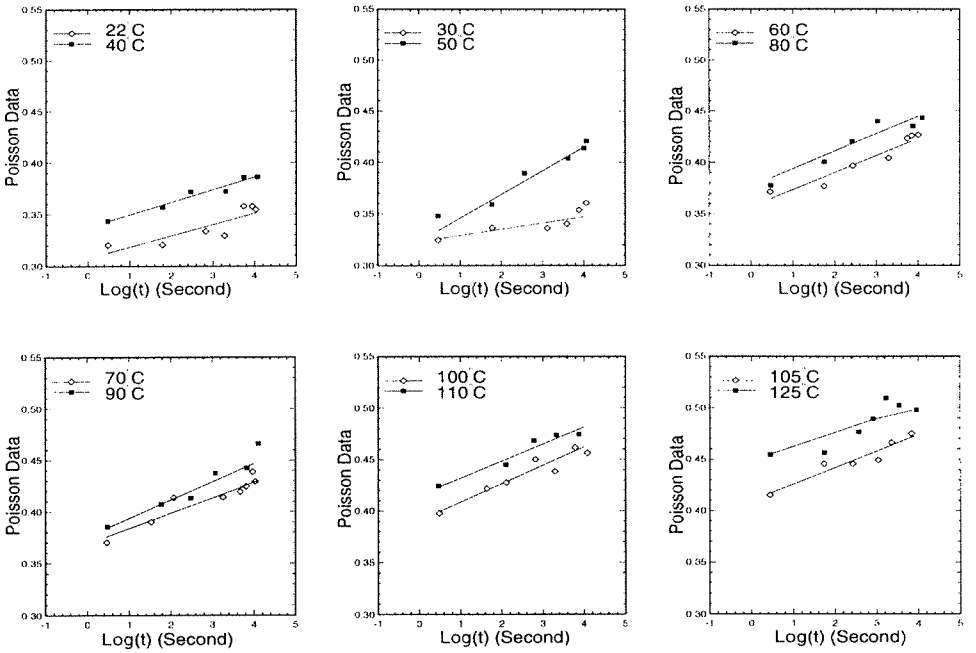

Figure 2.4: Poisson data at different temperatures (Rohm & Haas material)

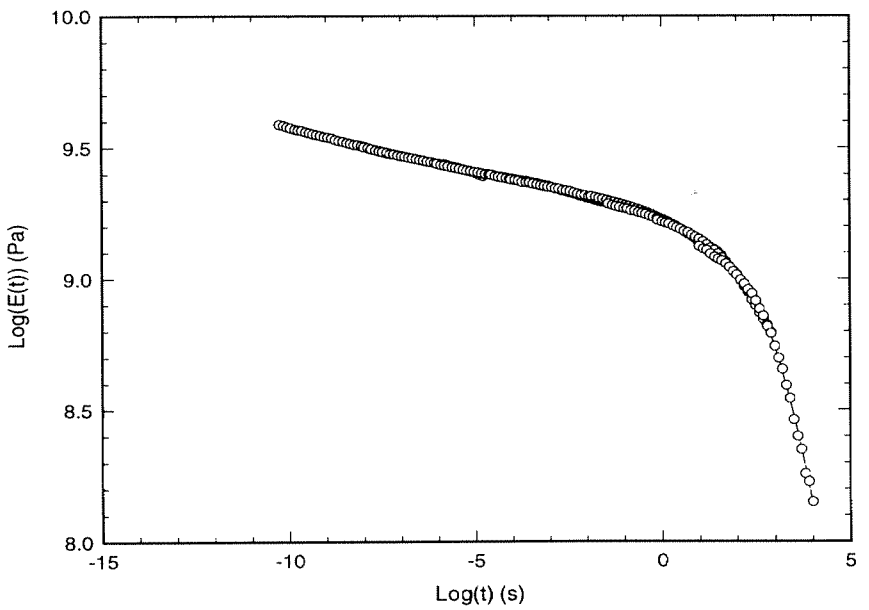

Figure 2.5: Master uniaxial relaxation modulus referred to $110°C$ (Rohm & Haas material)

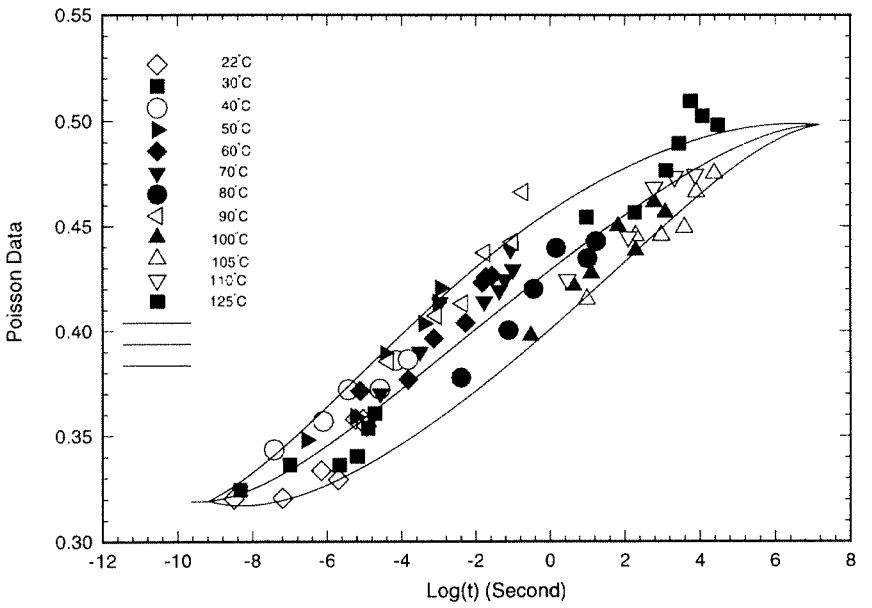

Figure 2.6: Poisson master curve with shift consistent with $E(t)$

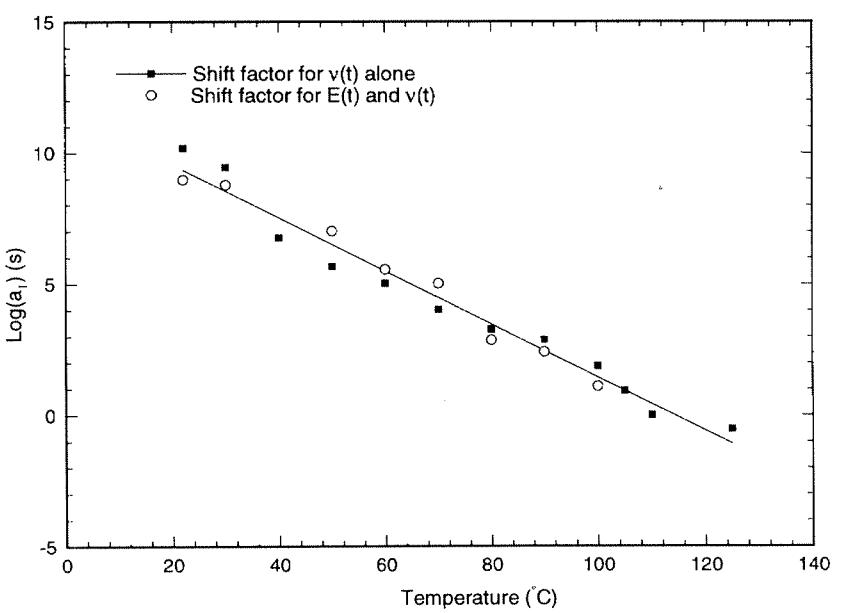

Figure 2.7: Shift factors for the uniaxial and Poisson Data

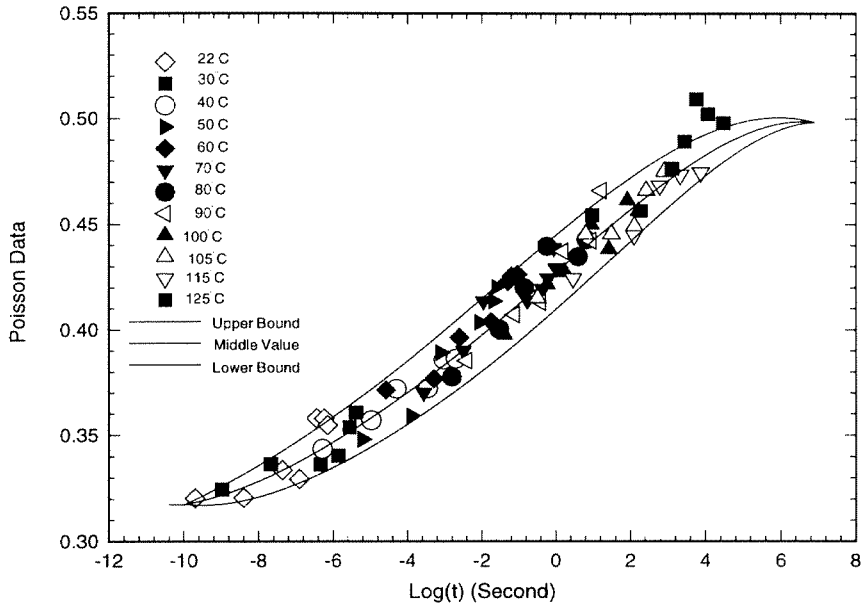

Figure 2.8: Best fit Poisson master curve

ever, the master curve for the Poisson data is not. This is due to the error incurred in measuring the extremely small transverse strains (between 0.06% and 0.1%) for a Poisson's ratio between 0.3% and 0.5% for most polymers when only 0.2% of axial strain is applied. It seems also reasonable to log-shift the Poisson data at different temperatures so as to produce a "best fit master curve" independent of the modulus data, as shown in figure 2.8 with the shift factors shown in figure 2.7. The Poisson master curve produced in this way is more narrowly bounded.

The question arises whether the shift factor for the uniaxial modulus and Poisson's ratio data are intrinsically different. Since the error bound for Poisson's ratio is $\pm 10\%$, and a smooth master curve can be generated within the error band, the evidence is not sufficient to determine at this time whether the shift factors for uniaxial relaxation and Poisson data are the same or not.

Using this data (figure 2.8) one obtains the bulk modulus via equation (2.1) as recorded in figure 2.9. The error band is small at short times but increases over

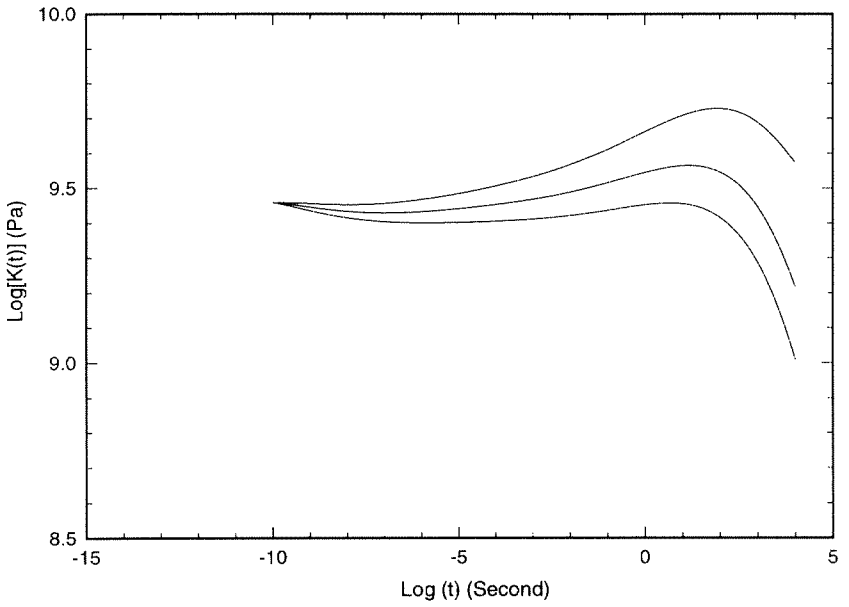

Figure 2.9: Bulk modulus computed from $E(t)$ and $\nu(t)$. The three curves correspond to the average, upper and lower bounds in figure 2.8

time. At $t = 10^4$, the bulk modulus in the upper bound is 3.67 times of that in the lower bound. The actual bulk modulus might be between the upper and lower bounds. However, these bounds are too large to be able to provide useful bulk data for practical use. Since the actual variation of bulk modulus over a wide range of time (or frequency) has been determined to be small[5] (1989) , the results computed from $E(t)$ and $\nu(t)$ would not be more accurate than a fictitiously constant bulk modulus. This observation casts serious doubt on the validity of computing the bulk modulus from the uniaxial relaxation modulus and Poisson's ratio. A simple quasi-elastic estimate renders from

$$k = \frac{E}{3(1-2\nu)},$$

[5]It has been determined by McKinney and Belcher (1963) that for PVAc, the dynamic storage compliance decreases by less than 50% over 12 decades of frequency. Recent measurements by Deng and Knauss (1996) render a ratio of 2.8. While Lin and Nolle (1989) determined the ratio as 2.7 ($0°C$ <temperature< $550°C$).

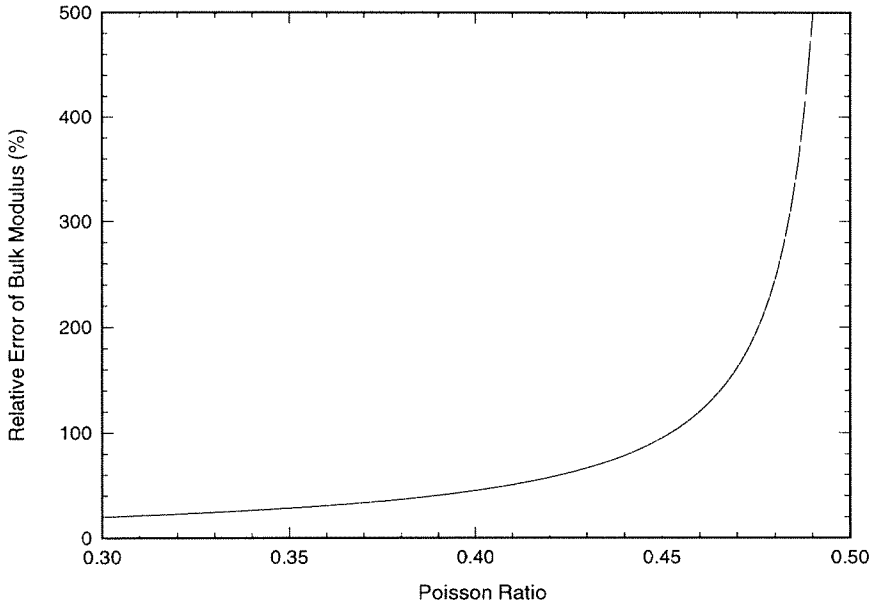

Figure 2.10: The error bound of K computed for an elastic solid from E and ν

that the relative error in K is, in terms of relative errors in E and ν

$$\left|\frac{dk}{k}\right| \leq \left|\frac{dE}{E}\right| + \frac{2\nu}{1-2\nu}\left|\frac{d\nu}{\nu}\right|. \tag{2.8}$$

For a reasonably good measurement one may expect a 5% of error in E and 10% of error in ν. For theses error bounds in E and ν, the relative error in K is plotted in figure 2.10 as a function of ν for $0.3 < \nu < 0.49$ which covers most polymers. This error is much higher than the errors in E and ν and increases rapidly as ν approaches 0.5; at $\nu = 0.49$ it reaches 500%! This large error makes it unrealistic to expect a reasonable determination of K from measurements of E and ν, especially at temperatures near the glass transition when Poisson's ratio approaches 0.5. In fact, one computes from equation (2.8) readily that for a relative error in the uniaxial modulus and an expected error of 5% for the bulk modulus that Poisson's ratio must be determined with a precision on the order of 10^{-4} as the rubbery plateau is approached ($\nu \to 0.499$), experimentally a more than daunting task.

2.5.2 The "Short-Time (Glassy) Limit" of the Relaxation Modulus

The uniaxial modulus was also determined through ultrasonic measurement at room temperature by determining the wave speeds of a longitudinal and a shear pulse at a frequency of $5MHz$; the uniaxial modulus and the Poisson's ratio were found to be $6.1GPa$ and 0.33. By way of comparison, the uniaxial modulus obtained in tension at a strain rate of $0.1\%/min$ was $3.1GPa$. This large difference in the moduli measured at different strain rates suggests that the moduli of PMMA at room temperature ($22°C$) are still rate dependent, rather than reaching a glassy plateau, an observation indicative of the well-established extended $\beta-$transition in PMMA. One may expect thus that the relaxation process will proceed even at temperatures very much below the glass transition. Consequently, the uniaxial relaxation modulus was measured at suitably low temperatures, and the data from $-40°C$ to $0°C$ are included in figure 2.11. More data may be found in Lu and Knauss (1997). It is clear that the relaxation process is still significant at a temperature that is $145°C$ below the glass transition, contrary to the widely accepted concept that the relaxation is negligible at such low temperatures. See also experiments by Rush (1968)

2.5.3 Uniaxial and Shear Relaxation Data for ACE Material; (Tubular Specimens)

Figures 2.11 and 2.12 show the uniaxial and shear relaxation moduli at different temperatures for the ACE material. The shift factor in figure 2.13 transforms this data into the master curves (figures 2.14 and 2.15) which are rather smooth in terms of experimental error.

To illustrate the uncertainties in determining the bulk modulus from such measurements it suffices to show this computation for the room temperature data over three decades of time, as shown in figure 2.16. These computations are based on numerically evaluating convolution integrals and illustrate the sensitivity of the bulk

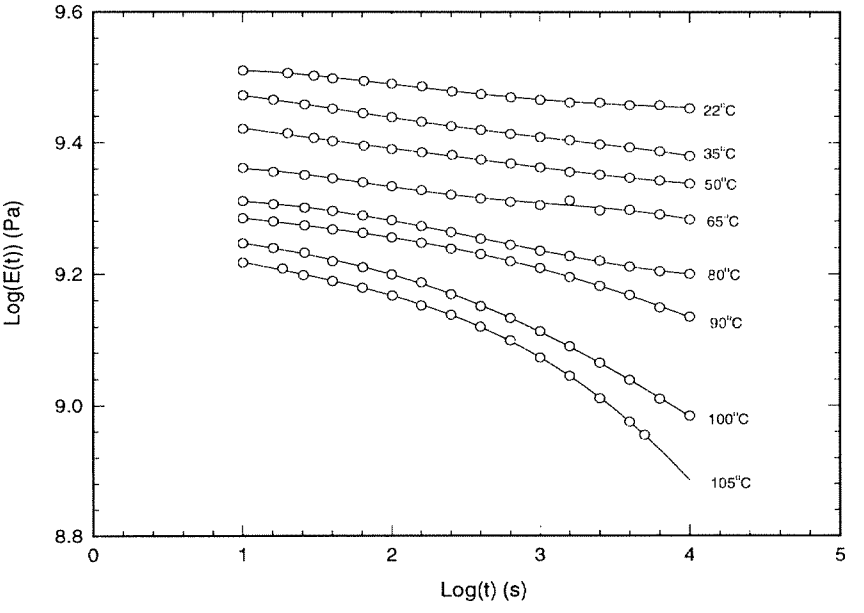

Figure 2.11: Uniaxial relaxation modulus (*aging time* = 172800 *s*)

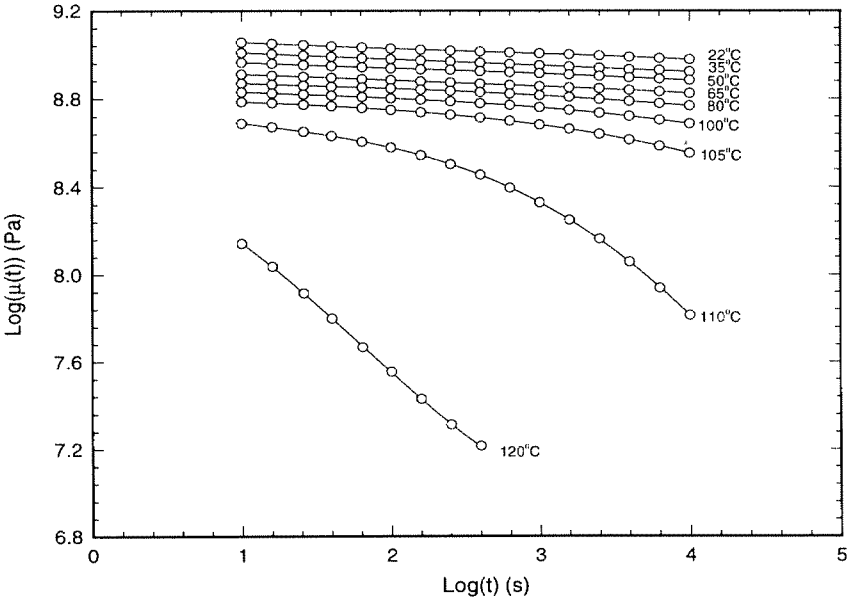

Figure 2.12: Shear relaxation modulus at different temperatures

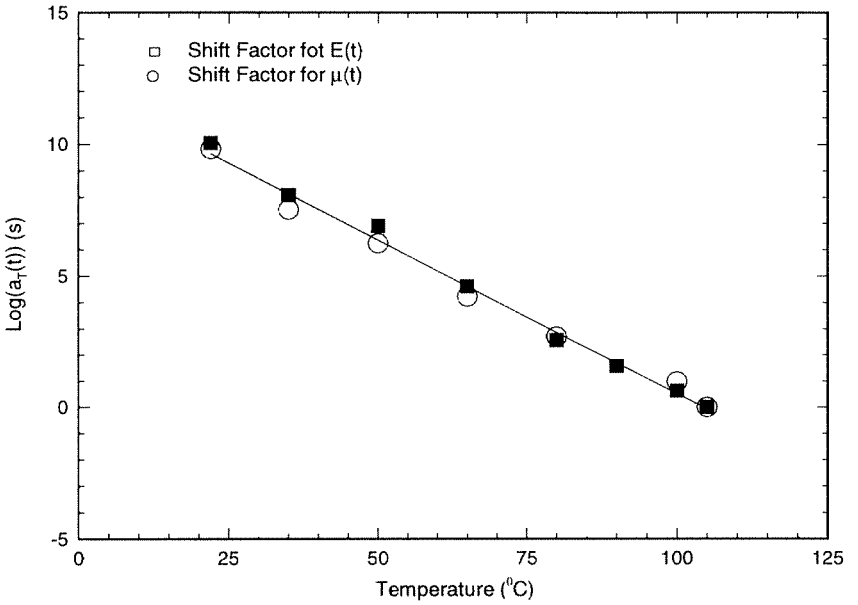

Figure 2.13: Shift factors for uniaxial and shear relaxation moduli

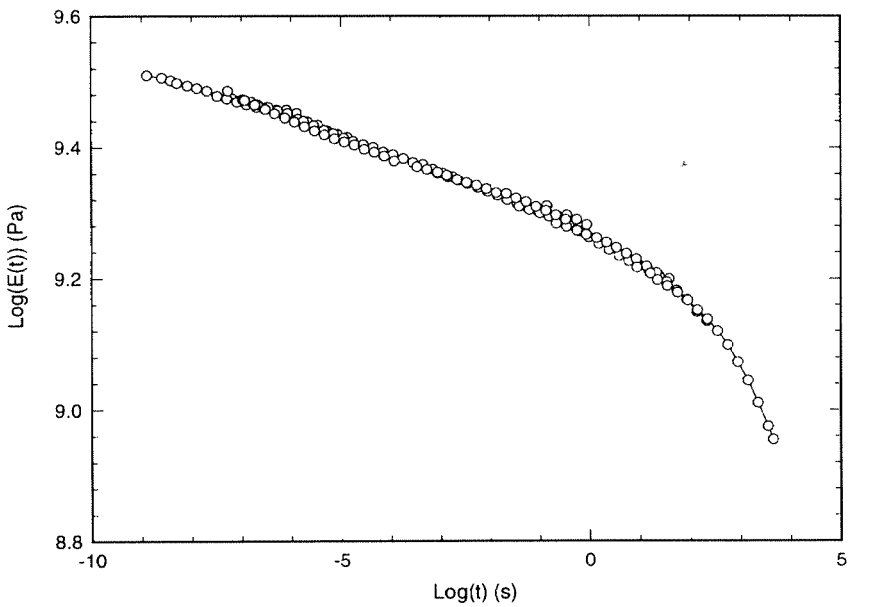

Figure 2.14: Uniaxial relaxation modulus referred to $105°C$

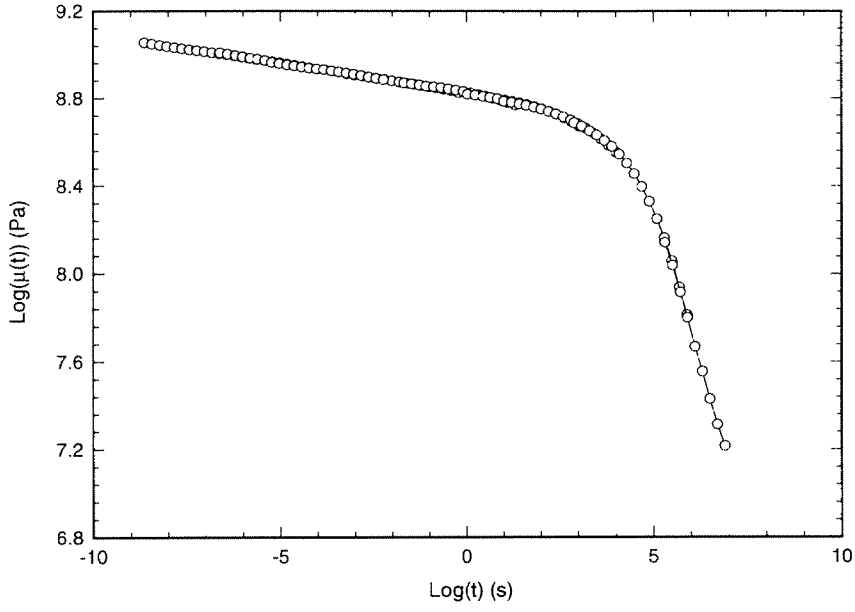

Figure 2.15: Shear relaxation modulus referred to 105°

behavior to errors in the shear modulus in two ways: Assuming the uniaxial modulus $E(t)$ to be error-free, the measured shear modulus in that figure, $\mu(t)$, yields a strongly increasing bulk characteristic. Alternately, assuming a (very) small "correction" to the shear modulus in the form of $\mu_a(t)$, as shown in that figure, brings the relaxation behavior of the bulk function "in line".

As a second way of illustrating the sensitivity of the conversion computation one may use again quasi-elastic analysis to estimate the required accuracy on the shear modulus function in order to achieve a bulk modulus function within a prescribed range of precision. Using the elastic relation

$$k = \frac{\mu E}{3(3\mu - E)}, \tag{2.9}$$

one finds (for $dE = 0$) that the relative error in the shear modulus is given by

$$\frac{d\mu}{\mu} = (\frac{1}{2} - \nu)\frac{dk}{k} \qquad \text{as} \quad \nu \to \frac{1}{2}.$$

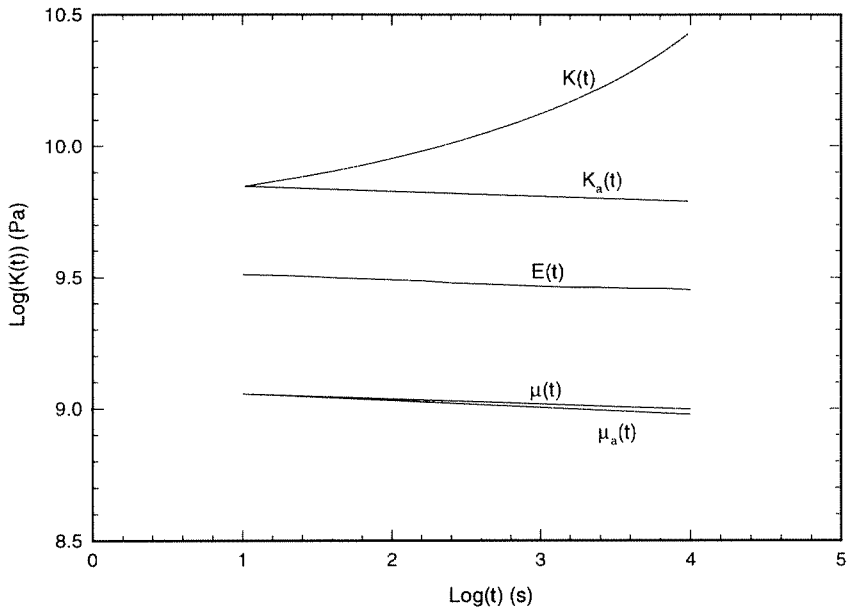

Figure 2.16: Sensitivity of bulk modulus to $E(t)$ and $\mu(t)$

Thus when approaching the rubbery domain ($\nu \to \frac{1}{2}$), the shear modulus would have to be determined with about thousand fold precision relative to the desired bulk modulus precision. This requirement is impossible to meet experimentally.

2.5.4 Additional Comparison of Measured and Converted Functions

Let us conclude this presentation with two (limited) comparisons, one for the two uniaxial relaxation measurements, and one which inverts this relaxation modulus to the creep compliance for comparison with experimental creep data. The relaxation data compiled from the two materials (Rohm & Haas and ACE) are juxtaposed in figure 2.17. The agreement is not "perfect" because one deals here with two different sources of material without detailed molecular identification. More importantly, one should bear in mind that these results derive from measurements at different relative humidities. While no detailed study of the quantitative effect of humidity on the rheological behavior was intended here, one notes that the differences are certainly

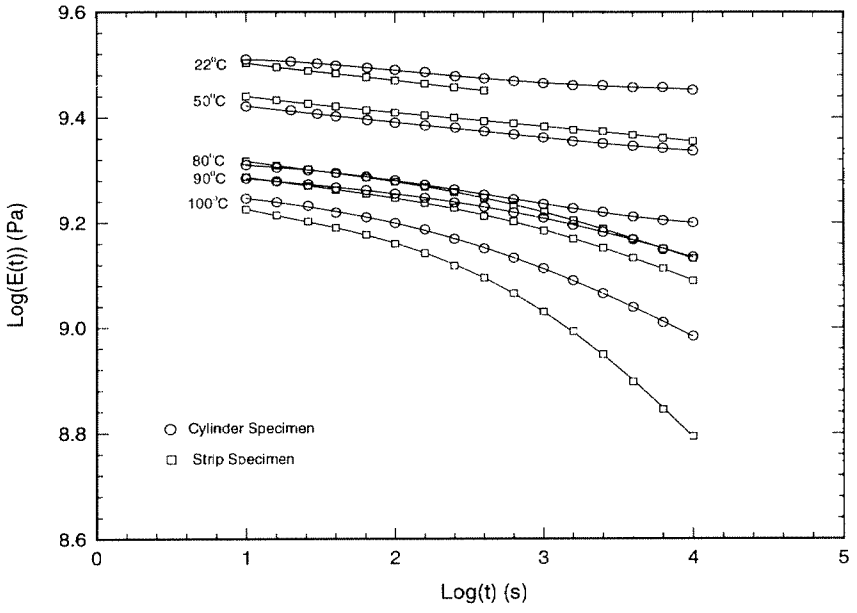

Figure 2.17: Comparison of the relaxation moduli measured from two kinds of specimens

consistent with the different environments.

In figure 2.18 the shear creep compliance as measured at $22°C$ for the ACE material is compared with the creep compliance for the same material, but as computed from the shear relaxation modulus for the same solid. Within experimental error, the agreement appears acceptable. One only notes that there appears to persist a systematically larger slope for the measured creep behavior which occurred at an increasing strain larger than that used to determine the relaxation behavior. This (slight) difference is believed to be a vestige of nonlinear behavior, inasmuch as similar comparisons at higher temperatures incur larger creep strains than those are typically used in relaxation measurements, and the creep measurements deviate consistently from those computed from the relaxation data by increasingly exhibiting both larger slopes as well as larger values. Discussion of this type of comparison exceeds the purpose of this presentation and the reader is referred to a more detailed discussion on this topic in Lu and Knauss (1997).

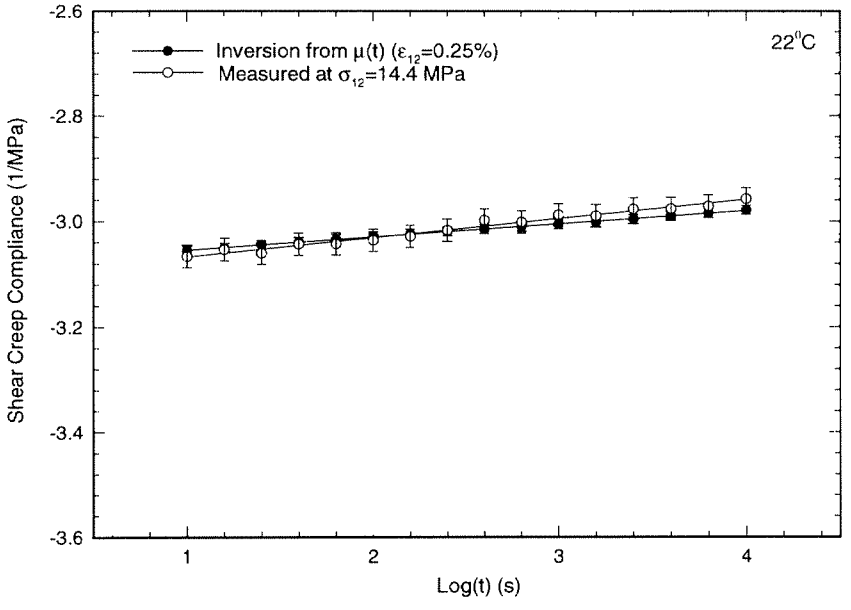

Figure 2.18: Creep compliance at $22°C$

2.6 Conclusion

Normally accessible viscoelastic material functions have been measured by means of relatively straightforward experimental methods and it has been illustrated that standard measurement accuracy is totally inadequate to allow conversion of these properties to bulk-related time dependent behavior. Computations indicate and experimental data support the idea that the relative error in bulk data is extremely sensitive to errors in other material functions ($E(t)$, $\mu(t)$ and $\nu(t)$). Direct measurements over a wide range of temperatures and times (or frequencies) are thus necessary to determine the bulk behavior.

Chapter 3 Nonlinearly Viscoelastic Behavior of PMMA under Multiaxial Stress States

Abstract

The nonlinear thermo-mechanical behavior of Polymethyl Methacrylate (PMMA) under combined axial (tension, compression) and shear stress states (torsion) is investigated on thin-walled cylindrical specimens at temperatures between 22° and 110°C. In contrast to the mutual independence of shear and dilatational response under conditions appropriate for linearized viscoelasticity, one observes an increasingly strong coupling between all deformation or stress invariants as assessed in creep experiments for strains in excess of 0.5%. While shear stresses alone elicit "intrinsically" nonlinear response in creep (rates), the addition of positive dilatation accelerates shear deformations while negative dilatation retards them in quantitative agreement with free volume arguments above and in a range about Tg. Passing below the glass transition still produces significantly greater creep acceleration from positive dilatation than from a decrease in specific volume, but the dominance of the intrinsic shear nonlinearity vis-a-vis the dilatational influence increases below T_g as the temperature drops. A limited set of pure shear data suggests that the creep strain can be represented as the sum of a component following linearly viscoelastic behavior and a component that is (nearly linearly) proportional to a critical stress exceedance (overstress) with a power law function of time.

3.1 Introduction

In spite of the tremendous increase in polymer applications to engineering problems there exists a surprising lack of knowledge regarding polymer nonlinear behavior at elevated load or deformation levels. To date, uniaxial stress or simple shear fields serve almost exclusively to characterize the mechanical properties of these materials. Such a simplistic approach to material characterization is clearly inadequate when large strains and high stresses are involved that can and will lead to structural failure/fracture. For example, crack propagation is an important aspect of evaluating the strength and life expectancy of polymeric structures. While linearly viscoelastic crack propagation models exist (Müller and Knauss, 1971; Knauss, 1974; Schapery, 1975) which correspond roughly to the Griffith model for rate independent, brittle fracture, their extension to nonlinearly viscoelastic material behavior cannot be investigated realistically because the nonlinearly viscoelastic description of the material constitution for arbitrary (uniaxial and multiaxial) loading histories and environmental (temperature, moisture content, etc.) conditions is not available. It is thus not possible to expand the investigation of linearly viscoelastic fracture models to nonlinear material behavior, similar to how plasticity considerations have extended the application of linear fracture mechanics to the engineering metals.

While there exist numerous investigations on the nonlinear time dependent behavior in one dimensional stress or strain states (sometimes superposed on pressure), investigations on the nonlinear viscoelastic behavior under multiaxial stress states are sparse. Most are restricted to the formulation of yield or flow rules modeled after (volume preserving) plasticity (Thorkildsen, 1964; Sternstein, 1969; Carapellucci, and Yee, 1986) under neglect of time dependence or evolutionary material characteristics. While this behavior is typically based on equivoluminal deformation behavior, that characteristic does not apply to polymers.

Polymer nonlinear viscoelastic behavior is also different from the pressure sensitive plasticity (Sternstein and Ongchin, 1969), where the yield-like[1] criterion is proposed as

$$\tau - \mu\sigma = \tau_{crit}. \tag{3.1}$$

τ and σ are equivalent stress and isotropic stress, respectively, τ_{crit} is a yield-like stress. μ has been determined to be around 0.15 for certain polymers at temperatures well below the glass transition. Though the isotropic stress is incorporated into the yield-like criterion, the flow rule is usually treated as pressure insensitive, because it is usually considered that μ is small so that the contribution from the isotropic stress may be neglected at low temperatures. However, these conclusions do not agree with the observations made on multiaxial creep behavior in which the contribution of volumetric deformation increases over time and temperature.

Very few results are reported on time dependent polymer behavior under multiaxial loading. Ewing, et al. (1972, 1973) investigated the creep behavior of polyethylene and found that under combined tension and torsion the equivalent stress is related isochronically to the "equivalent strain" by a power law under moderate strains, provided the material is considered incompressible (Poisson ratio=0.5) which is true at room temperature only for the amorphous phase. McKenna (1979) investigated the torsional relaxaion behavior of Poly(methyl) Methacrylate cylinders under constant length constraints at room temperature, and measured the resulting dilatation and axial force as a function of time.

In contrast to the pressure insensitivity in metal plasticity, the volumetric deformation in polymers plays an important role in controlling the "yield-like" behavior in polymers. There is ample evidence that at least around and above the glass transition volumetric changes affect the material time scale (internal clock) whether these

[1]It is not appropriate to use "yield" that is used typically for metal materials to describe the "yield-like" behavior in polymers because the "yield-like" behavior in polymers is the evolutionary character of the viscoelastic response rather than a physical process.

changes derive from moisture absorption (Knauss and Kenner, 1980) or mechanical pressure (Fillers and Tschoegl, 1977; Moonan and Tschoegl, 1983, '84, '85). The latter authors demonstrated experimentally, for example, that above T_g the classical time-temperature shift factor for (linearly) viscoelastic material characterization could be considered as a function of temperature or pressure induced volumetric deformation.

In this study the nonlinear time dependent shear (creep) behavior and its interaction with dilatationl effects is investigated and the degree to which the latter controls the nonlinearly viscoelastic response. Of particular interest is the effect of uniaxial tension or compression superposed on the response to shear loading. These effects are examined experimentally in biaxial stress states imposed on hollow cylinders. Because strain gauges cannot be used under high temperature conditions and since computing deformations from the end displacements and rotation angles may not be accurate when the possibility of inhomogeneneous deformations exists, a non-contact measurement technique based on digital image correlation (Sutton, 1983; Lu, Vendroux and Knauss, 1996) is used.

3.2 Experimental Preliminaries

Specimen Preparation: The material is commercially[2] cast rather than extruded PMMA stock of 38 mm in diameter to avoid possible anisotropy due to molecular alignment incurred during manufacturing. Blanks roughly one cm longer than the finished specimen length were annealed[3] before machining in Texaco ISO 46 hydraulic oil (boiling point=$355°C$) at $115°C$ for four hours and then cooled to room temperature at a cooling rate of about $5°C/hr$. During the cylinder machining process, coolant was circulated over the work piece to control any possible heating. The finished specimens were annealed again in the hydraulic oil bath at $115°C$ for 4 hours.

[2]ACE, now a part of Ono, $T_g = 105°C$

[3]It was found that if the rod was not annealed, the finished specimen would deform after annealing subsequent to the machining.

Specimen Dimensions and Poynting Effect: Two kinds of thin walled specimens[4] are used to avoid buckling in different temperature regimes. A thin-walled specimen (outer diameter $R = 22.23\ mm$, wall thickness $\lambda = 1.59\ mm$, test length= $88.9\ mm$, $\lambda/R = 0.14$) is used for the lower temperatures to reach shear strains on the order of 5% while the thicker wall (thick-walled specimen: outer diameter $R = 25.15\ mm$, wall thickness $l = 3.18\ mm$, test length=$76.2\ mm$, $\lambda/R = 0.29$). The specimen geometry is monitored continuously and all data are acquired without interference of buckling.

Specimen Re-Use and Aging: In order to minimize specimen-to-specimen variations the same thin walled cylindrical specimen is re-used at each temperature repeatedly which was made possible by annealing the specimens after each use. Care was taken to minimize the effect of physical aging (Struik , 1978; Gates, 1997). Lee and McKenna (1989) determined that at a certain time the polymer glass may reach a structural equilibrium state after which physical aging is not significant over several decades. A test series aimed at avoiding physical aging effects established boundaries for practically eliminating this phenomenon. Figure 3.2 shows example comparisons in terms of shear creep behavior at two temperatures; on the basis of such data specimens were aged at the test temperature after annealing typically for three days after annealing and prior to use.

Moisture Control: To control the influence of moisture variation (Knauss and Kenner, 1980), the specimens were stored and tested at the same relative humidity. A 6% relative humidity at room temperature was produced via a saturated sodium hydroxide solution within an enclosed belljar (Lide, 1995) in which the annealed PMMA specimens were stored for at least two weeks prior to use. The weight of each specimen was measured[5] at begining a few days and found to decrease initially but

[4]Axial strain will be generated that is proportional to the square of the shear strain due to Poynting effect (Poynting, 1912). For moderate shear deformation the Poynting effect is not expected to significantly affect the multiaxial behavior.

[5]Mettler electronic balance, model HL 32 with an accuracy of 1 mg.

to remain constant after three days. During the measurements the relative humidity was also maintained at 6% so that, excepting the time when the specimens were taken from the belljar and placed into the environmental chamber, they were always in an environment of 6% relative humidity.

Loading Arrangement: The experimental setup is shown in figure 3.1. An MTS 809 servo-hydraulic system with the dual capacity of 15 kN of axial load and 168 Nm of torque (calibrated to a precision of ± 0.5 N of load and 0.08 Nm of torque) was used to axially deform and twist the specimen, A customer-designed (Russell's) chamber provided an environment of constant temperature and relative humidity. The temperature being monitored continuously by a thermocouple close to the specimen assures a range of $\pm 0.2°C$ of the set temperature. The environmental chamber is activated at all times to control the temperature and humidity, even when the experiment is conducted at room temperature. The original standard furnace window glass of the Russell's environmental chamber was replaced by a single panel optically flat glass to reduce errors in the deformation measurements. The specimen, gripped by a well aligned fixture[6](see Appendix), was illuminated by two Halogen lights (Fuji, 12v, 20w) outside of the chamber so that the heat exposure of the specimen was minimal.

Axial load and torque were applied simultaneously to the specimen in ramp fashion (rise time =1 s) and the corresponding surface image patterns were recorded by an image acquisition system which used a Sanyo CCD camera possessing a spatial resolution of 640×480 $pixels$ and an $8-bit$ gray scale. Images were processed by the digital image correlation method (Sutton, 1983, 1986; Vendroux and Knauss, 1994; Lu, Vendroux and Knauss, 1996) to extract the surface deformations. For a cylinder of diameter 22.23 mm this rendered a resolution of 0.05% in axial and shear strains and 0.08% in circumferential strain (Lu, Vendroux and Knauss, 1996).

[6]We are indebted to Dr. T. Nicholas of the Wright Laboratories for providing the basic design.

Figure 3.1: Experimental setup

Stress/Strain Distribution: End effects and nonlinearity in the axial direction of the specimen are not important here since strains were measured locally. The surface stresses for a cylindrical specimen with an outer radius R and inner radius r under an axial force F and a torque T are given by

$$\left.\begin{aligned} \sigma &= \frac{F}{\pi(R^2 - r^2)} \\ \tau &= \frac{TR}{\frac{\pi}{2}(R^4 - r^4)} \end{aligned}\right\} \tag{3.2}$$

The axial and shear compliances[7] ($D(t)$ and $J(t)$) are defined by

$$\left.\begin{aligned} D(t) &= \frac{\epsilon_{xx}(t)}{\sigma} \\ J(t) &= \frac{2\epsilon_{x\theta}(t)}{\tau} \end{aligned}\right\} \tag{3.3}$$

Equations (3.2) are derived from the linear theory of viscoelasticity shich yields a linear distribution of shear stress over the radial coordinate. This behavior is not correct when a portion of the material in the specimen enters the nonlinear range.

[7]The (axial or shear) creep compliance in linearized viscoelasticity (appropriate for infinitesimal deformation) is a material function. In moderate deformations generating nonlinear material response, this "creep compliance" does not represent the basic material property but the terminology is still used here for reasons of expediency.

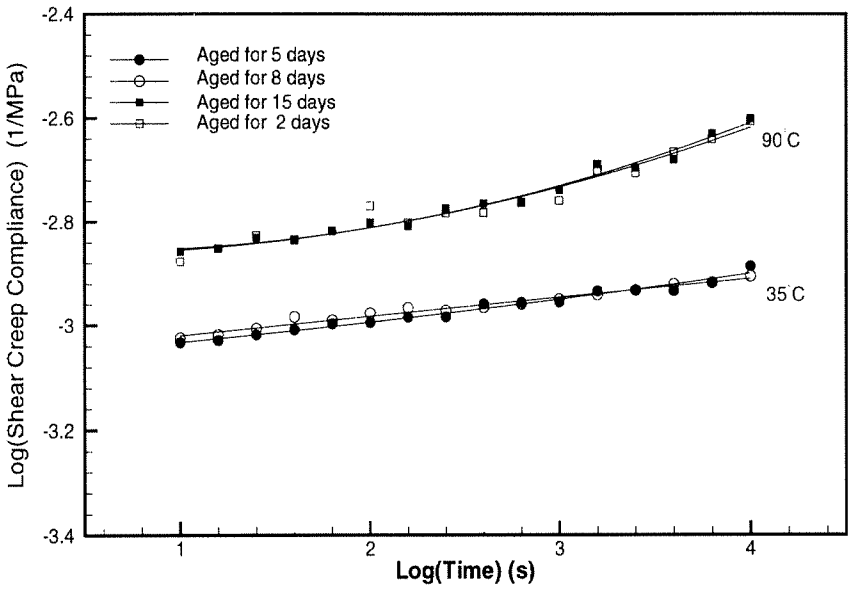

Figure 3.2: Shear creep compliance at $35°C$ and $90°C$

However, for the specimens used, the variation in the shear stress across the wall thickness is small ($\pm 7\% - \pm 14.5\%$) and are, therefore, assumed to have secondary importance.

3.3 Results

The presentation of results divides naturally into the characterization of pure shear deformations and their modification by superposed axial stresses. We present first the results for

Shear (Torsion) only

and examine subsequently modification of that response under superposed tension or compression. The shear creep compliances for different stress levels at $22°C$, $35°C$, $80°C$ and $100°C$ are shown in figures 3.3 through 3.7. To compare the creep compliances with the behavior under infinitesimal deformation, we derive the "linear" or

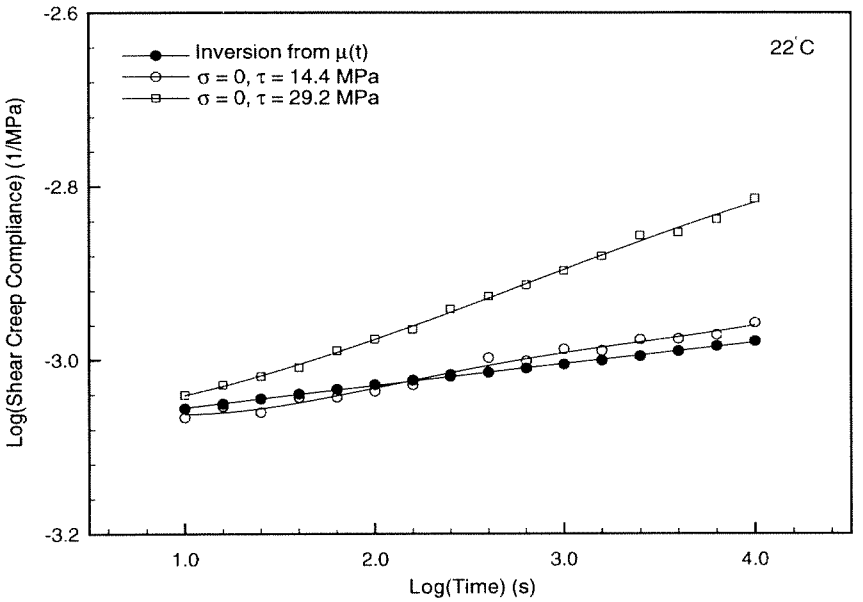

Figure 3.3: Shear creep compliance at $22°C$

"small deformation" compliances from relaxation behavior at strains of 0.25% (Lu and Knauss, 1996) and these are included in the figures[8], identified by solid circles. Since these curves are obtained from small deformations, they represent a basic material property and are (by assumption) stress and strain independent in the linearly viscoelastic regime.

Isochronic Stress-Strain relation at $80°C$

Because data for the largest number of stress levels have been accumulated for $80°C$ we examine first the behavior at that temperature. Figure 3.8 shows the isochronic stress-strain response of the data in figure 3.6. The two lines emanating from the origin represent a (linear) fan encompassing the linearly viscoelastic behavior for the duration of experiments. The remaining data are also fitted by straight lines. While a least square fit to each isochronic curve would not necessarily

[8]The inversion was performed via a code written by I. Emri and modified by L.C. Brinson based on the Hopkins-Hamming algorithm (Hopkins and Hamming, 1957).

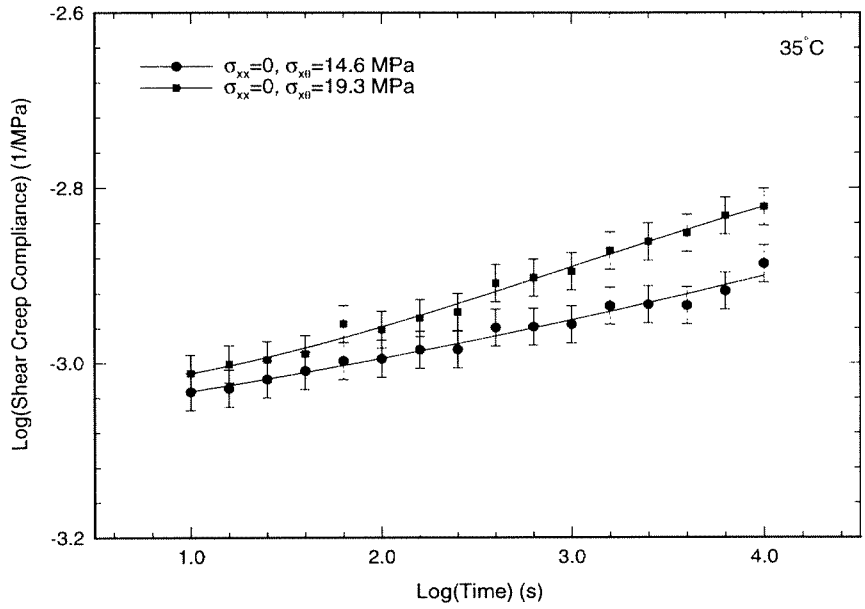

Figure 3.4: Shear creep compliance at $35°C$

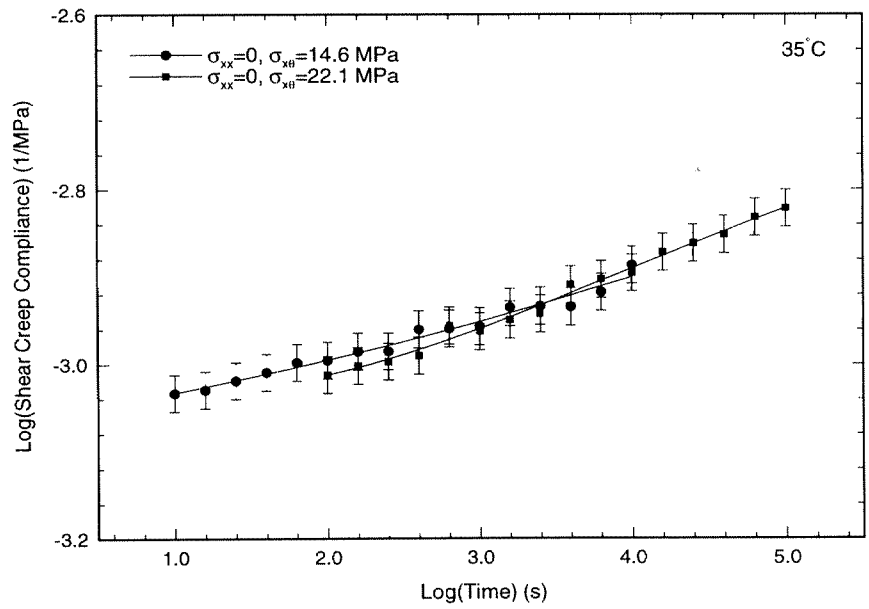

Figure 3.5: Tentative horizontal shift of the shear creep compliances at $35°C$

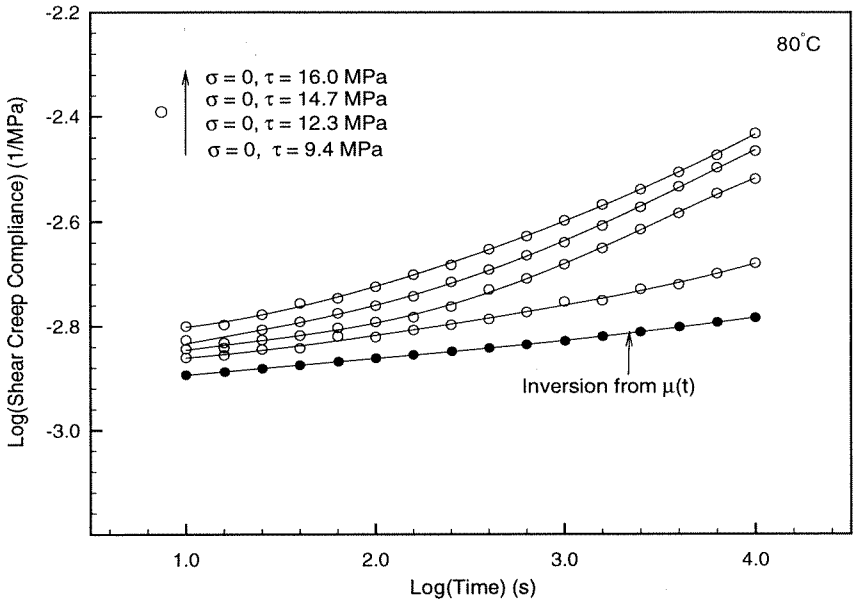

Figure 3.6: Shear creep compliance at $80°C$

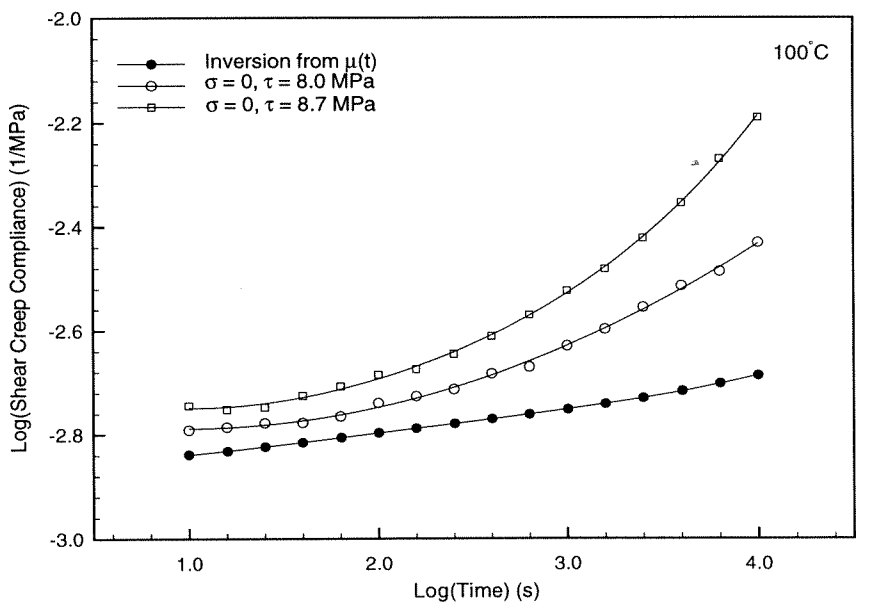

Figure 3.7: Shear creep compliance at $100°C$

produce a straight line, we find it illustrative and, in view of experimental uncertainties, admissible to represent these portions by straight line fits. It is observed that all the fitted straight lines intersect at a point or range that lies within the linear fan. Thus, for values of $\epsilon_{x\theta} > 0.4\%$ ($\tau > 8MPa$) accelerated creep occurs. This indicates that below a critical stress or strain value the material behaves essentially in a linear fashion while exceeding the critical value carries the material into the nonlinear range. This relationship is reasonably represented by

$$\epsilon_{x\theta} = \begin{cases} J_l(t)\tau & \epsilon_{x\theta} < \epsilon_0 \ or \ \ \tau < \tau_0, \\ \tau J_l(t) + (\tau - \tau_0)J_p(t) & \epsilon_{x\theta} > \epsilon_0 \ or \ \ \tau > \tau_0, \end{cases} \tag{3.4}$$

where τ_0 is the stress at the apex of the high-stress fan, $J_l(t)$ is the linear shear creep compliance and $J_p(t)$ is the time (power law) function shown in figure 3.9. It is left to future, more detailed studies of this phenomenological representation to establish any possible relation between $J_l(t)$ and $J_p(t)$, as well as rules for response under variable stress histories.

We present also the isochronic stress-strain curves for the other temperatures in figure 3.10. The curves at $22°C$ and $35°C$ represent features similar to $80°C$. At $100°C$ the fitted straight lines do not appear to intersect at the a point, which may indicate that at a temperature close to the glass transition the volume effect starts to emerge. The exponents of the J_p function are 0.10, 0.11 and 0.34 for $22°C$, $35°C$ and $100°C$ respectively.

It is next of interest to consider briefly the molecular mechanics responsible for this form of the constitutive shear behavior. It is clear that below a certain strain or stress value linearly viscoelastic shear behavior prevails. Inasmuch as the stress was constant for these tests it appears reasonable to think in terms of a critical stress level below which the molecular mechanicsms associated with small deformations prevail. Once this threshold has been passed additional molecular deformation mechanisms

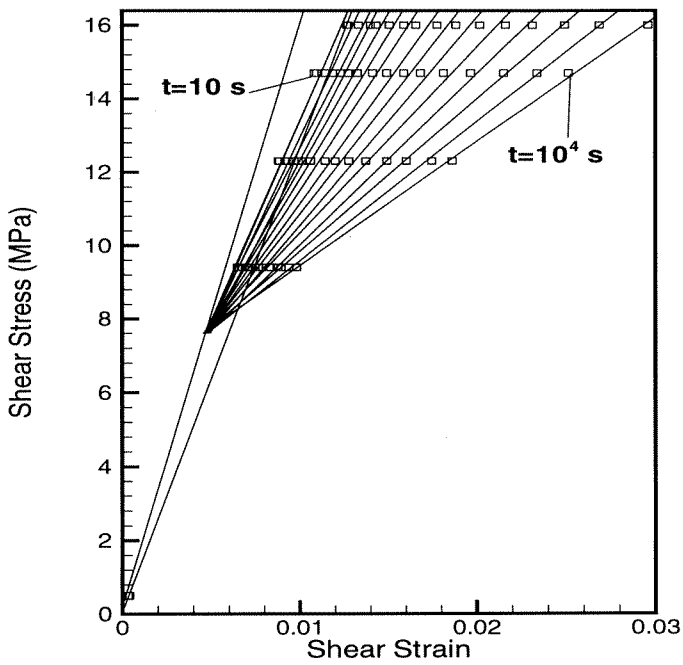

Figure 3.8: Isochronic Stress-Strain Relation at $80°C$

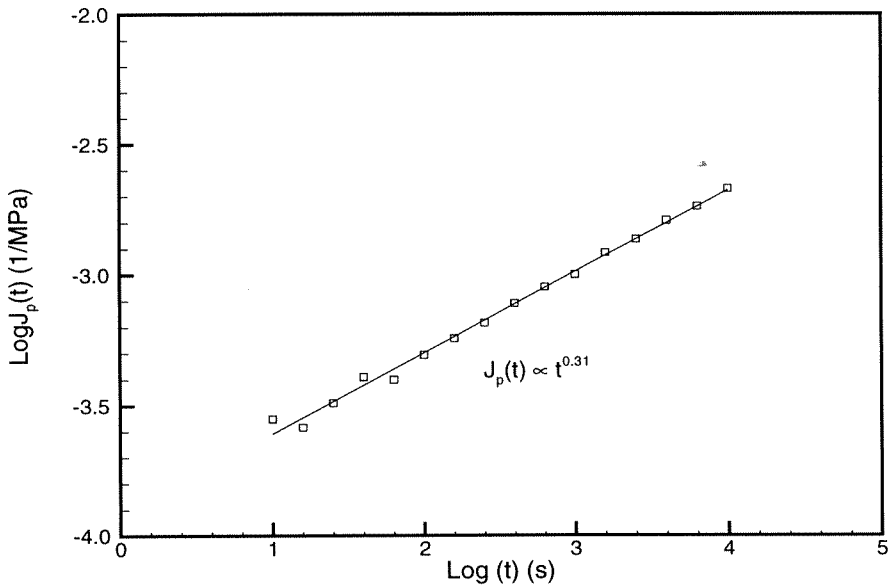

Figure 3.9: J_p at $80°C$

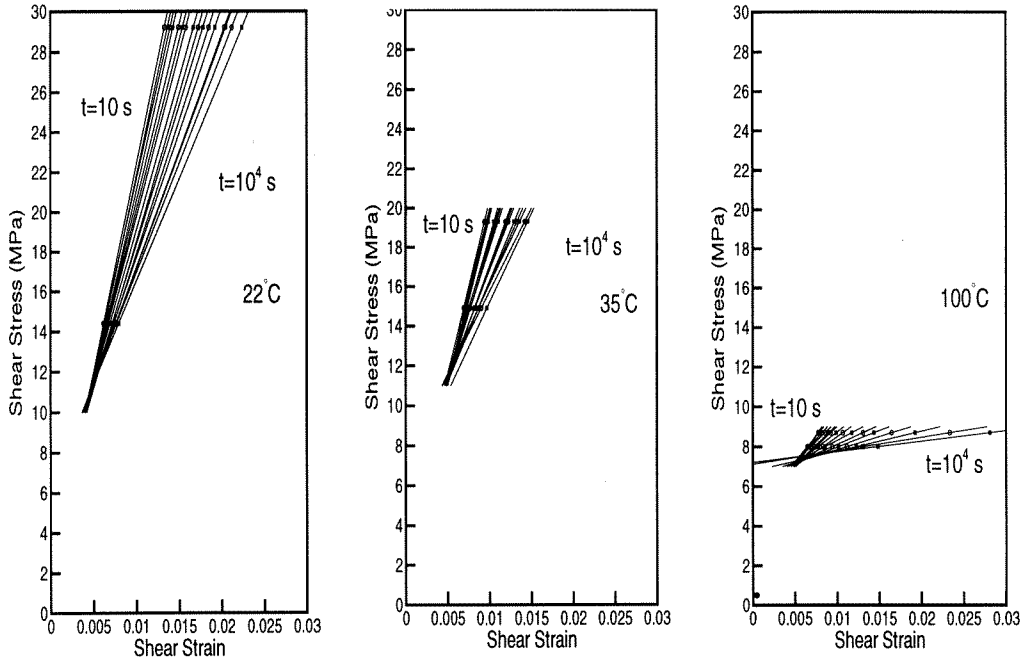

Figure 3.10: Isochronic Stress-Strain Relation at $22°C$, $35°C$ and $100°C$.

become available that add to the shear deformation. We think here in terms of molecular arrangements such as illustrated schematically (in two dimensions) in figure 3.11, but in which the chain flexibility is governed primarily by rotational degrees of freedom about the chain axis rather than by "backbone bending" (See also Argon, 1973). The activation of these mechanisms depends on the stress level, more of them becoming available to contribute as the global stress increases. In fact, the (nearly) linear increase in the nonlinear component (second term in equation 3.4) indicates that at least for the current range of data the number of such mechanicsm is directly proportional to the stress level, and that they all contribute with about the same (creep) time dependent response.

3.3.1 Multiaxial Stress States

In this section we present first the shear creep data above and near the glass transition range and then proceed to creep data well below the glass transition.

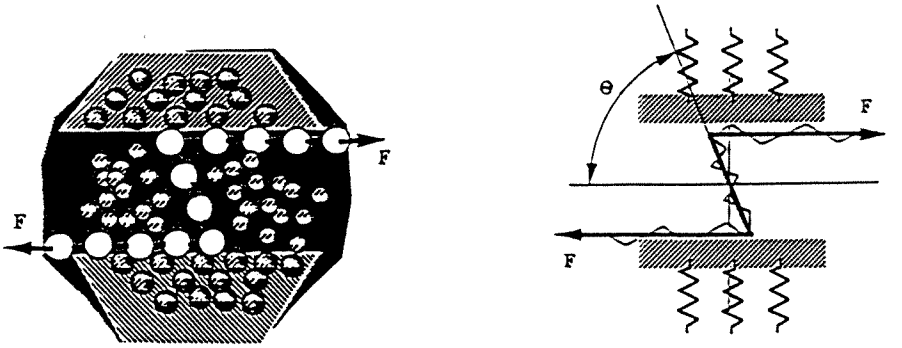

Figure 3.11: A "Z" shaped analog model representing the molecular arrangement

Figure 3.12 and 3.13 show the shear creep compliances under multiaxial loading at $100°C$ and $110°C$, both above the glass transition temperature ($T_g = 105°C$). It is apparent that the shear creep rate increases when a tensile stress is superposed on pure torsion at 100° and $110°C$[9]. While a superposed compressive stress reduces the shear creep rate at both $100°C$ and $110°C$[10].

These observations indicate that volume dilatation is a controling factor to the nonlinear viscoelastic response near the glass transition. While a positive dilatation increases the nonlinear viscoelastic response rate, a negative dilatation decreases the nonlinear viscoelastic response rate.

We turn next to the multiaxial creep behavior in the glassy state. Figure 3.14 show the creep compliance for a thin walled cylindrical specimen at $22°C$ subjected to a shear stress of 14.4 MPa and various axial stresses. Upon comparing the shear creep

[9]At $110°C$ the creep rate increased so much that the specimen soon buckled and broke.

[10]To confirm that the results observed at $110°C$ are not due to any nonanticipated effect of the prior specimen history, an additional uniaxial creep under a pure torsion with zero axial load is conducted with a new specimen. Figure 3.13 shows that the results obtained from two different specimens are reproducible. Multiaxial creep test under $\sigma = -9.5\ MPa$ and $\tau = 7.0\ MPa$ with a new specimen gives a slightly smaller shear creep compliance than that for $\sigma = -6.0\ MPa$ and $\tau = 7.0\ MPa$ and the shear creep compliances in both compression and torsion case is smaller than that for the pure torsion with the same magnitude of shear stress and zero axial load.

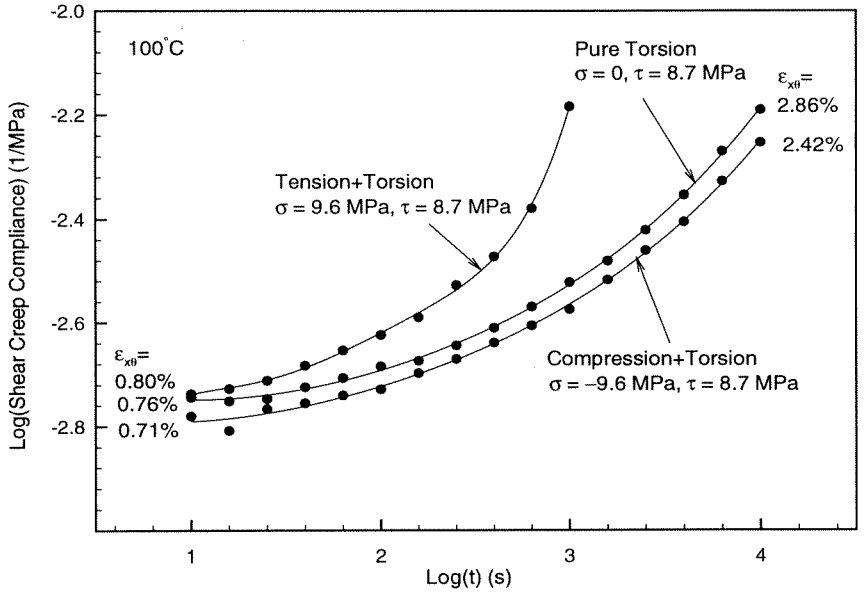

Figure 3.12: Shear creep compliance at $100°C$

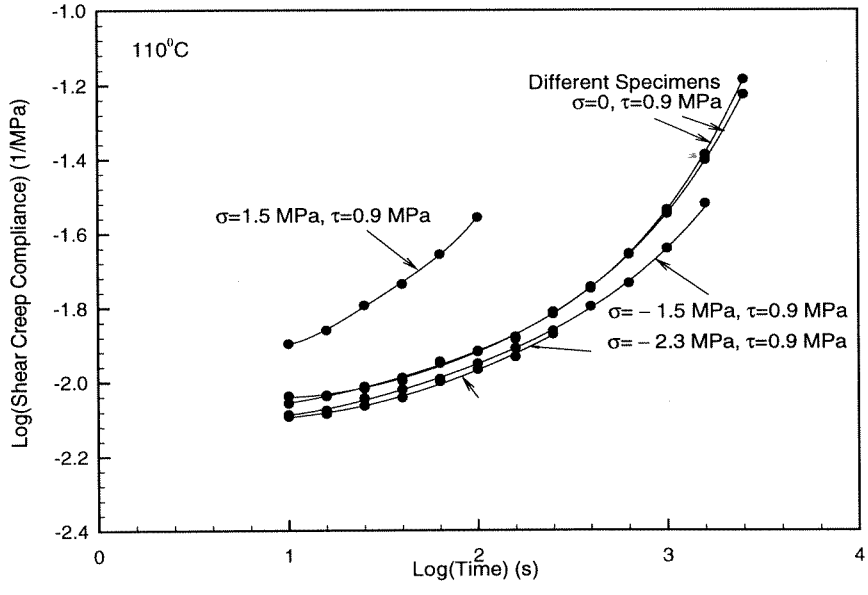

Figure 3.13: Shear creep compliance at $110°C$

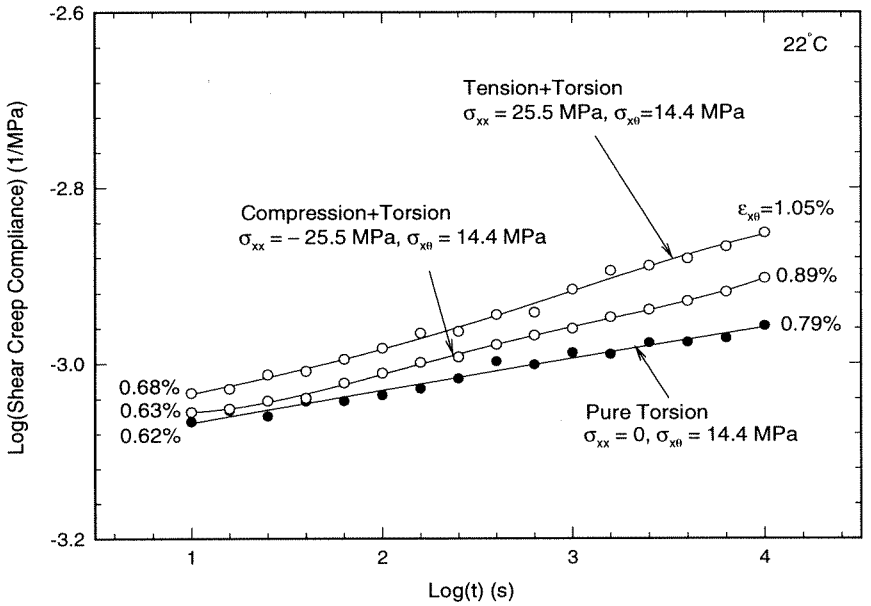

Figure 3.14: Shear creep compliance at $22°C$

response at axial stresses of $\sigma = \pm 25.5\ MPa$ with that under zero axial stress, we observe that a superposition of either a tensile stress ($\sigma = 25.5\ MPa$) or a compressive stress ($\sigma = -25.5\ MPa$) on a pure torsion increases the torsional (shear) creep rate. However, a superposed tensile stress tends to increase the rate distinctly more than does a compressive stress. This same phenomenon is observed at other temperatures. Figures 3.15, 3.16 and 3.17 show the shear creep compliances superposed with different axial stresses at $35°C$, $50°C$ and $80°C$.

Let us examine the results shown in figure 3.17 for $80°C$ more closely. A superposition of an axial compression of $-13.0\ MPa$ increases the shear creep compliance relative to that pure shear (torsion) of $9.4\ MPa$ by 8.2% at time $t = 10^4\ s$. On the other hand, a superposition of an axial tensile stress of $+13\ MPa$ increases the shear creep compliance much more, namely by 46.9% at the same time. When a compressive stress of $\sigma = -25.0\ MPa$ is superposed on shear, the creep rate is significantly increased and is even higher than that for a superposed tensile stress of

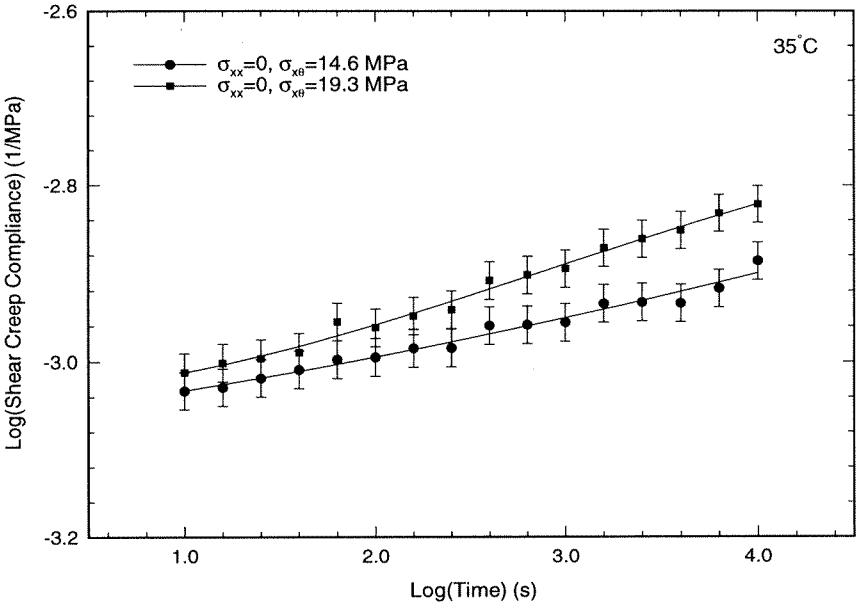

Figure 3.15: Shear creep compliance at $35°C$

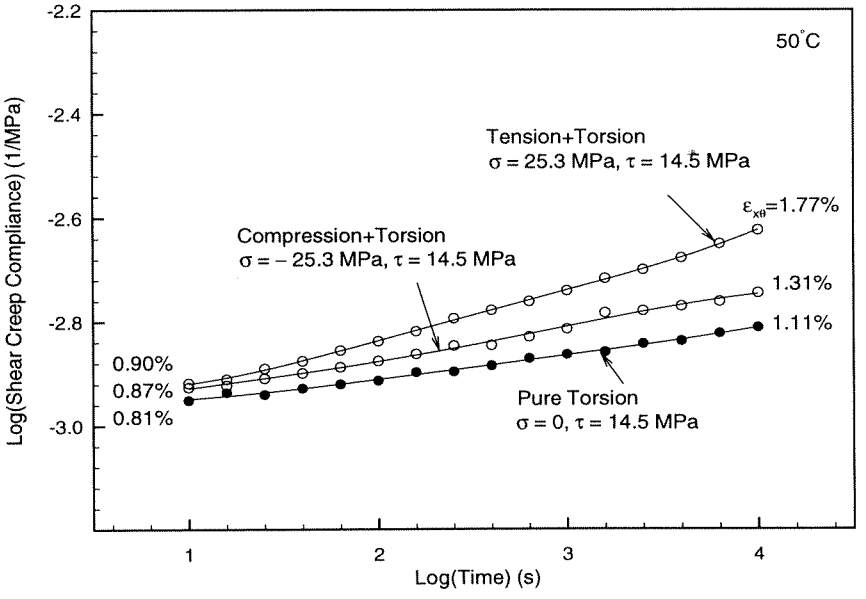

Figure 3.16: Shear creep compliance at $50°C$

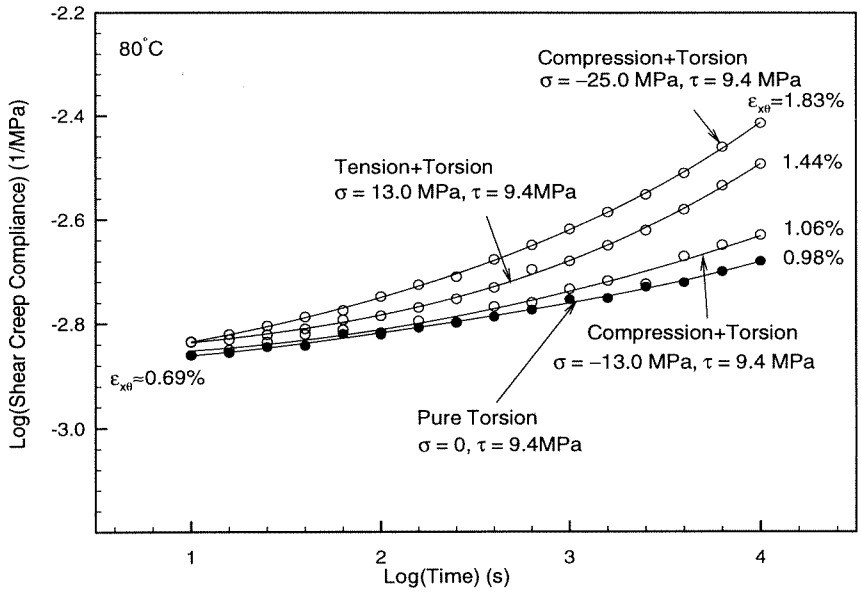

Figure 3.17: Shear creep compliance at 80°C

$\sigma = +13\ MPa$. The shear creep compliance is now 86.7% higher than that for pure torsion under zero axial load at $t = 10^4\ s$.

To provide a qualitative explanation to the behavior observed here, consider a pure shear ($\tau = 9.4\ MPa$) superposed by either a tensile stress ($\sigma = 13\ MPa$) or a compressive stress ($\sigma = -13\ MPa$). In both cases the resultant maximum shear stress and octahedral shear stress ($\sigma_s^{oct} = \frac{\sqrt{2}}{3}\sqrt{\sigma^2 + 3\tau^2}$) are the same but the isotropic stress components are different. If one thinks of a stress state with the maximum shear stress and zero hydrostatic stress as an intrinsic shear, one might expect that as the intrinsic shear stress (and the shear strain) increases the creep rate increases; this was observed for the pure torsion case. For this examples of the tensile and compressive stresses superposed on the pure torsion, the intrinsic shear is also the same, and thus the role of volumetric deformation starts to emerge. For the superposed tensile stress case, the isotropic stress is positive and the volumetric deformation (free volume variation) is positive; the creep rate is further accelerated with respect to the intrinsic shear

case. On the other hand, for the superposed compressive stress case, the volumetric deformation (free volume variation) is negative, which slows down the creep rate with respect to the intrinsic shear case, though the net creep rate is still higher than that for a pure torsion with zero axial load.

When a much higher compressive stress ($\sigma = -25.0\ MPa$, figure 3.17) is superposed on the pure torsion, the intrinsic (maximum) shear stress is 15.6 MPa, much higher than the intrinsic shear stress (11.4 MPa) for superposed axial stress of 13 MPa, it thus accelerates significantly shear creep rate. Despite the decrease in creep rate due to the negative isotropic stress, the net shear creep rate is still higher than the superposition of a smaller tensile stress (13 MPa).

Notice that although the shear creep compliances at temperatures between $22°C$ and $80°C$ are clos at short times, the difference of creep compliances at lower temperatures (from $22°C$ to $50°C$) are larger than that at $80°C$. These results are due to the strain range experienced at each temperature. At $80°C$, the material is closer to the glass transition temperature and becomes relatively soft. Thus a creep curve covers a relatively wider strain range than that at lower temperatures. The strain range covers most likely linear regime at the beginning and nonlinear regime as time evolves. In the linear regime the creep compliances are stress (or strain) independent and therefore exhibit coincidence appearance at different superposed axial stresses. However in the nonlinear regime the creep compliances start to deviate, as observed in figure 3.17. At lower temperatures ($22°C$, $35°C$), the material becomes more rigid than that at $80°C$ and the creep behavior is less pronounced. The strains experienced in the creep time may be all within the nonlinear regime and therefore exhibit deviation from the beginning for the chosen axial stress magnitude.

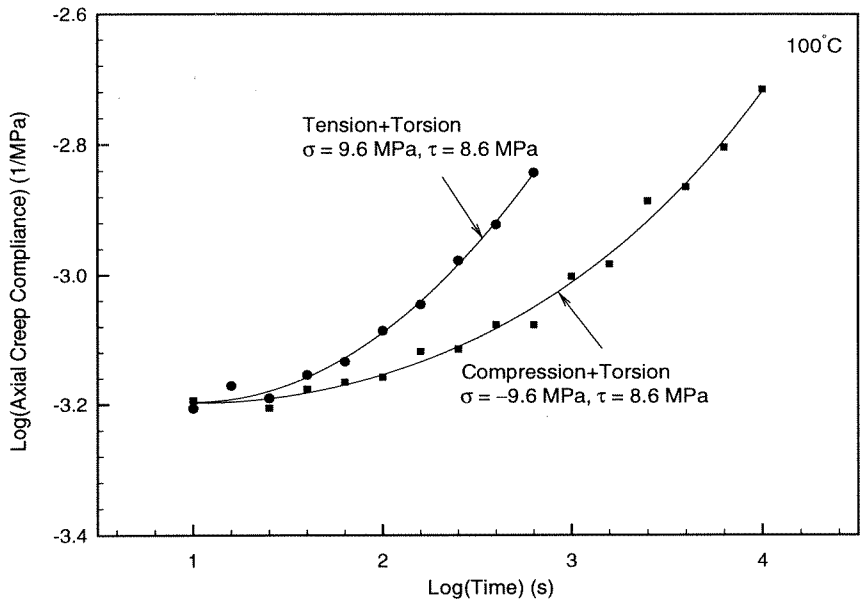

Figure 3.18: Axial creep compliance at $100°C$

3.4 Axial Creep Behavior

Consider next the axial creep behavior resulting from combined axial and torsional loading. Figures 3.18 and 3.19 show the axial creep compliances corresponding to the combined axial and torsional loading as shown in figures 3.12 and 3.13. For the same magnitude of axial and shear stresses, the axial creep compliance in combined tension and torsion is much higher than that for the combined compression and torsion. In both cases the maximum shear stress is the same, it is therefore the difference in isotropic stress that produces the difference in axial creep compliance. The combined tension and torsion leads to positive volume dilatation (and thus free volume dilatation) which provides a higher axial creep response rate than the combined compression and torsion (negative volumetric deformation).

The axial creep compliances for the combined axial and torsional loading below the glass transition (described in section 3.3.1) in figures 3.20 to 3.23. It can be seen from figure 3.20 that the axial creep compliance under combined tension and

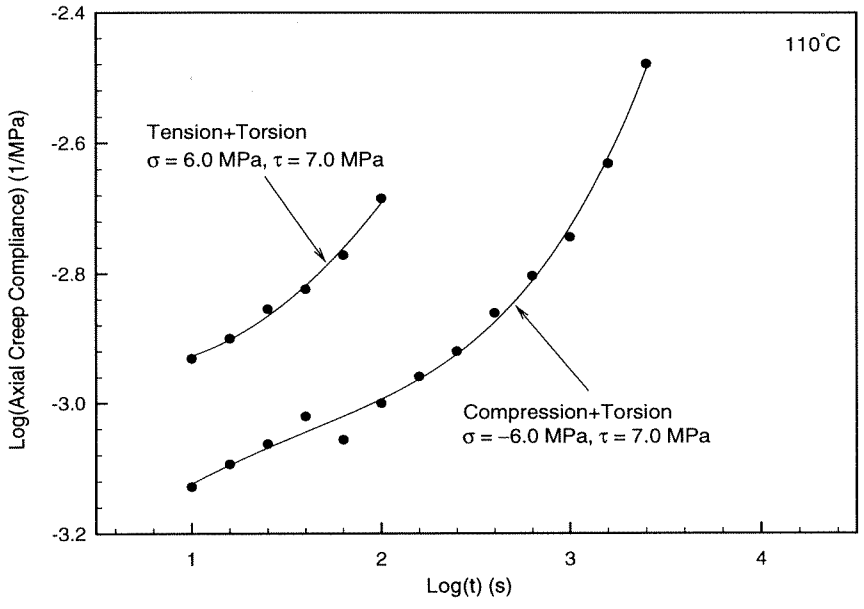

Figure 3.19: Axial creep compliance at 110°C

torsion loading is higher than that for a combined compression and torsion of the same magnitudes of stresses. In both loading conditions, the intrinsic shear stress (maximum shear stress) is the same, the difference is again in the isotropic stress. Free volume consideration suggests that a positive free volume variation increases the deformation rate while a negative volumetric deformation decreases it, and this conclusion is confirmed by these results.

Figure 3.23 shows the axial creep compliance for the combined axial and torsional creep tests at 80°C. The creep rate for the compression case is apparently smaller than that for tension case. This is also consistent with the prediction of free volume concept. However, the magnitude of the axial creep compliance for the combined compression and torsion case is larger than that for the combined tension and torsion case at the beginning. This is possibly due to uncertainties in measurement.

The results for the axial creep compliances under uniaxial creep and multiaxial creep at 35°C are presented in figure 3.24. It is observed that the axial creep com-

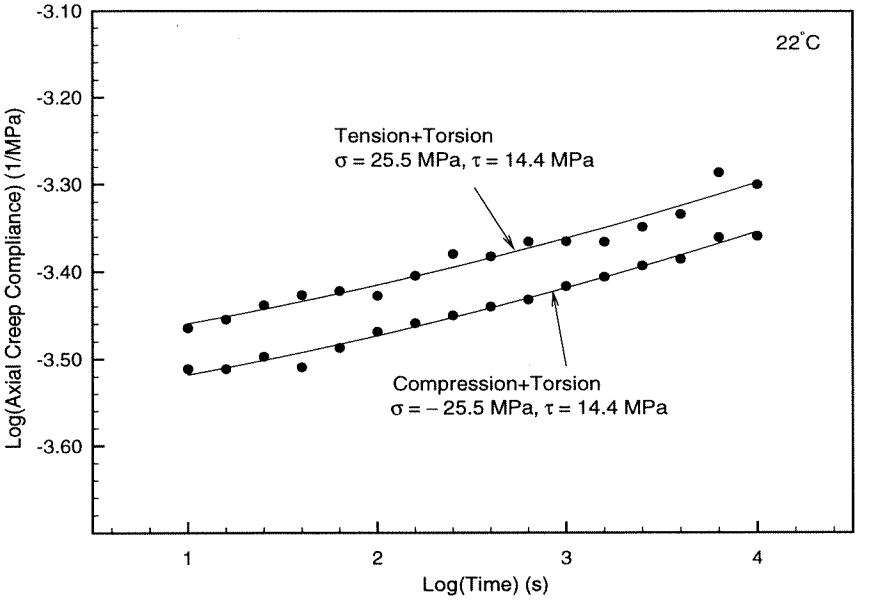

Figure 3.20: Axial creep compliance at $22°C$

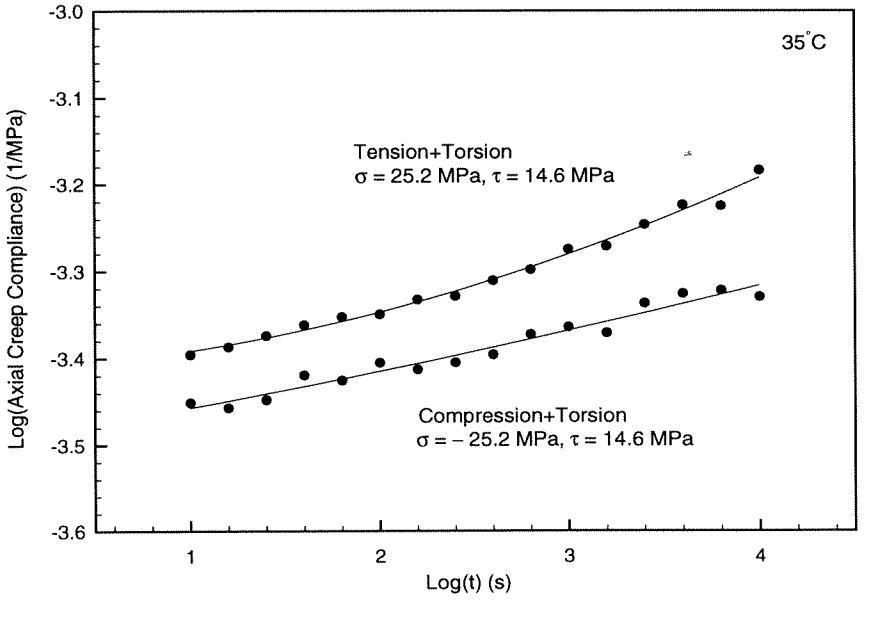

Figure 3.21: Axial creep compliance at $35°C$

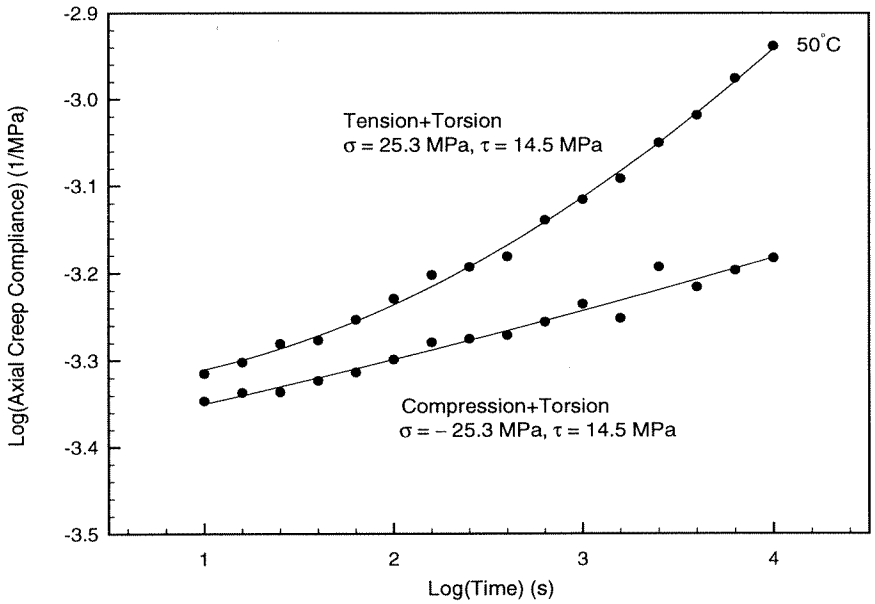

Figure 3.22: Axial creep compliance at $50°C$

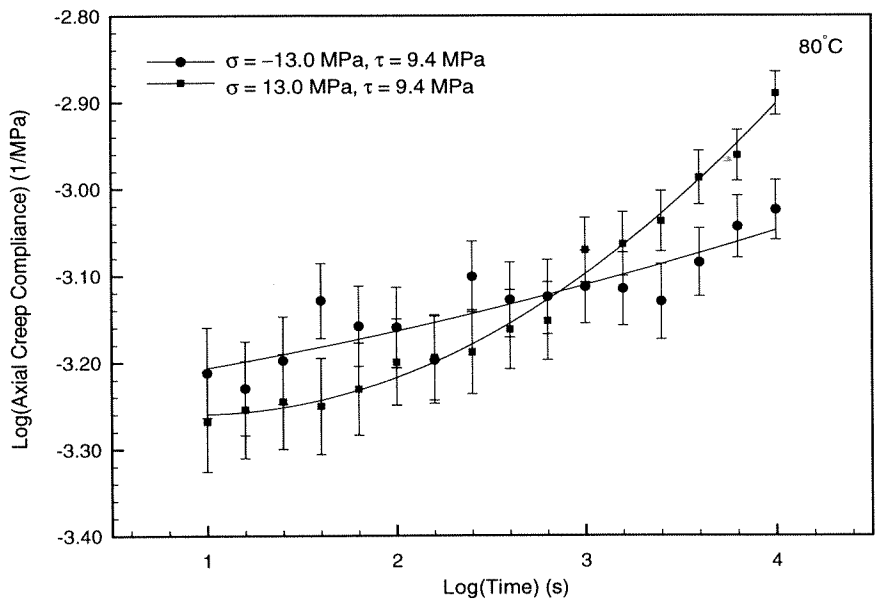

Figure 3.23: Axial creep compliance at $80°C$

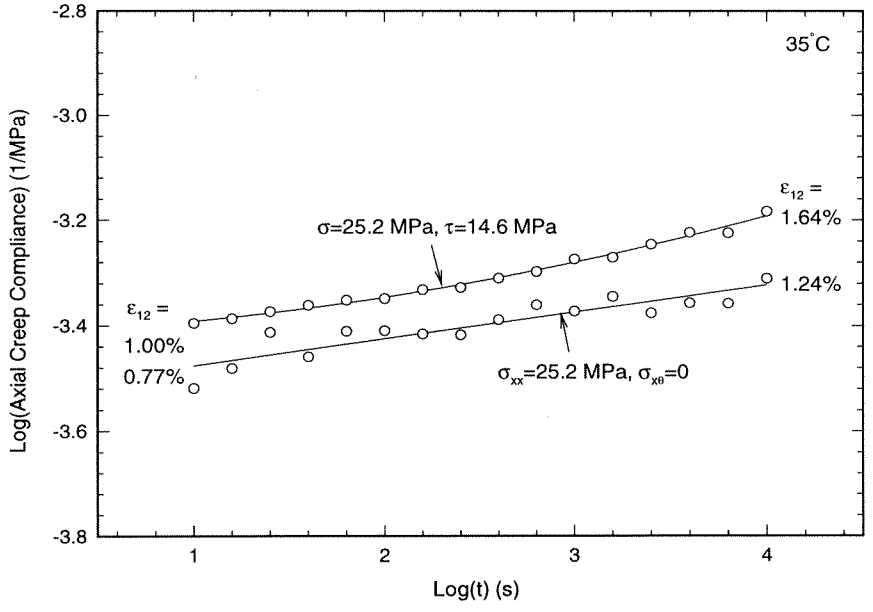

Figure 3.24: Axial Creep Compliance at $35°C$

pliance under multiaxial creep is higher than that under axial creep with an increase of 32% at $t = 10^4$ s. Since the difference in the two tests is the shear stress, we can identify that the shear stress accelerates the axial creep compliance. Although there is Poynting effect generated axial strain due to torsion, since it is on the order of the square of the applied shear strain, it is expected that it can induce only an axial strain variation of less than 0.05%. Therefore the significant amount of acceleration in axial strain cannot be explained by the Poynting effect, and it can be identified to be the influence of the applied shear stress.

3.5 Octahedral Behavior

In dislocation governed yield behavior plasticity theory can provide a unifying constitutive description in terms of octahedral stress and strain representations. It is thus natural to ask in the present context whether an octahedral description instead of a shear and normal stress/strain description similarly offers simplified or unified

material description. The answer is a clear "no", even though in the context of classical plasticity occtahedral stresses and strains are related through shear response and independently so of the dilatational stress and strain relation.

In casting the data into octahedral form we must incorporate an assumption regarding the deformations: While surface strains are measured directly, the strain through the wall thickness is not determined explicitly. In order to compute octahedral strains we assume thus that the radial strain is equal to the circumferential strain and related to the axial strain via a Poisson ratio. Following the analysis of Poisson's ratio in Lu, Zhang and Knauss (1997) we assume a value that depends on temperatures but not on time. The error in the present situation is minimal and insufficient to invalidate the conclusions reached here.

It is clear from figures 3.25 and 3.26 octahedral response is modified by the isotropic stress or stain component for temperatures at $100°C$ and $110°C$, which should be compared with figures 3.12 and 3.13 respresenting the same data as simple shear behavior. Similar results prevail for the comparison between octrahedral and simple shear response at all temperature (well) below the glass transition; for demonstration purposes it suffices to show in figure 3.27 one illustration of this behavior at $50°C$, which is the counterpart of figure 3.16. In summary, we conclude that respresentation of the (non-linear) creep behavior in terms of an octahedral representation neither eliminates nor reduces the effect of the dilatational stress or strain component(s) on the creep behavior. While the non-linearly time dependent behavior may ultimately be formulated in terms of an octahedral (shear) format, the second component in that formulation must be a first stress or strain invariant the magnitude of which modifies the time dependence (rate) of the deformations.

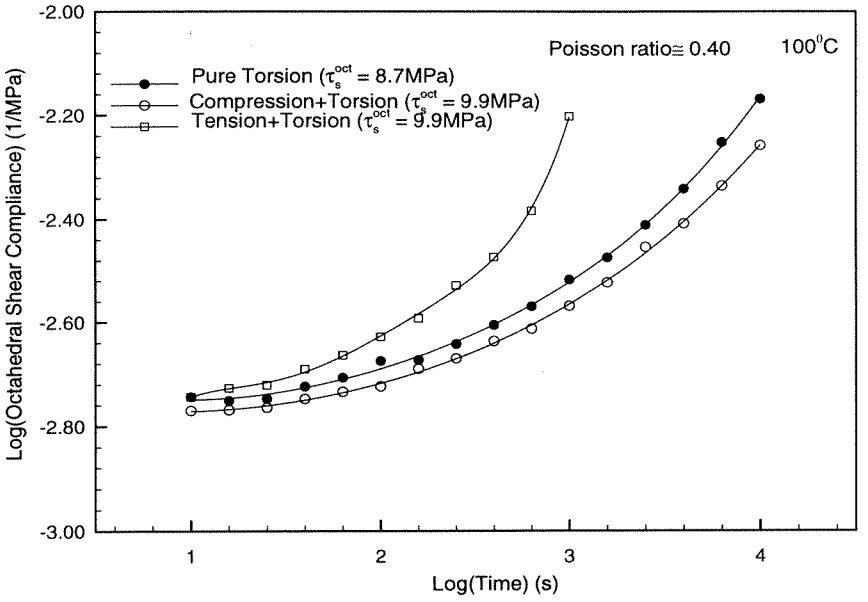

Figure 3.25: Octahedral creep compliance at $100°C$

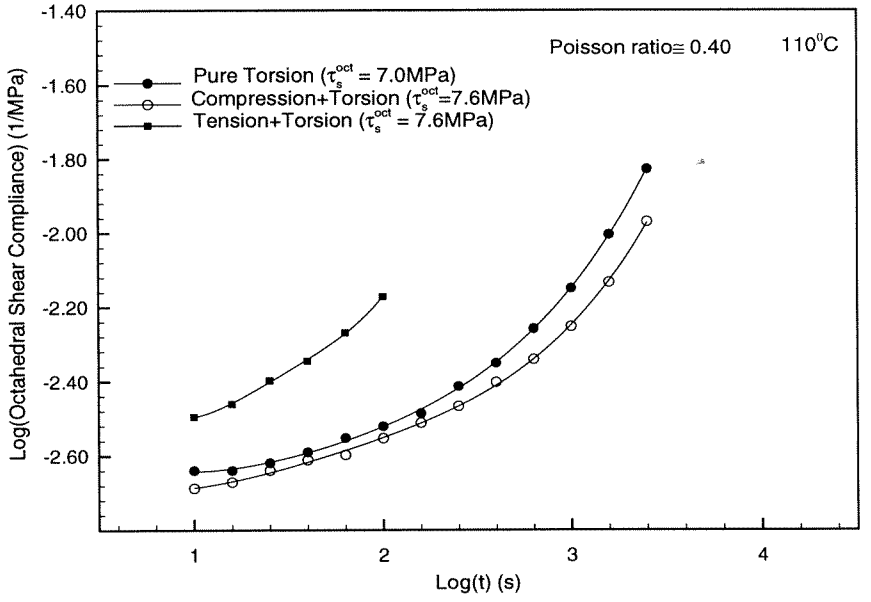

Figure 3.26: Octahedral creep compliance at $110°C$

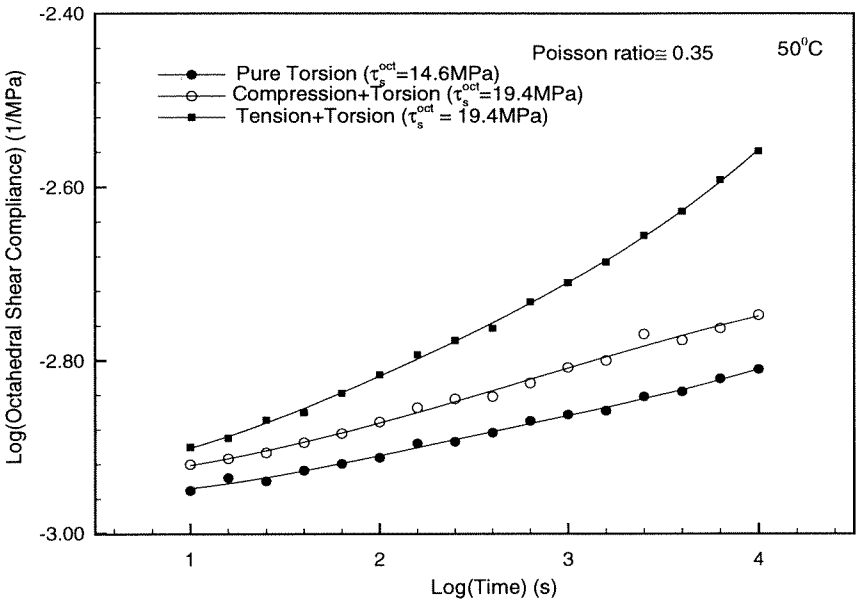

Figure 3.27: Octahedral creep compliance at $50°C$

3.5.1 Relation of Data to Model Representations

Formulations for non-linearly viscoelastic deformation behavior have been suggested by variouws authors (Bernstein, Kearsly and Zapas (BKZ), 1963; Schapery, 1969; Boyce, 1976; Knauss/Emri, 1981 and 1987; Losi/Knauss, 1992; Caruthers, 1986). While we shall not attempt to evaluate all these models against our measurements we examine the dilatational (free volume) model of Knauss/Emri/Losi and the strain clock moodel of Wineman/Waldron (1995), as well as the "stress clock" model advanced by Schapery, all of which have been used in recent stress analysis documentations. While it has been demonstrated earlier that free volume explanations controls (much of) the deformation response around the glass transition (Knauss/Emri, etc.) and of higher temperatures, the same is not true (substantially) below the glass transition. While either model renders qualitatively the behavior observed in tests, all fail to corraborate the data quantitatively; and only the volume clock model recognizes the distinct effect of dilatation on (shear) creep response.

Stress-Clock

We turn first to examining the stress-shift clock suggested by Schapery (1969), and note that in view of the complex shear-dilatational behavior outlined in section 3.3.1 it is hardly expected that a single stress-shift, whether by maximum shear stress, octahedral or principle value, will coordinate the data (quantitatively). We demonstrate this lack of corroboration via the $80°C$ (shear) data in figure 3.6 where it is clear that the creep curve segments do not possess (sufficient) portions of common slopes to allow completion of a simple "master curve". Following Schapery's suggestion that often the subtraction of a "glassy" compliance from the data leaves a transient (time-dependent) portion that plots with constant slope on a log-log plot, we have also attempted to extract a "glassy compliance" in the form of a monotonic function of the stress level from these data to a stress-shifting process. While the curvature of the creep segments changed with $\log(time)$, the net result was such that both slope and curvature were measurably different from the steep segments so as to preclude horizontal (and/or vertical) shifting[11].

Returning to measurements obtained at $80°C$ (figure 3.6) one observes that the (shear) creep compliance increases monotonically with the shear stress. The creep compliance inverted from the relaxation modulus is different from that measured at a shear stress of 9.4 MPa. Nonlinearity is thus apparent at a much lower shear stress level than

Turning to measurements obtained at $80°C$ (figure 3.6) one observes that the

[11]We also observe this phenomenon in Govaert's data (1995). Figure 3.28 shows this for Polycarbonate at $20°C$ under multiaxial tensile stresses. At axial stresses of 15 MPa and 20 MPa, the creep data are initially very close but deviate as time increases, so that the shifting (either horizontally or vertically, or both) is not appropriate. Shifting at higher stress levels appears more reasonable for these curves which are, however, measured over only 2 decades in time. It is typically more subjective to shift data obtained for short periods of time, i.e., the master curves might be significantly different if segments are shifted by different persons. Figure 3.29 shows the creep master curve shifted by Govaert (1995) and by present authors. The latter is effected so as to obtain overlapping of the short time portion of the segments while the shifting by Govaert is conducted possibly to ensure a global least square fit to the measured data. One notes differences of more than 1.5 decades of time at $t = 10^5$ s and more than 3 decades of time difference at $t = 10^{10}$ s.

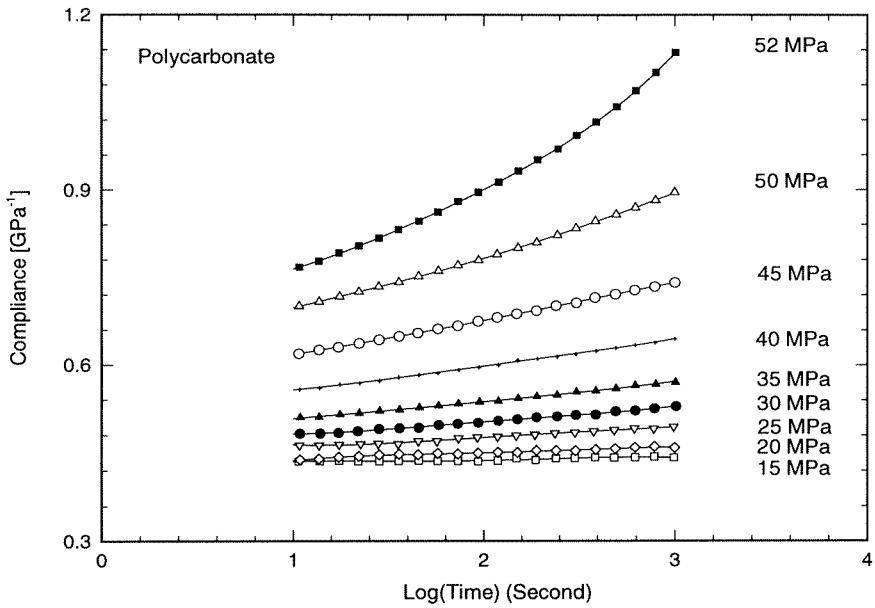

Figure 3.28: Axial creep compliance at different stresses ($20°C$)

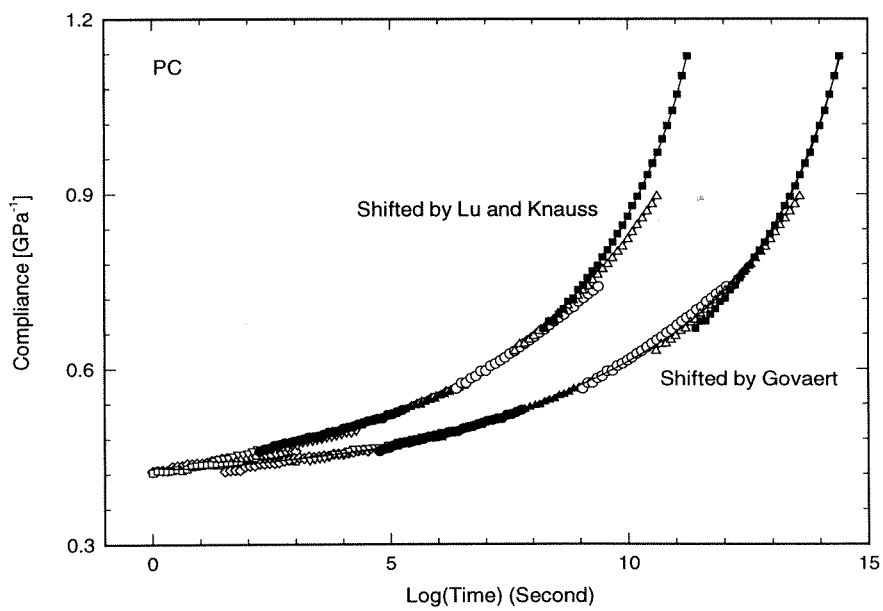

Figure 3.29: Axial creep compliance master curves ($20°C$), left curve: shifted by authors; right curve: shifted by Govaert

(shear) creep compliance increases monotonically with the shear stress. The creep compliance inverted from the relaxation modulus is different from that measured at a shear stress of 9.3 MPa. Nonlinearity is thus apparent at a much lower shear stress level than at $22°C$. The creep compliance inverted from the relaxation modulus and those at shear stresses of 9.3 MPa and 12.3 MPa are essentially the same again at the beginning (short time) but deviate gradually as time increases, thus repeating the phenomenon observed at $22°C$ and $35°C$. These consistent observations indicate that in the initial stage when the shear strains are small ($< 1\%$) the linearity range has not been exceeded significantly and therefore the material behaves as a (nearly) linearly viscoelastic solid. However, as the shear strain increases the nonlinearity effect becomes more pronounced and as a consequence the shear creep compliance deviates from the linear function. In this sense the nonlinearity is controlled by the magnitude of the shear strain.

Segments derived from creep compliances at different shear stress levels at $80°C$ were also shifted horizontally as shown in figure 3.30 as well as analyzed by "glassy" behavior. The result is not smooth compared to the relaxation modulus master curve measured at infinitesimal deformation (figure 2.15) inasmuch as creep curves at different shear stress levels cross each other. At these short time intervals when the long term direction is not determined, the shifting may appear fair, but the curves do not have common slopes.

The creep data (figure 3.7) at different shear stress levels at $100°C$ are shifted horizontally and a master curve is obtained as shown in figure 3.31. The master curve is much smoother than that at lower temperatures ($22°C$, $35°C$ and $80°C$). This suggests that the time-stress superposition can be applicable near the glass transition, but not not necessarily for certain stress levels well below the glass transition.

At $100°C$ when the temperature is close to the glass transition, the Poisson's ratio is close to 0.5. As the dilatation variation is small over the test period of 10^4 s, it

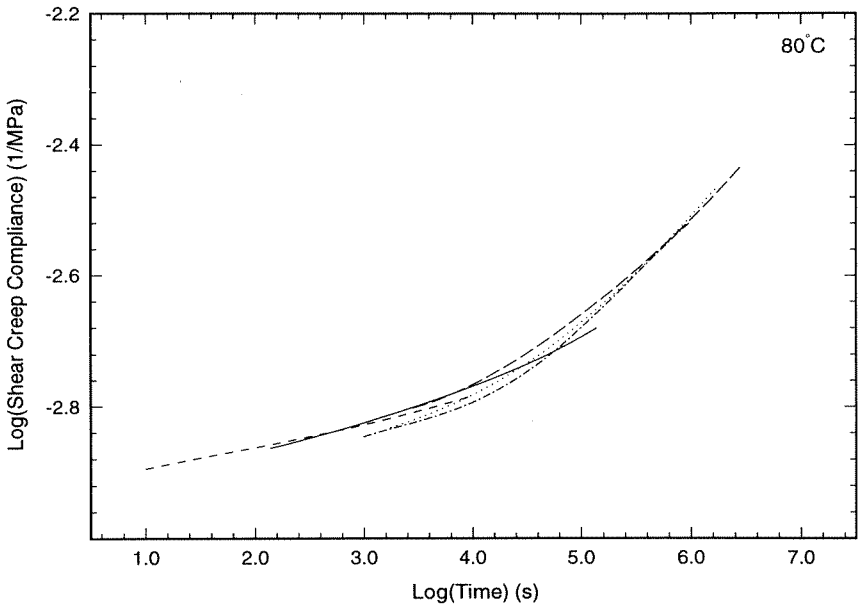

Figure 3.30: Shear creep compliance at 80°C

may be close to a constant. The shifting of creep data in terms of stress might be essentially the same as the shifting in terms of the strain induced dilatation. This seems to indicate that stress-shifting might be valid near the glass transition not deep in the glassy state.

Nonlinearly Constitutive Relations

The constitutive models proposed by Emri and Knauss (1981) and Losi and Knauss (1992) are modified to accomodate the instantaneous local free volume change due to shear. The basic equations are listed in this section[12]. For an isotropic, simple material with memory the constitutive relation under an isothermal process is described by

$$S_{ij}(t) = \int_{-\infty}^{t} 2\mu(\xi(t) - \xi(\tau)) \frac{\partial e_{ij}(\tau)}{\partial \tau} d\tau, \tag{3.5}$$

$$\sigma_{kk} = \int_{-\infty}^{t} K(\xi(t) - \xi(\tau)) \frac{\partial \epsilon_{kk}}{\partial \tau} d\tau, \tag{3.6}$$

[12]For a detailed development of the free volume based model, see Emri and Knauss, 1981; Losi and Knauss, 1992 and Lu and Knauss, 1996.

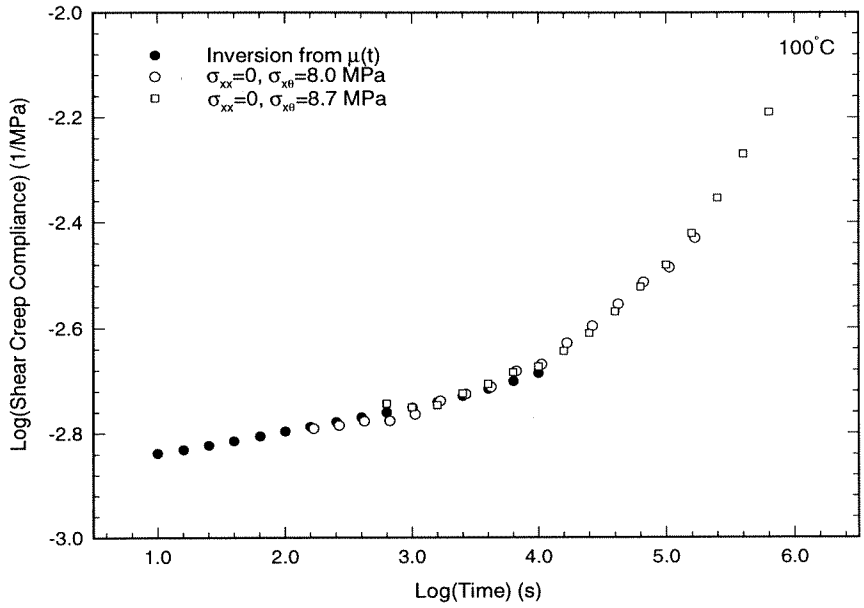

Figure 3.31: Shear creep compliance shifted from different stress levels at $100°C$

where σ_{ij}, ϵ_{ij} are stress and strain components, S_{ij} and e_{ij} are deviatoric stress and strain components, $K(t)$ and $\mu(t)$ are the bulk and shear relaxation functions, and ξ is the internal time determined by

$$\xi(t) = \int_0^t \frac{d\tau}{a_T}, \tag{3.7}$$

where a_T is the time shift factor determined by

$$\log a_T = B(\frac{1}{f} - \frac{1}{f_0}), \tag{3.8}$$

where B is a material parameter, f is the effective fractional free volume and f_0 is its value in the reference state.

$$f = f_e + \alpha\epsilon_{kk} + \beta\frac{\epsilon_s^{oct}\cos(\theta_0 + \epsilon_s^{oct})}{\sin\theta_0}. \tag{3.9}$$

$$f_e = \frac{f_\infty}{1 - \frac{A}{2} e^{B(\frac{1}{f_e} - \frac{1}{f_0})}}. \tag{3.10}$$

A is a stochastic parameter.

$$f_\infty = \begin{cases} f_0 + \alpha_g (T - T_g) & \text{for} \quad T \leq T_g \\ f_0 + \alpha_f (T - T_g) & \text{for} \quad T > T_g \end{cases} \tag{3.11}$$

where α_g and α_f are the coefficients of thermal expansion in the glassy and rubbery states respectively, T is the temperature and T_g is the glass transition temperature.

Model Parameters

It is found that with a pair of parameters ($\alpha = 1.0, \beta = 1.0$) all the behavior observed may be explained qualitatively. However, to best fit the data under various loading conditions, the following parameters may be appropriate.

$$\begin{aligned} A &= 0.2 \\ f_0 &= 0.036 \\ B &= 0.4342 \\ \alpha_g &= 2.5 \times 10^{-4}\ C^{-1} \\ \alpha_l &= 9.47 \times 10^{-4}\ C^{-1} \end{aligned}$$

.Below T_g, $\alpha = 0.3$

$\beta = 0.6$

Above T_g, $\alpha = 1.0$

$\beta = 0.25.$

Comparison of model prediction and measurements

Figure 3.32 shows the comparison of the model prediction and measurements. The

model predicts the relative creep rates at different stress levels. At the lower shear stress level ($\tau = 9.4MPa$), the agreement is good. At higher shear stress levels, the model reproduces the features only qualitatively, however, the curvature of the model prediction is different from that of the measurement. There are two possible reasons for this discrepancy: (i) The model prediction is very sensitive to dilatation, which is computed from the measured axial strain, shear strain and circumferential strain. While the axial and shear strains are measured with an error of $\pm 0.05\%$ of strain, the error in measuring the circumferential strain is larger and on the order of 0.08%. Therefore, the measured circumferential strain is not used to compute the volumetric deformation; instead, the circumferential strain is computed from the axial strain via Poisson's ratio $\nu(t)$ (Lu, Zhang and Knauss, 1996) that is measured from infinitesimal deformation and so that the circumferential strain $\epsilon_{\theta\theta}$ is (quasi-elastically) related to the axial strain ϵ_{xx} through

$$\epsilon_{\theta\theta} = -\nu(t)\epsilon_{xx}. \tag{3.12}$$

In the case of larger axial strain, the relation between circumferential and axial strains may not obey this relation that is valid for infinitesimal deformation. It might then be appropriate to shift the Poisson's ratio logarithmically to larger strains because the dilatation accelerates the internal time. This requires either data on the ratio of circumferential strain to axial strain at higher strain levels or accurate data on Poisson's ratio at different temperatures, neither of which are available at this time. The determination of the actual shear induced dilation is important in this model, we have proposed an analog model to demonstrate the shear induced dilatation, the actual shear induced dilatation requires the distribution (spectrum) of initial orientation angles θ_0 and the parameter, which should be determined from direct measurement of the shear induced dilatation. In the case that a specific angle θ_0 is used as an average, may explain qualitatively but might not be able to explain

quantitatively the behavior over a wide range of temperature and stress levels.

It is noted that after $t = 10^3\ s$, the model predicted shear creep compliances increase very fast at higher shear stress levels. This is so because the effective fractional free volume has reached the level of the value in the glass transition and the internal time has reached the rubbery regime. It is expected this might change when the two problems listed above can be resolved.

Figure 3.33 shows the comparison of results between the model prediction and measurements. The model can predict qualitatively the relative position of one curve relative to others. The quantitative agreement is good for the pure torsion ($\sigma = 0,\ \tau = 9.4\ MPa$) and pure torsion superposed by a smaller compression ($\sigma = -13.0,\ \tau = 9.4\ MPa$). However, the predicted creep rates are smaller than those measured at short times. At longer times because the effective fractional free volume reaches the value of the glass transition region, the predicted creep compliance should take the value in the glass transition. Since the creep compliance increases very fast in the glass transition region, this leads to a very faster creep compliance than measurements. With an accurate determination of the volumetric strains, one may expect a slower increase in creep compliance that is closer to measured data.

Figure 3.35 shows the comparison of shear creep compliances between model prediction and measurement. The shear creep compliance under pure torsion with zero axial load predicted from the model and that measured from the experiment has a very good agreement. Under a superposed tension, the model predicts a faster shear creep rate, and, under a superposed compression, the model predicts a slower shear creep rate. The model predicts qualitatively the right feature as experimental observation. When there is superposed tension, there is a positive effective fractional free volume variation, the internal time goes into the rubbery regime and therefore induces a much faster shear creep rate. On the other hand, when there is a compression superposed on pure torsion, there is a negative effective fractional free volume

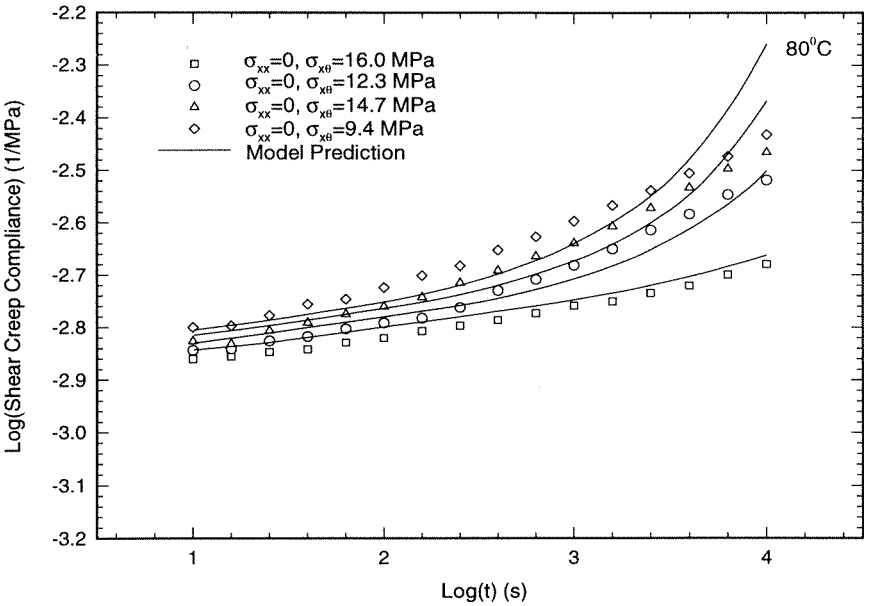

Figure 3.32: Comparison of model prediction and measurements for shear creep Compliance at $80°C$

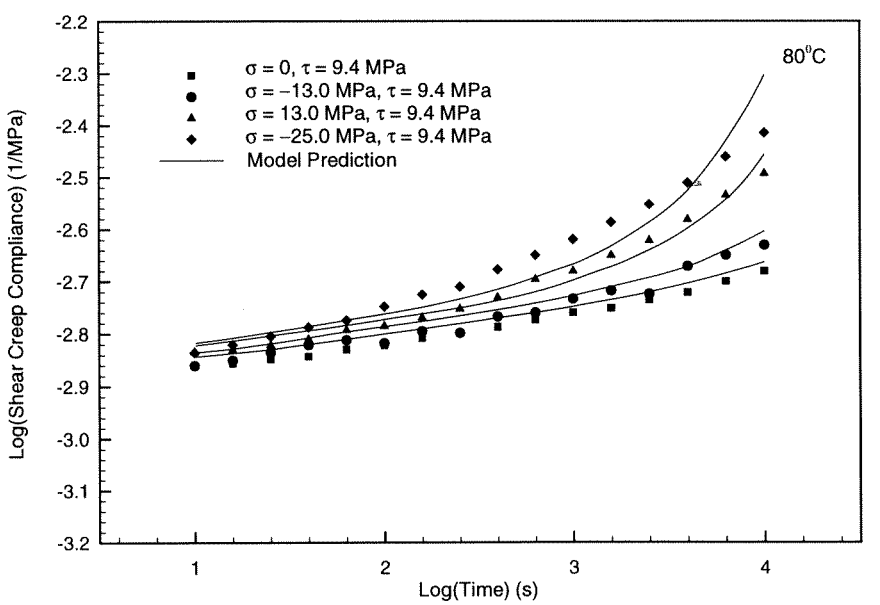

Figure 3.33: Comparison of model prediction and measurements for shear creep Compliance at $80°C$ under multiaxial loading

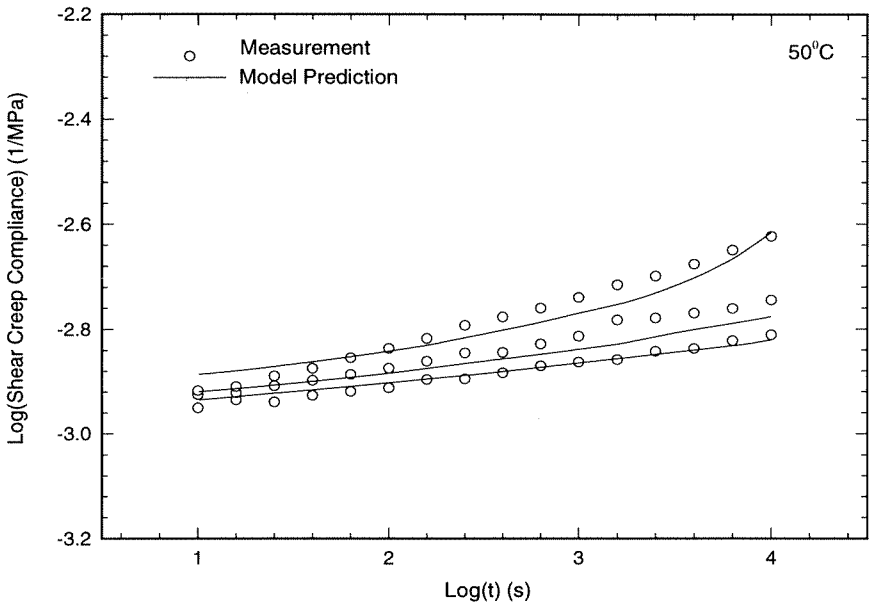

Figure 3.34: Comparison of model prediction and measurements at $50°C$

variation and the internal time goes into the glassy state, and therefore induces a slow rate. Since the shear creep compliance does not vary over time significantly in the glassy state, the shear creep compliance decreases only slightly under compression.

The discrepancy between model prediction and measurements at $110°C$ might arise from two facts: (i) The internal material governing time is very sensitive to the volumetric deformations. For this experiment, the axial and shear strains can be determined to an accuracy of $\pm 0.05\%$, respectively, however, an accurate determination of the circumferential strain is not possible. As an approximation, an elastic response between the circumferential strain and axial strain is assumed and the circumferential strain is computed from the axial strain via Poisson's ratio (Lu, Zhang and Knauss, 1996). This might lead to some extent of error when the circumferential strain determined in this way is not accurate.(ii) The shear creep compliance under infinitesimal deformation ($\mu(t)$) measured at temperatures between $105°C$ and $120°C$ is not accurate because the torque reading is not accurate when the torque is not big

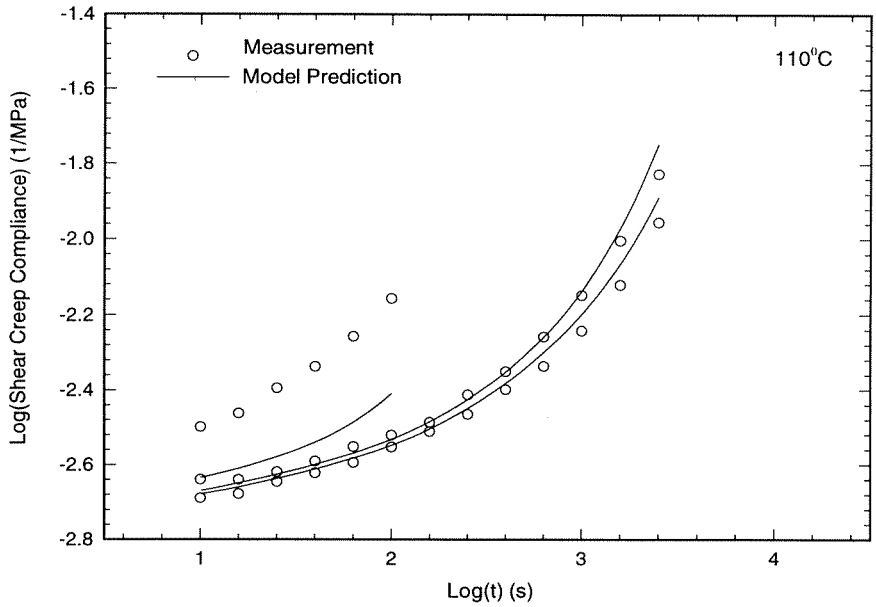

Figure 3.35: Comparison of model prediction and measurements for shear creep compliance at $110°C$

compared with the accuracy of the MTS system (0.084 Nm).

If the circumferential strain measurement is not accurate, a question arises: to what accuracy a measurement should be made in order to predict the behavior under combined tension and torsion?

3.6 Summary

This study intends to investigate the the effects of volumetric and deviatoric deformations on the nonlinearly viscoelastic behavior at creep strains up to 6%. To this end a sequence of creep tests were performed under combined axial (tension, compression) and torsional loading at temperatures between room temperature and $110°C$ with PMMA thin walled cylindrical specimens. A constitutive model based on free volume consideration was proposed to model the multiaxial behavior. The following conclusions can be made:

(i) A strong coupling between axial and shear strains at strains as small as 1% at different temperatures is observed. This observation indicates that the linear viscoelasticity is not valid for strains higher than about 1% for certain categories of polymers. A nonlinear characterization of the behavior of polymers under multiaxial loading is needed for strains not less than 1%.

(ii) Well below the glass transition temperature wither a superposed tensile stress or a compressive stress increases the torsional creep rate, with a tensile stress providing distinctly more creep acceleration than a compressive stress. However, in the vicinity of the glass transition, a superposed compressive stress decreases the torsional creep rate while a tensile stress increases it. These observations indicate that both volumetric deformation (free volume) and deviatoric deformation contribute to the nonlinearly viscoelastic behavior of polymers. However, the effect relative contribution of any volumetric vis-a-vis shear effects in controlling general deformation rates varies with temperature and is particularly sensitive to how close the temperature is close to the glass transition.

(iii) The effect of shear to the viscoelastic behavior is incorporated through the shear induced dilatation and the concept of effective free volume is introduced to include the shear induced dilatation. A constitutive model that is based on free volume consideration is proposed to explain the behavior observed in the experiment. This model can qualitatively explain the acceleration and deceleration of deformation rate under various multiaxial loading. The relative deformation rates under various loading conditions can be explained qualitatively within the framework of free volume consideration. Quantitative agreement is good for time-temperature superposition, creep behavior under pure torsion loading at relatively small shear stress and multiaxial creep behavior near the glass transition. However, the model prediction cannot fit the creep data very well under multiaxial loading at tempertures well below the glass transition.

3.7 Appendix: Nonlinearly Viscoelastic Constitutive Relation for Amorphous Polymers

3.7.1 Introduction

The constitutive models proposed by Emri and Knauss (1981) and Losi and Knauss (1992) are modified here to accomodate the instantaneous local free volume change due to shear. Based on free volume consideration, a nonlinear constitutive model was proposed by Knauss and Emri (1981, 1987) to describe the time dependent behavior near the glass transition and another model that generalizes Knauss and Emri's description to glassy state was proposed by Knauss and Losi (1992) to describe the behavior both in the glassy and rubbery states. These models can explain a variety of phenomena in nonlinear range, including the effects of moisture content and pressure, relaxation behavior at different non-infinitesimal strain levels, uniaxial straining with piecewise constant deformation rates, uniaxial stress-strain behavior superposed in pressure, etc.

A point that has been made is that if volumetric changes are solely responsible for the "yield-like" behavior in polymers, then "yielding" should not occur in these materials if pure shear deformations, such as under torsion, prevail. This latter assumption is based on our normal understanding of metal yielding, but is not necessarily justified for polymers. Indeed, that dilatational straining can result from shear is both conceivable and measurable. In fact, Robertson (1963, 1966, 1968, Robertson & Patel, 1972) argued that volumetric changes should accompany with shear stressing as a result of molecular chain stiffness and suggested that shear-yielding would then result from the dilatationally induced increase in molecular mobility. However, a direct measurement of the associated dilatation was not attempted. On the other hand, McKenna and coworkers (McKenna & Zapas, 1979; Duran & McKenna, 1990) have recorded volume changes under purely torsional deformations. Similarly, we have

observed axial deformation under purely torsional creep under zero axial loading (Lu and Knauss, 1996), though the resolution limitation of the digital image correlation prevents to provide the volumetric changes.

We present an analog model here to demonstrate that local shear deformation may induce instantaneous local dilatation which allows the surrounding molecules to take this position, and this process occurs in sequence to give rise to local volume needed for molecules to move. Although the overall deformation may not change significantly, the local shear induced dilatation is significant and may tremendously accelerate the deformation rate. We therefore introduce the concept of effective free volume that includes the volumetric deformation from different sources, including volumetric deformation due to the isotropic deformations, such as moisture content, temperature and hydrostatic pressure, and the local instantaneous dilatation due to deviatoric deformation. The dependence of internal time on the shear deformation is therefore included through the local effective volumetric deformation.

A similar approach was proposed by Wineman and Waldron (1995), where he introduced the dependence of a material clock or pseudo time on a scalar function that is equivalent to a shift factor, and this scalar function depends not only on the volumetric deformation but also on the local shear. The definition of local shear depends on the deformation considered. The local shear was introduced to contribute the deformation rate without any physics explanation.

The effective free volume we introduce here is still in the framework of free volume consideration. In the regime of linear viscoelasticity, when a cylinder is subjected to a pure torsion with a fixed end distance, the volumetric deformation generated from torsion is on the order of the square of the shear strain, which is usually considered to be negligible for infinitesimal deformation. However, in the regime of nonlinearly viscoelasticity, the volumetric deformation may be higher, as observed by McKenna. Since the volumetric deformation determined from the trace of the infinitesimal strain

tensor contains only the volumetric deformation from the isotropic stress, the volumetric deformation due to deviatoric deformation is therefore neglected. The inclusion of the volumetric deformation due to the deviatoric part is thus necessary to take into account the volumetric deformation due to all possible sources.

Volumetric deformation may be generated from pure shear deformation in polymers. It may be determined (with some unknown constant to be determined from experiment) from a kinematic analysis based on large deformation description (Murnaghan, 1951) or an analysis based on small deformation and nonlinear constitutive relation (Poynting, 1912). But the shear induced dilatation in our consideration is a material behavior, which cannot be determined from kinematic analysis. It can only be determined from measurements. McKenna measured the dependence of volumetric deformation on shear deformation from a cylindrical specimen for an epoxide monomer. The volumetric deformation contains most likely linear term of the shear strain and higher order terms. Although this result depends on the geometry of the specimen and test conditions, the dilatation observed in the experiment is apparently contrary to the prediction of the Poynting effect for the test condition, because the Poynting effect predicts a volumetric contraction due to negative normal stress when the length of the cylinder specimen is fixed under pure torsion. This appears to indicate that there exists a volumetric deformation associated with the shear deformation.

With the extension of the free volume concept to effective free volume, we can therefore extend the framework of Knauss and Emri (1981, 1987) and Losi and Knauss (1992) accordingly. The extension of Knauss and Emri's model to effective free volume leads to a constitutive relation that is valid above the glass transition. On the other hand the extension of Losi and Knauss' description leads to a more general constitutive relation that may be applied to both glassy and rubbery states.

3.7.2 Nonlinearly Constitutive Model for Amorphous Polymers

For an isotropic, simple material with memory the constitutive relation under an isothermal process is described by

$$S_{ij}(t) = \int_{-\infty}^{t} 2\mu(\xi(t) - \xi(\tau))\frac{\partial e_{ij}(\tau)}{\partial \tau}d\tau \tag{3.13}$$

$$\sigma_{kk} = \int_{-\infty}^{t} K(\xi(t) - \xi(\tau))\frac{\partial \epsilon_{kk}}{\partial \tau}d\tau, \tag{3.14}$$

where σ_{ij}, ϵ_{ij} are stress and strain components, S_{ij} and e_{ij} are deviatoric stress and strain components, $K(t)$ and $\mu(t)$ are the bulk and shear relaxation moduli measured at a reference temperature, and ξ is the internal time given by

Time shift behavior in the nonlinear range

When the deformation is not infinitesimal such that the material exhibits nonlinear behavior, experimental observations have indicated that the time shift factor for polymers depends not only on the thermal history, but also on the mechanical induced volumetric deformation (Knauss and Emri, 1981, 1987). In the case that there are only isotropic deformations such as deformations induced by moisture content, temperature and hydrostatic deformation (in the absence of deviatoric deformation). The time shift factor is still given by equation (3.8), however, the fractional free volume which is a fraction of the total volumetric deformation, may be represented through an equation as proposed by Ferry and Stratton (1960).

$$f = f_0 + \alpha_f \Delta T + \beta_f \Delta\sigma_{kk} + \gamma_f \Delta c, \tag{3.15}$$

where α_f, β_f and γ_f are material parameters, ΔT, $\Delta\epsilon_{kk}$ and Δc are temperature, isotropic stress and solvent concentration changes with respect to the reference condition at f_0 (or H_0).

We now choose a reference state that is stress free under isothermal condition. The temperature and fractional free volume at this reference state are T_0 and f_0, respectively. With the introduction of the metastable free volume in section 3.7.2, The first two terms $(f_0 + \alpha_f \Delta T)$ on the right-hand side in Eq. (3.15), designating the fractional free volume at a reference state and that due to temperature effect, may now be replaced by a more general quantity, f_e (metastable fractional free volume), to account for the fractional free volume at any temperatures. Thus Eq. (3.15) can be written as

$$f = f_e + \beta_f \Delta\sigma_{kk} + \gamma_f \Delta. \tag{3.16}$$

Knauss and Emri (1981, 1987) considered a more general material model for which the material parameters (α_f, β_f, γ_f) are time-operators in the case that the Eq. (3.15) needs to be expressed in terms of convolution integrals over time histories of temperature, isotropic stress and solvent concentration. As an example, in the case of moisture concentration change only, the convolution integral would be

$$f(t) = f_e + \int_{-\infty}^{t} \gamma_f(\xi(t) - \xi(\tau)) \frac{\partial c}{\partial \tau} d\tau. \tag{3.17}$$

We focus our consideration on the contribution to free volume from the mechanical stress induced dilation with the material having the same moisture content as that in the reference state, the contribution from moisture content variation is therefore absent. We thus do not need to consider the contribution from moisture content in the subsequent consideration.

Effective Fractional Free Volume

Experimental results on the multiaxial behavior of polymers (Lu and Knauss, 1996) have demonstrated that shear can also accelerate viscoelastic deformation rate.

It is usually understood that there is no dilatation associated with the shear deformation in homogeneous polymeric materials. Experimental results, however, appear to indicate that there is a dilatation generated when there is a shear deformation in the nonlinear range. McKenna (1990) observed that when a polymer cylinder specimen is subjected to pure torsion with fixed end distance, there is a volumetric deformation generated. At small shear strain in lower temperatures the volumetric dilatation is approaching γ^2. However at higher strain or higher temperature, the volumetric deformation should include a linear term in γ. This observation is different from that as observed in steel wires by Poynting (1912). Poynting determined that when a steel wire under torsion with a free end, the wire may extend, the diameter may shrink and the total volumetric deformation may increase. It is therefore expected that when the wire is subjected to torsion with a fixed end distance, since the fixed ends prevent the elongation of the wire, there must be compressive force generated and this should induce a diameter increase due to Poisson effect and make the total volume decrease, which is different from the volume increase in polymers as observed by McKenna.

We consider an analog model as shown in figure 3.11. The interaction of a molecule chain from the surrounding molecules may be modeled by a "Z" shaped molecule embedded in a viscoelastic medium. When this molecule is subjected to a pair of shear forces, F, and starts to move, it has to overcome the interactions from the surrounding medium and create a local volume in its surrounding medium. This volume is on the same order of the shear strain, it may exist instantaneously and then disappear. But it creates a temporary volume (possibly a volumetric deformation relaxed over time) for the surrounding molecules and allows the surrounding molecules to take this position and move more easily. This instantaneous volume is expected to be observed by experimental investigations, such as McKenna's (1990) investigation. It certainly needs more thorough investigation to confirm this shear induced volumetric dilatation.

We now consider the magnitude of the shear induced local dilatation. Let ϵ be the axial strain in the vertical direction, γ be the local shear deformation. When a molecule initially at an orientation angle θ_0 moves to θ, the local shear strain is given by

$$\gamma = \frac{1}{2}(\theta - \theta_0).$$

In order to allow this shear strain to proceed, there must be a local shear induced axial strain, which is given by

$$\begin{aligned} \epsilon &= \frac{R(\sin\theta - \sin\theta_0)}{R\sin\theta_0} \\ &= \frac{2\cos(\theta_0+\gamma)\sin\gamma}{\sin\theta_0}, \end{aligned} \tag{3.18}$$

where $2R$ is the length of the molecule trapped between the upper and lower media.

This formulation is based on a two dimensional consideration. For a more general three dimensional case, the local shear, γ, may be replaced by the octahedral shear strain γ_{oct}, then Eq. (3.18) becomes

$$\epsilon = \frac{2\cos(\theta_0+\gamma_{oct})\sin\gamma_{oct}}{\sin\theta_0}. \tag{3.19}$$

The local shear induced dilation ϵ_{kk}^{oct} is assumed to be proportional to the shear induced axial strain, ϵ, i.e.,

$$\epsilon_{kk}^{oct} = \beta' \frac{2\cos(\theta_0+\gamma_{oct})\sin\gamma_{oct}}{\sin\theta_0}, \tag{3.20}$$

where β' is a parameter. The molecule chains in a polymer may take any orientation angles θ_0. We consider here an average behavior of molecules in different initial orientation angles and represent it by a parameter θ_0. For small deformation, the

molecule chains may easily move forward and backward near $\theta = \pi/2$. We therefore chose a θ_0 that is close to $\pi/2$ for our modeling of the constitutive behavior at strains on the order of a few percent.

In the previous consideration we consider only the mechanical induced free volume derived from isotropic stress. The contribution of free volume from the deviatoric stress, possibly on the same order as that due to isotropic stress, is not considered. To take into account the volumetric deformation due to the deviatoric deformation, we introduce the concept of *effective free volume*. The effective free volume consists of the volumetric deformation generated from both the isotropic stress induced dilation, shear induced dilation and the dilatation from any other sources including the contributions from moisture content and temperature variation. The shear induced local dilatation, which was ignored in the previous free volume considerations (Knauss and Emri, 1981 and 1987; Losi and Knauss, 1992), is included here in the effective fractional free volume to account for the shear induced acceleration to deformation rate. Following the same consideration as that of the fractional free volume, we now assume that the fractional effective free volume is a fraction of the total volumetric deformation and is given by

$$f \equiv f_e + \alpha(\epsilon_{kk} + \frac{2\beta' \cos(\theta_0 + \gamma_{oct}) \sin \gamma_{oct}}{\sin \theta_0}), \tag{3.21}$$

where α is a material parameter. We consider here small deformations with shear strains on the order of a few percent, therefore $\sin \gamma_{oct} \cong \gamma_{oct}$. Introducing a material parameter β as defined by

$$\beta \equiv 2\alpha\beta',$$

Eq. (3.21) then becomes

$$f = f_e + \alpha\epsilon_{kk} + \beta\frac{\cos(\theta_0 + \gamma_{oct})\gamma}{\sin\theta_0}. \tag{3.22}$$

With the extension of the free volume concept to effective fractional free volume, the time shift factor may be still described by Eq. (3.8), but the fractional free volume f has to be understood as the fractional effective free volume as given by Eq. (3.9)

Model Parameters

The nonlinearly viscoelastic behavior of amorphous polymers in isothermal state at any temperatures below or above the glass transition may be described by equations Eq. (3.13) and (3.14) with the internal material governing time ξ determined by Eq. (3.7) and the shift factor a_T determined by Eq. (3.8). The effective fractional free volume f is given by Eq. (3.22) with α and β being material parameters having different values in the glassy regime and rubbery regime.

It is found that with a pair of parameters ($\alpha = 1.0, \beta = 1.0$) all the behavior observed may be explained qualitatively, however, to best fit the data under various loading conditions, the following parameters may be appropriate.

$$\begin{aligned}
f_0 &= 0.036 \\
B &= 0.4342 \\
\alpha_g &= 2.5 \times 10^{-4}\ C^{-1} \\
\alpha_l &= 9.47 \times 10^{-4}\ C^{-1}. \\
\text{Below } T_g, \quad \alpha &= 0.3 \\
\beta &= 0.6. \\
\text{Above } T_g, \quad \alpha &= 1.0 \\
\beta &= 0.25.
\end{aligned}$$

The analysis requires the bulk relaxation modulus $K(t)$ and shear relaxation modulus $\mu(t)$ for infinitesimal deformation. While $\mu(t)$ has been determined for PMMA (Lu and Knauss, 1996), the bulk modulus is not available in the literature. Correspondingly, the shear creep behavior cannot be determined from the applied axial and shear stresses. However, we may obtain the effective fractional free volume from the measured surface deformations, and compute the time-temperature shift factor from the effective free volume. The model predicted shear creep compliance may then be determined and compared with the experimental results.

Appendix

Axial-torsional Alignment of the Cylindrical Specimens

The alignment of the specimen relative to the MTS frame is essential. A misaligned loading frame may apply unexpected bending moment on the specimen and generate inhomogeneous stress and strain field on a specimen. When a specimen is gripped improperly on an MTS test system the specimen may be subjected to unexpected complicated loading conditions: the upper and lower ends of the specimen may not be parallel to each other, resulting in a bending moment on the specimen. Also suppose that the axis of the upper grip is not aligned with the axis of the lower grip; This may induce both a bending moment and shear forces on the test section. Because this experimental research focuses on relatively small deformations, deformations resulting from the misalignment that are comparable to those arising from infinitesimal loading need to be suppressed.

An alignment fixture[13] (figure 3.36 and 3.37) is designed to conduct the axial-torsional alignment of the grip on the MTS material test system. It employs a low temperature alloy, Woods metal (Belmont Metals Inc.), with a melting point between $70°C$ and $75°C$. To effect the alignment one fixes a pot with grooves in the vertical and circumferential directions to the base of the MTS frame. The load cell is connected to the lower grip, and an extension part (plug) which also has grooves in the axial and circumferential directions is connected to the load cell (figure 3.36). A dummy aluminum cylindrical specimen that has the same dimensions as the actual specimen is at first gripped on the top piston of the MTS frame. The Woods metal pot is first heated up by an Ohm heater wrapped on the pot to a temperature of $100°C$. The melting Woods metal is poured into the Woods metal pot to fill out the space between

[13]Thank Ted Nicolas of Wright Pat for making idea and drawings available.

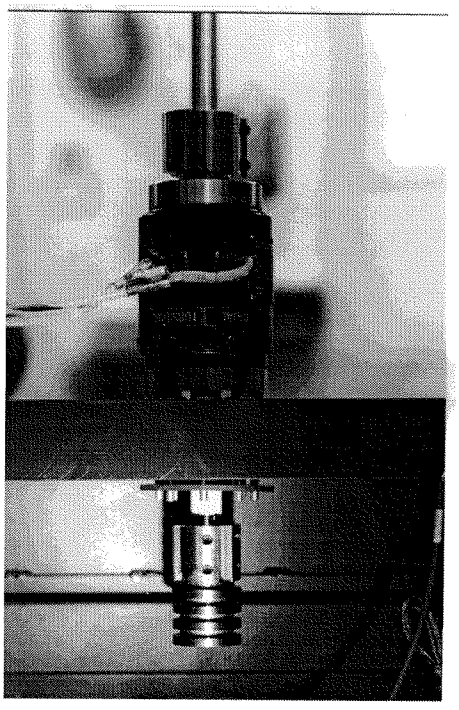

Figure 3.36: Axial-torsional alignment of the MTS loading frame

the pot and the extension part (plug). The alignment at this moment is perfect. We then stop heating up the pot and cool down the Woods metal slowly in the air. After the Woods metal has solidified, the Woods metal pot and the plug become one piece. The load applied to the specimen is taken over by the base of the MTS frame through the Woods metal and the pot.

To demonstrate the effect of misalignment, Figure 3.38 shows the (optical) projection of the relative surface displacements of a cylindrical specimen subjected to simultaneous tension and torsion[14]. As seen in this figure, besides tensile and torsional loading, there are some other unexpected deformations that arise from misalignment. For comparison, Figure 3.39 shows a projection of the relative surface displacements of a specimen subjected to simultaneous tension and torsion. The maximum displacement vector has a magnitude of 0.32 pixels, the axial strain is 0.25% and the shear

[14]In this displacement field the average displacement vector has been subtracted to make a better visual results.

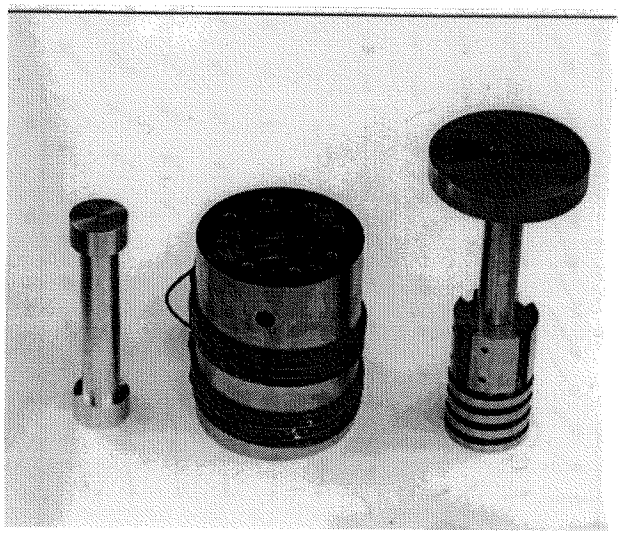

Figure 3.37: Components of the alignment fixture

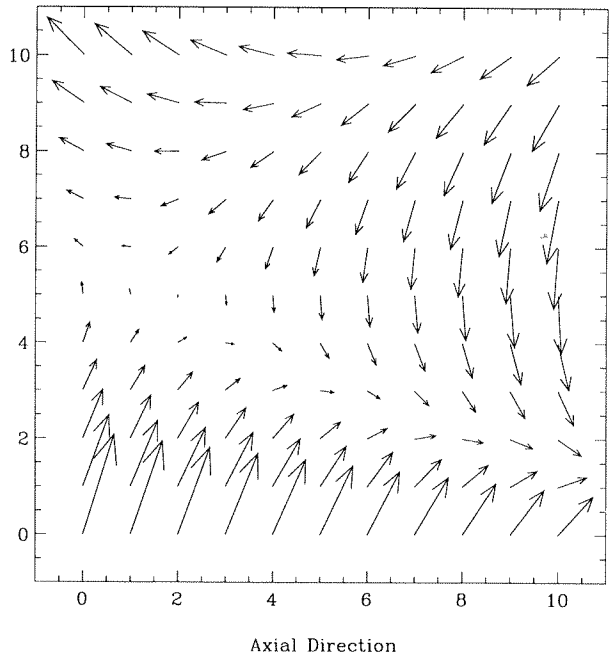

Figure 3.38: A projection of a relative displacement field for a mis-aligned specimen

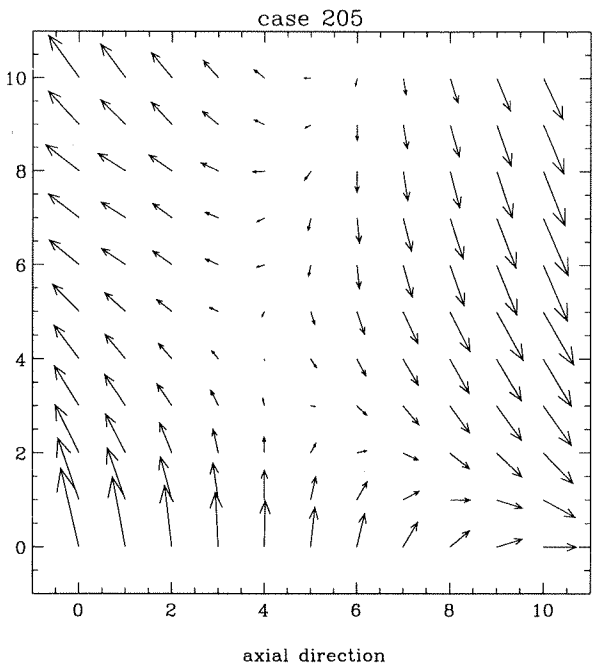

Figure 3.39: A projection of a relative displacement field for a well-aligned specimen

strain is 0.19%. It can be seen that a simultaneous tension and torsion are applied on the specimen and the displacements due to misalignment are very small.

References

Argon, A.S., (1973), "A theory for the Low-temperature Plastic Deformation of Glassy Polymers", *Philosophical Magazine*, **28**, 839-865

Bruck, H.A., McNeil, S.R., Sutton, M.A. and Peters, W.H., (1989), "Digital Image Correlation using Newton-Raphson Method of Partial Differential Correction", *Experimental Mechanics*, **29**(3), 261-267

Carapellucci, L.M. and Yee, A.F., (1986), "The Biaxial Deformation and Yield Behavior of Bisphenol-A Polycarbonate: Effect of Anisotropy", *Polymer Engineering and Science*, Vol. 26, No. 13, pp. 920-930

Cohen, M.H. and Turnbull, D., (1959), "Molecular Transport in Liquids and Glasses", *Journal of Chemical Physics*, Vol. 17, pp. 1-46

Cohen, M.H., Turnbull, D., (1959), "Molecular Transport in Liquids and Glasses", *Journal of Chemical Physics*, Vol. 31, pp.1164-1169

Chu, T.C., Rason, W.F., Sutton, M.A. and Peters, W.H., (1985), "Applications of Digital-Image-Correlation Techniques to Experimental Mechanics", *Experimental Mechanics*, **25**(3), 232-244

Deng, T.H. and Knauss, W.G., (1996), "Dynamic Volume Compliance of a Polymer", GALCIT SM Report 96-5, California Institute of Technology. To appear in *Mechanics of Time Dependent Materials*, **1** 1997

Doi, M., (1986), *Theory of Polymer Dynamics*, Oxford University Press

Doolittle, A.K., (1951), "Studies in Newtonian Flow. I. The Dependence of the

Viscosity of Liquids on Temperature", *Journal of Applied Physics*, Vol. 22, pp. 1031-1035

Doolittle, A.K., (1951), "Studies in Newtonian Flow. II. The Dependence of the Viscosity of Liquids on Free-Space", *Journal of Applied Physics*, Vol. 22, pp. 1471-1475

Ewing, P.D., Turner, S. and Williams, J.G., (1972), "Combined Tension-Torsion Studies on Polymers: Apparatus and Preliminary Results for Polythene", *Journal of Strain Analysis*, Vol. 7, pp. 9-22

Ewing, P.D., Turner, S. and Williams, J.G., (1973), "Combined Tension-Torsion Creep of Polythene with Abrupt Changes of Stress", *Journal of Strain Analysis*, Vol. 8, pp. 83-89

Ferry, J.D. and Stratton, R.A., (1960), "The Free Volume Interpretation of the Dependence of Viscosities and Viscoelastic Relaxation Times on Concentration, Pressure and Tensile Strain", *Kolloid-Zeitschrift*, Vol. 171, pp. 107-111

Fillers, R.W. and Tschoegl, N.W., (1977), "The Effect of Pressure on the Mechanical Properties of Polymers", *Transactions of the Society of Society of Rheology*, Vol. 21, pp.51

Gilmour, I. Trainor, A. and Howard, (1974), *Journal of Polymer Science, Polymer Physics Edition*, **12**, 1939

Govaert, L., (1995), "Nonlinear Viscoelastic Modeling of Glassy Polymers", *Symposium of the Workshop on Nonlinear, Time-Dependent Constitution of Engineering Polymers*, Institute of Mechanics and Materials, UCSD, La Jolla

Green, A.E. and Rivlin, R.S., (1957), "The Mechanics of Non-Linear Materials with Memory, Part I", *Archive for Rational Mechanics and Analysis*, Vol. 1, pp 1-21

Green, A.E. and Rivlin, R.S., (1960), "The Mechanics of Non-Linear Materials with Memory, Part III", *Archive for Rational Mechanics and Analysis*, Vol. 4, pp. 387-404

Heydemann, P., (1959), "The Dynamic Compressibility of Highpolymers in the Frequency Range from 0.1 c/s to 60 kc/s", *Acustica*, **9**, 446-452

Heymans, L., (1983), "An Engineering Analysis of Polymer Film Adhesion to Rigid Substrates", Ph.D. thesis, California Institute of Technology

Hopkins, I.L. and Hamming, R.W. , (1957), "On Creep and Relaxation", *Journal of Applied Physics*, **28**, 906

James, M.R., Morris, W.L. and Cox, B.N., (1990), "A High Accuracy Automated Strain-Field Mapper", *Experimental Mechanics*, **30**(1), 60-67

Knauss, W.G., (1974), "On the Steady Propagation of a Crack in a Viscoelastic Sheet: Experiments and Analysis", *Deformation & Fracture of High Polymers*, Kausch, Hassell and Jaffe (Eds.), Plenum Press

Knauss, W.G. and Emri, I., (1981), "Non-linear Viscoelasticity Based on Free Volume Consideration", *Computer & Structures*, Vol. 13, pp. 123-128

Knauss, W.G. and Emri, I., (1987), Volume Change and the Nonlinearly Thermo-Viscoelastic Constitution of Polymers, *Polymer Engineering and Science*, Vol. 27, No.1, pp. 86-100

Knauss, W.G. and Kenner, V.H., (1980), "On the Hygrothermomechanical Characterization of Polyvinyl Acetate", *Journal of Applied Physics*, Vol. 51, pp. 5131-5136

Lai, J. and Bakker, A., (1995), "An Integral Constitutive Equation for Nonlinear Plasto-Viscoelastic Behavior of High-Density Polyethylene", *Polymer Engineering*

and Science, 1995, Vol. 35, pp. 1339-1347

Lee, A. and McKenna, G.B., (1989), "The Physical Aging Response of an Epoxy Glass Subjected to Large Stresses", *Polymer*, Vol. 31, pp. 423-430

Lide, D.R., (1995), *Handbook of Chemistry and Physics*, pp. 15-25

Losi, G.U., (1990), "Nonlinear Thermoviscoelastic Behavior of Polymers", Ph.D. thesis, California Institute of Technology

Losi, G.U. and Knauss, W.G., (1992), "Free Volume Theory and Nonlinear Thermoviscoelasticity", *Polymer Science and Engineering*, Vol. 32, No. 8, pp. 542-557

Lou, Y.C. and Schapery, R.A., (1971), "Viscoelastic Characterization of a Nonlinear Fiber-Reinforced Plastic", *Journal of Composites Materials*, Vol. 5, pp. 208-234

Lu, H.B. and Knauss, W.G., (1996), "Nonlinear Thermo-Mechanical Behavior under Multiaxial Loading", Caltech GALCIT SM Report, 96-17

Lu, H.B., Vendroux, G. and Knauss, W.G., (1996), Surface Deformation Measurements via Digital Image Correlation, GALCIT SM Report 96-1, California Institute of Technology, Pasadena, California

Luo, P.F., Chao, Y.J., Sutton, M.A. and Peters, W.H., (1993); "Accurate Measurement of 3-Dimensional Deformations in Deformable and Rigid Bodies Using Computer Vision", *Experimental Mechanics*, **33**(2),123-132

Knauss, W.G. and Kenner, V.H., (1980), *Journal of Applied Physics*, **51**, 10

Lide, D.R., (1995), *Handbook of Chemistry and Physics*, Chemical Rubber Pub. Co., 15-25

Lin, T.S. and Nolle, A.W., (1989), "Dynamic Compressibility of Poly(vinyl ac-

etate) and Poly(methyl Methacrylate): Effects of Molecular Weight", *Polymer*, **30**, 648

Lu, H. and Knauss, W.G., (1993), "The Stress Relaxation Behavior of PMMA", GALCIT SM Report 93-17, California Institute of Technology.

Lu, H. and Knauss, W.G., (1996), "Nonlinear Polymer Response under Biaxial Stress States", GALCIT SM Report 96-2, California Institute of Technology. To appear *Mech. of Time Dep. Mat.* (Kluwer, Dordrecht, Holland), **1**, 1997

Lu, H. Vendroux, G. and Knauss, W.G., (1996), "Surface Deformation Measurements of a Cylindrical Specimen by Digital Image Correlation", GALCIT SM Report 96-1. California Institute of Technology

Matsukawa, S., Mcdonough, W. and Hunston, D.L., (1992), *Proceedings of the 15th Annual Meeting of the Adhesion Society, Library of congress number 92-70209*

McCammond, D. and Turner, S., (1973), *Polymer Engineering and Science*, **13**, 187

McKinney, J.E. and Belcher, H.V., (1963),"Mechanical Properties of Toughened Epoxies", *Journal of Research of the National Bureau of Standards, A. Physics and Chemistry*, **67A(1)**, 43 (1963)

McKinney, J.E., and Simha, R., (1974), "Configurational Thermodynamic Properties of Polymer Liquids and Glasses. Poly(vinyl acetate). I.", *Macromolecules*, Vol. 7, pp.894-901

McKinney, J.E., and Simha, R., (1976), "Configurational Thermodynamic Properties of Polymer Liquids and Glasses. Poly(vinyl acetate). II.", *Macromolecules*, Vol. 9, pp. 430-441

McLoughlin, J.R. and Tobolsky, A.V., (1952), " The Viscoelastic Behavior of Polymethyl Methacrylate", *Journal of Colloid Science*, **7**, 555

Moonan, W.K. and Tschoegl, N.W., (1983), "Effect of Pressure on the Mechanical Properties of Polymers. 2. Expansivity and Compressibility Measurements", *Macromolecules*, Vol. 16, pp. 55

Moonan, W.K. and Tschoegl, N.W., (1984), "Effect of Pressure on the Mechanical Properties of Polymers. 3. Substitution of the Glassy Parameters for Those of the Occupied Volume", *International Journal of Polymer Materials*, Vol. 10, pp. 199

Moonan, W.K. and Tschoegl, N.W., (1985), "Effect of Pressure on the Mechanical Properties of Polymers. 4. Measurements in Torsion", *Journal of Polymer Science, Part B, Polymer Physics*, Vol. 23, pp. 623

Müller, H.K. and Knauss, W.G., (1971), Crack Propagation in a Linearly Viscoelastic Strip, *Journal of Applied Mechanics*, Vol. 38, Series E, pp. 483

Murnahan, F.D., (1951), *Finite Deformation of Elastic Solid*, Wiley, New York, pp.130-137

Poynting, J.H., (1912), "On the Change in the Dimensions of a Steel Wire when Twisted, and on the Pressure of Distorsional Waves in Steel", *Proceedings of Royal Society of London Series A*, Vol. 86, pp. 534-561

Rusch, K.C., (1968), "Time-Temperature Superposition and Relaxation Behavior in Polymeric Glasses", *Journal of Macromolecule Science – Physics*, Vol. B2(2), pp. 179-204

Schapery, R.A., (1966), "A Theory of Nonlinear Thermoviscoelasticity Based on Irreversible Thermodynamics", *Proceedings of the 5th U.S. National Congress of Applied Mechanics*, ASME, 511

Schapery, R.A., (1969), "Further Development of a Thermodynamic Constitutive Theory: Stress Formulation", Purdue University, Report No. 69-2

Sharpe, W.N., (1982), "Applications of the Interferometric Strain/Displacement Gage", *Optical Engineering*, **21**(3), 483-488

Shay, R.M., Jr. and Caruthers, J.M., (1986),"A New Nonlinear Viscoelastic Constitutive Equation for Predicting Yield in Amorphous Solid Polymers", *Journal of Rheology*, Vol. 30, No. 4, pp. 781-827

Simha, R., Curro, J.G. and Robertson, R.E., (1984), "Molecular Dynamics of Physical Aging in the Glassy State", *Polymer Engineering and Science*, Vol., 24, No. 14, pp. 1071-1078

Sternstein, S.S. and Ongchin, L., (1969), "Yield Criteria for Plastic Deformation of Glassy High Polymers in General Stress Fields", *American Chemical Society: Polymer Preprints*, Vol. 10, pp. 1117-1124

Struik, L.C.E., (1978), *Physical Aging in Amorphous Polymers and Other Materials*, Elsevier Scientific Publishing Company

Sutton, M.A., Cheng, M., Peters, W.H., Chao, Y.J. and McNeil, S.R., (1986), "Application of an Optimized Digital Image Correlation Method to Planar Deformation Analysis", *Image Vision Computing*, **4**(3), 143-150

Sutton, M.A., McNeil, S.R., Jang, J. and Babai, M., (1988), "The Effect of Subpixel Image Restoration on Digital Image Correlation Estimates", *Optical Engineering*, **27**(10), 870-877

Sutton, M.A., Walters, W.J., Peters, W.H., Rason, W.F. and McNeil, S.R. (1983), "Determination of Displacements using an Improved Digital Correlation Method", *Image Vision Computing*, **1**(3) 133-139

Tervoort, T.A., (1996), *Ph.D. thesis, Constitutive Modeling of Glassy Polymers: Finite Non-Linear Viscoelastic Behavior of Polycarbonate*

Thorkildsen, R.L., (1964), *Engineering Design for Plastics*, E. Baer, ed., Reinhold, NY

Timoshenko, S., (1940), *Strength of Materials*, D. Van Nostrand Company, Inc., pp.299

Veazie, D.R. and Gates, T.S., (1997), Compressive Creep of IM7/K3B Composite and the Effects of Physical Aging on Viscoelastic Behavior, *Experimental Mechanics*, Vol. 37, No. 1, pp. 62

Vendroux, G. and Knauss, W.G.,, (1994a), "Deformation Measurements at the Sub-Micron Size Scale: I. Design of a Digital Scanning Tunneling Microscope", GALCIT report SM 94-4, Caltech , Submitted to *Experimental Mechanics*

Vendroux, G. and Knauss, W.G., (1994b), "Deformation Measurements at the Sub-Micron Size Scale: II. Refinements in the Algorithm for Digital Image Correlation", GALCIT Report 94-5, Caltech, submitted to *Experimental Mechanics*

Williams, M.L., Landel, R.F. and Ferry, J.D., (1955), *Journal of the American Chemical Society*, **77**, 3701

Wilson, I., Ladizesky, N.M. and Ward, I.M., (1976), *Journal of Materials Science*, **11**, 2177

Wilson, I., Cunningham, A. and Ward, I.M., (1976), *Journal of Materials Science*, **11**, 2181

Wineman, A. S. and Waldron, W.K., Jr., (1995), "Yieldlike Response of a Compressible Nonlinear Viscoelastic Solid", *Journal of Rheology*, Vol. 39, pp.401-423

Zhang, X. and Knauss, W.G., (1991), "Poisson and Bulk Relaxation Properties of Polymethyl methacrylate", GALCIT SM Report 91-9, California Institute of Technology